5-2012

MODELING ONE- AND TWO-DIMENSIONAL SHALLOW WATER FLOWS WITH DISCONTINUOUS GALERKIN METHOD

Wencong Lai
Clemson University, wlai@g.clemson.edu

MODELING ONE- AND TWO-DIMENSIONAL SHALLOW WATER FLOWS WITH DISCONTINUOUS GALERKIN METHOD

A Dissertation
Presented to
the Graduate School of
Clemson University

In Partial Fulfillment
of the Requirements for the Degree
Doctor of Philosophy
Civil Engineering

---

by
Wencong Lai
May 2012

Accepted by:
Abdul A. Khan, Committee Chair
Taufiqaur R. Khan
Earl J. Hayter
Nadarajah Ravichandran

ABSTRACT

Numerical models for one- and two-dimensional shallow water flows are developed using discontinuous Galerkin method. Formulation and characteristics of shallow water equations are discussed. The well-balanced property and wetting/drying treatment are provided in the numerical models. The shock-capturing property is achieved by the approximate Riemann solvers in the schemes. Effects of different approximate Riemann solvers are also investigated. The Total Variation Diminishing property is achieved by adoption of slope limiters. Different slope limiters and their effects are compared through numerical tests. Numerical tests are performed to validate the models. These tests include dam-break flows, hydraulic jump and shocks in channels, and flows in natural rivers. Results show that the numerical models developed in present work are robust, accurate, and efficient for modeling shallow water flows.

The one-dimensional model shows that the area based slope limiter provided the best solution in natural channels. The slope limiter based on the water depth or water surface elevation performs progressively poorer as the cross-section shape deviates from rectangular. In the approximate Riemann solver, the wave speeds are based on the original form of the equations, although the pressure force and the gravity force terms are combined for solving the shallow water equations with discontinuous Galerkin method. The combined term is discretized, in one- and two-dimensional models, such that the stationarity property is preserved. Different wetting and drying procedures are evaluated

for the one- and two-dimensional models. Analytical, laboratory, and field tests are conducted to verify the accuracy of the wetting and drying procedures.

TABLE OF CONTENTS

Table of Contents (Continued)

Page

LIST OF TABLES

LIST OF FIGURES

List of Figures (Continued)

List of Figures (Continued)

Figure Page

List of Figures (Continued)

Figure Page

List of Figures (Continued)

Figure Page

List of Figures (Continued)

Figure Page

List of Figures (Continued)

Figure Page

List of Figures (Continued)

Figure Page

CHAPTER ONE

INTRODUCTION

Numerical modeling of open channel flows has been of great interest to hydraulics researchers and engineers. The governing equations for shallow water flows are the well-known Saint-Venant equations. For most practical cases of river flow problems, the shallow water hypothesis is valid. Over recent decades, many numerical schemes have been developed to solve the Saint-Venant equations (Fennema and Chaudhry, 1990; Capart et al., 2003). The difficulties in modeling these equations come from the treatment of the convective flux and source terms (Garcia-Navarro and Vázquez-Cendón, 2000).

Improper treatment of source term results in non-physical flows in the simulation domain. Nujić (1995) proposed a non-oscillatory scheme in rectangular channels, where the pressure force term was extracted from the flux term and discretized to achieve compatibility with the bed slope term. Garcia-Navarro and Vázquez-Cendón (2000) discussed the difficulties associated with the correct treatment of the geometrical source term, and proposed an upwind treatment for this term. Perthame and Simeoni (2001) presented a kinetic approach for the treatment of the source term in rectangular channels. Zhou et al. (2001) proposed the water surface gradient method for the treatment of the source term in the data reconstruction step. Sanders et al. (2003) provided an exact expression for the source term in a trapezoidal channel, which included forces due to channel width changes and bed elevation. Ying et al. (2004) developed a weighted

average water surface gradient approach based on the Courant number criterion to deal with the source term. Catella et al. (2008) proposed a predictor-corrector method based on the Froude number, where the bed elevation change term and the wall pressure force term were discretized to guarantee the elimination of nonphysical flows due to changes in the bed topography with a constant water surface elevation. Modified shallow water equations (Ying et al., 2009; Kesserwani and Liang, 2010) or flux modification (Ern et al, 2008; Xing et al. 2010) can also be used to deal with source term.

Since the shallow water equations are hyperbolic, a discontinuous solution may be generated even if the initial conditions and boundary conditions are smooth. In recent decades, the Discontinuous Galerkin (DG) method has gained popularity in modeling shallow water flows as it combines the advantages of the finite element method and the finite volume method (Schwanenberg and Harms, 2004; Kesserwani et al., 2008). The DG method was first introduced by Reed and Hill (1973) for the solution of neutron transport equation. Later, Cockburn and Shu (1988, 1989, and 1998) and Cockburn et al. (1989, 1990) introduced the Runge-Kutta Discontinuous Galerkin (RKDG) method to solve the nonlinear, time-dependent, hyperbolic conservation laws. In the DG method, higher order interpolation functions can be utilized to attain higher order spatial accuracy. Since the DG method allows solutions to be discontinuous across element boundaries, it provides better solution strategy for problems including shocks and discontinuities. According to Li (2006), the RKDG method provides additional advantages, for example, the RKDG method can easily deal with a source term as can the finite element method. By decoupling the elements using boundary flux, a local formulation is achieved that

does not require assembling the global matrix and explicit time schemes can be implemented. The local formulation is also efficient in cases of nonlinear problems that require iterative solutions (Dolejší, 2010). In practical applications, where millions of elements may be used, the RKDG method will prove advantageous in terms of computing speed and memory demand. The RKDG method is a conservative scheme, which is a suitable choice for physical problems, since most physical properties such as mass and momentum are conservative quantities. In addition, the hp-adaptive algorithm is much easier to apply to the RKDG local formulation.

Schwanenberg and Köngeter (2000) were the first to implement the RKDG method for shallow water equations for applications to practical problems like shocks, dam-break problem, and oblique hydraulic jump. Later, Schwanenberg and Harms (2004) investigated the accuracy and convergence of the RKDG method in transcritical flows. Aizinger and Dawson (2002) and Dawson and Aizinger (2005) applied the RKDG method to two-dimensional and three-dimensional shallow water flows. Kubatko et al. (2006) demonstrated the applicability of the hp-adaptive algorithm for the RKDG method. In recent years, significant progress has been achieved in the application of the DG method to dam-break flows in channels (Fagherazzi et al., 2004; Schwanenberg and Harms, 2004), coastal wave disturbance and tidal flows (Eskilsson and Sherwin, 2004; Aizinger and Dawson, 2002), and flooding and drying (Bokhove, 2005; Ern et al, 2008; Xing et al., 2010).

In solving hyperbolic conservation laws, exact and various approximate Riemann solvers are employed to achieve accurate approximations for the flux terms. Godunov

(1959) was the first to introduce a discontinuous solution for the flux terms by using the exact formulation of a Riemann problem. Roe (1981) introduced a solution to the linearized Riemann problems for conservation laws and it is known as the Roe flux. Harten et al. (1983) introduced the HLL (Harten-Lax-van Leer) flux where upstream differencing and Godunov-type schemes were utilized for hyperbolic conservation laws. Einfeldt (1988) proposed the positively conservative HLLE (Harten-Lax-van Leer-Einfeldt) flux for conservation laws. Toro (1989) suggested a weighted average flux method for hyperbolic conservation laws based on the wave speeds of the system. Toro et al. (1994) presented the HLLC (Harten-Lax-van Leer Contact wave) flux, a modification of the HLL flux, to take into account the contact and shear waves for equations with three distinct eigenvalues or characteristic wave speeds.

Like most higher-order methods, oscillations are observed in numerical solutions near discontinuities, and additional efforts are needed to eliminate these oscillations. The Essentially Non-oscillatory (ENO) scheme (Harten et al., 1987) and the Total Variation Diminishing (TVD) scheme are the two widely used methods to reduce oscillations. The key idea in the ENO scheme is to choose the locally smoothest stencil with a nonlinear adaptive procedure at the approximation level. Later, Liu et al. (1994) constructed the Weighted Essentially Non-oscillatory (WENO) scheme in a similar way. The ENO and WENO schemes were originally constructed within the framework of the finite volume method and the finite difference method. Qiu and Shu (2005) applied the WENO limiters with the discontinuous Galerkin finite element method. Schemes that satisfy the Total Variation Diminishing (TVD) criterion are oscillation-free schemes as well. Flux limiters

and slope limiters are widely used to achieve the TVD property. The key idea for flux limiter and slope limiter is the same. The flux limiter would be applied directly to the fluxes while slope limiter would be applied to the conservative variables or primitive variables. For this reason, slope limiters are preferred, since it may better preserve the conservative property and reduce oscillations.

The goal of this research is to develop robust, accurate, and efficient numerical models for shallow water flows in one and two dimensions. A suitable choice of governing equations and the treatment of the source term that provides a well-balanced scheme will be illustrated. This research will advance the application of the discontinuous Galerkin method to natural rivers with wetting/drying episodes modeled with complex geometries. Various schemes to approximate numerical fluxes will be investigated. Different slope limiters will be tested and their effects will be compared. A number of numerical tests will be performed to validate these models. Numerical scheme development for the one-dimensional shallow water flows is presented in Chapter 2, followed by numerical tests in Chapter 3. The numerical scheme for two-dimensional shallow water flows is given in Chapter 4, with numerical tests presented in Chapter 5. Summary and conclusions are provided in Chapter 6.

CHAPTER TWO

NUMERICAL SCHEME FOR ONE-DIMENSIONAL FLOWS

This chapter provides the details of the numerical scheme using discontinuous Galerkin finite element method to model the one-dimensional shallow water flow equations. Implementation of the approximate Riemann solver for numerical fluxes and slope limiters used to achieve TVD property are discussed. The time integration of the governing equations using TVD Runge-Kutta scheme is illustrated.

2.1 Shallow water flow equations

The governing equations of one-dimensional shallow water flows for natural rivers with irregular cross-section are known as the Saint-Venant equations. The continuity and momentum equations are based on several assumptions, including mild slope, uniform velocity over cross-section, vertical accelerations are negligible, and so on. The one-dimensional governing equations are given by

$$\frac{\partial A}{\partial t} + \frac{\partial Q}{\partial x} = 0 \tag{2.1}$$

$$\frac{\partial Q}{\partial t} + \frac{\partial (Q^2 / A + gI_1)}{\partial x} = gI_2 + gA(S_o - S_f) \tag{2.2}$$

where the hydrostatic pressure force I_1, wall pressure force I_2, bed slope S_o, and friction slope S_f are defined, respectively, as

$$I_1 = \int_0^{h(x,t)} (h-y)b(x,y)dy\,; \quad I_2 = \int_0^{h(x,t)} (h-y)\frac{\partial b(x,y)}{\partial x}dy \tag{2.3}$$

$$S_o = -\frac{\partial z_b}{\partial x}; \quad S_f = \frac{n^2 Q|Q|}{R^{4/3}A^2} \tag{2.4}$$

In the equations described above, $Q =$ flow rate, $A =$ cross-section area, $n =$ Manning's roughness coefficient, $b =$ channel width at the water surface, $z_b =$ channel bed elevation, $h =$ water depth, $g =$ gravitational acceleration, and $R =$ hydraulic radius. A sketch of a natural channel cross-section geometry is shown in Figure 2.1. The eigenvalues and eigenvectors for the Saint-Venant equations are given, respectively, by Equations (2.5) and (2.6).

$$\begin{cases} \lambda_1 = Q/A - \sqrt{gA/b} = u - c \\ \lambda_2 = Q/A + \sqrt{gA/b} = u + c \end{cases} \tag{2.5}$$

$$\begin{cases} \mathbf{k}_1 = [1\,, u-c]^T \\ \mathbf{k}_2 = [1\,, u+c]^T \end{cases} \tag{2.6}$$

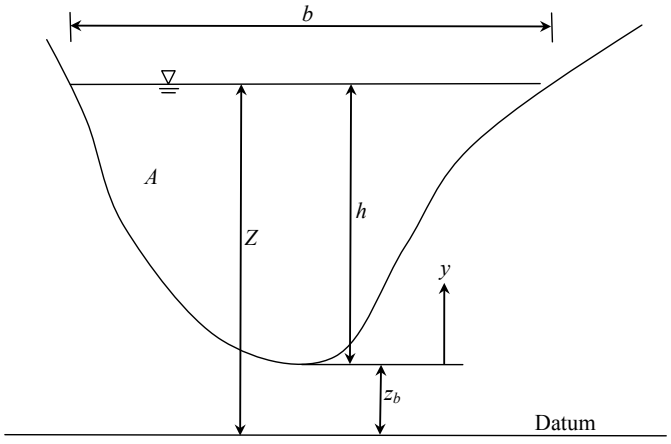

Figure 2.1 Natural channel cross-section

Due to the known difficulty in calculating and generalizing the hydrostatic and wall pressure force terms, Equation (2.2) can be simplified following Leibnitz's rule as follows (Cunge et al., 1980)

$$\frac{\partial Q}{\partial t}+\frac{\partial(Q^2/A)}{\partial x}=-gA\frac{\partial Z}{\partial x}-gAS_f \tag{2.7}$$

where Z is the water surface level, as shown in Figure 2.1, that combines the pressure force and bed elevation change terms. An advantage of this equation is that it circumvents unphysical bed slope generated flow due to inadequate treatment of the bed slope term. That is, if the water in the channel is at rest initially it will remain at rest. As part of the flux term in the original momentum equation, Equation (2.2), is combined with the source term, special attention has to be paid to calculate the numerical flux at the cell interface accurately. The accuracy of the numerical flux is controlled by the convective flux term (Nujić, 1995). The incomplete flux function in Equation (2.7) will give an accurate solution if the pressure force term is treated properly. The details of the pressure force term treatment will be given latter. In addition, the above equation is easier to solve numerically than Equation (2.2) as integral terms for pressure force calculations are eliminated.

As described before, the flux terms in the Saint-Venant equations are generally discretized using approximate Riemann solvers (e.g., Roe flux, HLL, HLLE, or HLLC). These approximate Riemann solvers achieve upwinding along the characteristic directions that are given by the eigenvalues. Eigenvalues represent characteristics speeds or physical speeds with which disturbances move in the channel. Since the physical

characteristics of the equations are independent of the mathematical form of the equations, the actual eigenvalues and eigenvectors based on Equations (2.1) and (2.2) are used for the approximate Riemann solver (i.e., HLL and Roe flux) in this study to solve Equations (2.1) and (2.7).

2.2 Discontinuous Galerkin method formulation and source term treatment

The one-dimensional domain of length L is divided into m elements with m+1 nodes ($0 = x_1 < x_2 \cdots < x_{m+1} = L$). A typical spatial discretization in the discontinuous Galerkin method is illustrated in Figure 2.2 with linear non-overlapping elements. The channel geometry and roughness coefficient are specified at the nodes. For linear elements, this means that these properties are specified at the end of an element.

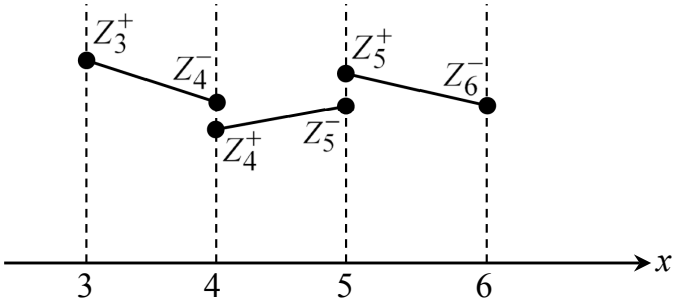

Figure 2.2 Spatial discretization for discontinuous elements

The discontinuous Galerkin formulation is written for each element in local coordinate system $\xi \in [-1,1]$ corresponding to an element with global coordinate system $x \in [x_s, x_e]$, where x_s and x_e are the start and end coordinates, respectively. Linear

interpolating functions (also known as basis or shape functions) are used to describe the variation of the nodal values within an element. In an element, the variation of A, Q, and any function f (like friction slope) can be written as (note Einstein summation notation is assumed)

$$\hat{A} = N_j A_j; \quad \hat{Q} = N_j Q_j; \quad \hat{f}\left(A,Q\right) = f\left(\hat{A},\hat{Q}\right); \quad j = 1,2 \tag{2.8}$$

where $N_1 = 0.5(1-\xi)$ and $N_2 = 0.5(1+\xi)$ are the basis functions, and j refers to number of nodes in an element (2 for linear elements). The conversion from global to local coordinates is achieved by recognizing that $dx = 0.5\Delta x d\xi$, where Δx is the size of the element, and any spatial derivative in the global coordinate (x) can be transformed into the local coordinate (ξ).

The discontinuous Galerkin finite element method is applied to Equations (2.1) and (2.7). First the equations are multiplied by weight or test functions, N_i ($i = 1,2$ for linear elements), and are assumed to be the same as shape functions N_j in the Galerkin method. Next, integration over an element is carried out. The resulting equations, after integration by parts of the flux terms, can be written as

$$\left[\int_{x_s}^{x_e} N_i N_j dx\right]\frac{\partial A_j}{\partial t} = \int_{x_s}^{x_e} \frac{\partial N_i}{\partial x}\hat{Q}dx - N_i(x_e)P_2 + N_i(x_s)P_1 \tag{2.9}$$

$$\begin{aligned}\left[\int_{x_s}^{x_e} N_i N_j dx\right]\frac{\partial Q_j}{\partial t} &= \int_{x_s}^{x_e} \frac{\partial N_i}{\partial x}\frac{\hat{Q}^2}{\hat{A}}dx - N_i(x_e)G_2 + \\ N_i(x_s)G_1 &+ \int_{x_s}^{x_e} N_i\left(-g\hat{A}\frac{\partial \hat{Z}}{\partial x} - \frac{gn^2\hat{Q}\left|\hat{Q}\right|}{\hat{R}^{4/3}\hat{A}}\right)dx\end{aligned} \tag{2.10}$$

where $P(x,t)=Q$ and $G(x,t)=Q^2/A$ are the numerical fluxes at the element boundary and are computed using Riemann solvers. The final step is to transform Equations (2.9) and (2.10) into the local coordinate system. The transformed equations can then be integrated easily using Gauss-Legendre quadrature rules.

The water surface gradient term on the right hand side of Equation (2.10) is discretized using the following expression (see Figure 2.2)

$$\begin{cases} -gN_1\hat{A}\dfrac{\partial\hat{Z}}{\partial x} = -gN_1\dfrac{(A_{x_s}^- + A_{x_e}^-)}{2}\dfrac{(Z_{x_e}^- - Z_{x_s}^-)}{(x_e - x_s)} = N_1C_1 \\ -gN_2\hat{A}\dfrac{\partial\hat{Z}}{\partial x} = -gN_2\dfrac{(A_{x_s}^+ + A_{x_e}^+)}{2}\dfrac{(Z_{x_e}^+ - Z_{x_s}^+)}{(x_e - x_s)} = N_2C_2 \end{cases} \tag{2.11}$$

where $A_{x_s}^-$ and $A_{x_s}^+$ are the values of A at boundary x_s from the left and right elements, N_1, N_2 $(i=1,2)$ correspond to test functions at nodes 1 and 2 of the element, respectively, and C_1, C_2 are treated as constants during integration.

The discretization scheme for the combined pressure force and bed elevation change terms given by Equation (2.11) will not produce unphysical bed slope generated flows referred to as a numerical imbalance problem (Kesserwani et al, 2010) under still water condition. For a constant water surface elevation with zero flow, Equation (2.11) will maintain the still water steady state (or stationary solution) as the water surface gradient term will vanish, that is, $Z_{x_e}^- = Z_{x_s}^-$, $Z_{x_e}^+ = Z_{x_s}^+$, and the time derivative terms in Equations (2.9) and (2.10) are equal to zero. In addition, the discretization in Equation (2.11) is similar to central difference and models diffusive flux accurately. If pressure force and bed elevation change terms are separated, special care has to be exercised to

achieve a well-balanced scheme (preserving constant water surface and zero discharge in a channel with irregular bed topography, also known as stationarity test).

2.3 Numerical flux functions and dry bed treatment

Some widely used approximate Riemann solvers have been discussed before. In this study, the HLL flux and Roe flux are adopted for the one dimensional two-wave system. The wave speeds are calculated using a method suggested by Fraccarollo and Toro (1995). For the conserved-variable vector $\mathbf{U} = [A, Q]^T$ and flux vector $\mathbf{F} = [Q, Q^2/A]^T = [P, G]^T$, the approximate numerical fluxes at the boundaries of an element are given as

$$\mathbf{F}^{HLL}\left(\mathbf{U}^-, \mathbf{U}^+\right) = \begin{cases} \mathbf{F}^-; & 0 \le S_L \\ \dfrac{S_R\mathbf{F}^- - S_L\mathbf{F}^+ + S_L S_R\left(\mathbf{U}^+ - \mathbf{U}^-\right)}{S_R - S_L}; & S_L < 0 < S_R \\ \mathbf{F}^+; & 0 \ge S_R \end{cases} \tag{2.12}$$

$$\begin{cases} S_L = \min\left(u^- - \sqrt{g\left(A/b\right)^-}, \quad u^* - c^*\right) \\ S_R = \max\left(u^+ + \sqrt{g\left(A/b\right)^+}, \quad u^* + c^*\right) \end{cases} \tag{2.13}$$

$$u^* = \frac{1}{2}(u^- + u^+) + \sqrt{g\left(A/b\right)^-} - \sqrt{g\left(A/b\right)^+} \tag{2.14}$$

$$c^* = \frac{1}{2}(\sqrt{g\left(A/b\right)^-} + \sqrt{g\left(A/b\right)^+} + \frac{1}{4}(u^- - u^+) \tag{2.15}$$

where $\mathbf{F}^- = \mathbf{F}(\mathbf{U}^-)$ and $\mathbf{F}^+ = \mathbf{F}(\mathbf{U}^+)$.

In Roe's (1981) method, the original non-linear conservation law is replaced by a linearized system with constant coefficient, called the Roe Jacobian matrix. That is, the original Riemann problem is replaced by the approximate Riemann problem. Following Garcia-Navarro and Vázquez-Cendón (2000), the approximate numerical flux is given by

$$\mathbf{F}^{Roe} = \frac{1}{2}\left(\mathbf{F}^{-} + \mathbf{F}^{+}\right) - \frac{1}{2}\sum_{i=1}^{2} \tilde{\alpha}_i \left|\tilde{\lambda}_i\right| \tilde{\mathbf{k}}_i \tag{2.16}$$

$$\tilde{\alpha}_1 = \frac{(\tilde{c} + \tilde{u})\Delta A - \Delta Q}{2\tilde{c}}; \quad \tilde{\alpha}_2 = \frac{(\tilde{c} - \tilde{u})\Delta A + \Delta Q}{2\tilde{c}} \tag{2.17}$$

$$\tilde{\lambda}_1 = \tilde{u} - \tilde{c}; \quad \tilde{\lambda}_2 = \tilde{u} + \tilde{c} \tag{2.18}$$

$$\tilde{\mathbf{k}}_1 = (1, \tilde{u} - \tilde{c})^T; \quad \tilde{\mathbf{k}}_2 = (1, \tilde{u} + \tilde{c})^T \tag{2.19}$$

$$\tilde{u} = \frac{Q^+\sqrt{A^-} + Q^-\sqrt{A^+}}{\sqrt{A^-A^+}\left(\sqrt{A^-} + \sqrt{A^+}\right)} \tag{2.20}$$

$$\tilde{c} = \sqrt{\frac{g}{2}\left[\left(A/b\right)^- + \left(A/b\right)^+\right]} \tag{2.21}$$

$$\Delta A = A^+ - A^-; \; \Delta Q = Q^+ - Q^- \tag{2.22}$$

For HLL flux, the wave speeds for a dry bed to the right or left of the element under consideration are, respectively, given by

$$S_L = u_L - \sqrt{g\left(A/b\right)_L}; \quad S_R = u_L + 2\sqrt{g\left(A/b\right)_L} \tag{2.23}$$

$$S_L = u_R - 2\sqrt{g\left(A/b\right)_R}; \quad S_R = u_R + \sqrt{g\left(A/b\right)_R} \tag{2.24}$$

For the Roe flux function, the corresponding wave speeds are given by

$$\tilde{\lambda}_1 = u_L - \sqrt{g\left(A/b\right)_L}; \quad \tilde{\lambda}_2 = u_L + 2\sqrt{g\left(A/b\right)_L} \tag{2.25}$$

$$\tilde{\lambda}_1 = u_R - 2\sqrt{g\left(A/b\right)_R}\,; \quad \tilde{\lambda}_2 = u_R + \sqrt{g\left(A/b\right)_R} \tag{2.26}$$

Two different methods are tested to handle flow over a dry bed. In the first method, a sufficiently small depth h_{dry} (e.g., 10^{-8} m) and zero velocity are defined at the dry nodes (Ying et al. 2004). At an element boundary, if water depth on one side is greater than h_{dry} and water depth on the other side is less than or equal to h_{dry}, the numerical flux is computed according to the dry bed location and flux function. If the water depths on both sides of the boundary are less than or equal to h_{dry}, the numerical flux in Equation (2.12) or Equation (2.16) would be zero. After every time step the water depth at every node is checked. If the water depth at a node is less than h_{dry}, the water depth is set to $h = h_{dry}$ and the flow rate is set to zero.

In the second method, zero depth and zero velocity are specified at all the dry nodes, and a small depth h_{dry} is used to check wet/dry front (Sanders, 2001). If the water depth on one side of an element face is larger than h_{dry} and the other side is less than h_{dry}, the numerical flux is calculated; if the water depths on both sides are less than h_{dry}, the numerical flux is set to zero. In the event that the computed water depth is less than h_{dry} (but positive), the velocity is set to zero. If the computed water depth is less than zero, both depth and velocity at the node are set to zero. The two methods are found to provide the same level of accuracy for the tests conducted in the one-dimensional case, and mass and momentum are conserved. The results shown in next chapter are based on the second method.

2.4 Runge-Kutta TVD time integration

To diminish oscillation for hyperbolic conservation laws, the TVD Runge-Kutta time integration is preferred (Gottlieb and Shu, 1998). Former studies have shown that the TVD Runge-Kutta time integration scheme should be one order higher than the space discretization (Cockburn and Shu, 1989; Cockburn et al., 1989; Cockburn et al., 1990). The second order TVD Runge-Kutta scheme is used here. Equations (2.9) and (2.10) can be written in the following form after numerical integration

$$\frac{\partial \mathbf{U}}{\partial t} = L(\mathbf{U}) \tag{2.27}$$

To advance the solution from time step t to $t+\Delta t$, the second order TVD Runge-Kutta scheme, as given by Gottlieb and Shu (1998), can be written as

$$\begin{cases} \mathbf{U}^{[1]} = \mathbf{U}^{t} + \Delta t L\left(\mathbf{U}^{t}\right) \\ \mathbf{U}^{t+\Delta t} = \dfrac{1}{2}\mathbf{U}^{t} + \dfrac{1}{2}\mathbf{U}^{[1]} + \dfrac{\Delta t}{2} L\left(\mathbf{U}^{[1]}\right) \end{cases} \tag{2.28}$$

For the explicit scheme adopted here, the Courant-Friedrichs-Lewy (CFL) condition must be fulfilled and is given by

$$\max\left[\frac{\Delta t}{\Delta x}\left(|u| + c\right)\right] \le \frac{1}{2p+1} \tag{2.29}$$

where p is the order of polynomial used for space discretization (Cockburn, 1999).

2.5 Slope limiting procedure

To achieve TVD property in a numerical scheme, flux limiters and slope limiters are often applied in combination with TVD time integration. Generally, the slope limiter

is applied to the water depth or water surface elevation in addition to discharge. This is generally satisfactory for rectangular channels. However, for natural channels the flow area is another alternative for applying the slope limiter. Here, the slope limiter is used on the variables A and Q. The flow area slope limiter is compared with the water depth and water surface elevation slope limiters.

In an element, the slope limiter for a variable ϕ can be written as

$$\phi(x) = \bar{\phi}_\ell + (x - x_{mp})\sigma_\ell ; \quad x_s \le x \le x_e \tag{2.30}$$

where $\bar{\phi}_\ell$ is the average value of a variable over an element and x_{mp} is the midpoint of the element. The variable ϕ can be water depth, water surface, cross-section flow area, or flow rate. The two values of ϕ, corresponding to $x = x_s$ and $x = x_e$, represent the values of a variable at the two nodes of an element. A monotonized central slope limiter (Li, 2006) is used, and for an element ℓ it can be written as

$$\sigma_\ell = \frac{\left(sign(a) + sign(b)\right)}{2} \min\left(\frac{|a+b|}{2}, 2|a|, 2|b| \right) \tag{2.31}$$

The upwind slope a, the downwind slope b, and the central slope $(a+b)/2$ are, respectively, given by

$$a = \frac{\bar{\phi}_\ell - \bar{\phi}_{\ell-1}}{(x_{\ell,mp} - x_{\ell-1,mp})} \tag{2.32}$$

$$b = \frac{\bar{\phi}_{\ell+1} - \bar{\phi}_\ell}{(x_{\ell+1,mp} - x_{\ell,mp})} \tag{2.33}$$

$$\frac{a+b}{2} = \frac{\bar{\phi}_{\ell+1} - \bar{\phi}_{\ell-1}}{(x_{\ell+1,mp} - x_{\ell-1,mp})} \tag{2.34}$$

where $x_{\ell,mp}$ is the midpoint of element ℓ and so on.

The procedure to apply the slope limiter on cross-section A and flow rate Q is briefly described below. First, A and Q are determined at the end nodes for each element in the domain using Equations (2.9) and (2.10). Next, the limiter variable ϕ (A and Q) is calculated for each element using Equation (2.30). Finally, the water surface Z or water depth h is computed from A based on the channel cross-section geometry. In case of water depth or water surface slope limiter, the first step is the same as above. In the next step, the water depth or water surface for each node is computed from the cross-sectional flow area and the limiter variable ϕ (Z or h) is calculated for each element. Finally, the area is calculated from water surface Z or water depth h based on channel geometry.

CHAPTER THREE

NUMERICAL TESTS FOR ONE-DIMENSIONAL FLOWS

In this chapter, the one-dimensional numerical model with the RKDG method is validated through a number of numerical tests, including idealized dam-break, wetting and drying in a parabolic bowl, hydraulic jump in a divergent channel, partial dam-break, and flows in natural rivers. Numerical results are compared with analytic solutions or measured data to evaluate the performance of the model.

3.1 Dam-break in a triangular channel

A classical dam-break problem in a frictionless, horizontal, triangular channel is simulated. The channel is 1000 m long with side slope of 1H:1V (Sanders, 2001). The dam was located at the middle of the channel. Both wet bed and dry bed conditions downstream of the dam are considered. The upstream water depth was 1 m for both cases, and the downstream water depth was 0.1 m for the wet bed test. For the wet bed case, 400 elements are used with $\Delta x = 2.5$ m and $\Delta t = 0.125$ s. For the dry bed test, 1000 elements are used with $\Delta x = 1$ m, $\Delta t = 0.05$ s, and $h_{dry} = 10^{-16}$ m. The wet bed test results for the water surface elevation and flow rate are shown in Figure 3.1 and Figure 3.2 at 80 s after the dam removal. The dry bed test results for water surface elevation and velocity are shown in Figure 3.3 and Figure 3.4 at 45.16 s after the dam removal.

Throughout this work, 'HLL-Z' means the HLL flux is adopted and the slope limiter is applied to the water surface. Similarly, 'A' and 'h' signify that the slope limiter

is applied to the flow area and water depth, respectively. For a horizontal channel, water surface and water depth slope limiters will produce identical results. The exact solution for dam-break problems in a horizontal channel of any shape can be found in Henderson (1966).

Results in Figure 3.1 and Figure 3.2 show that the numerical results with slope limiter on flow area are in good agreement with the exact solution for both flux functions and capable of capturing the shock accurately. The water surface based slope limiter produces errors in wave speed, wave amplitude, and flow rate with both flux functions. The HLL and Roe flux functions provided similar results for all other tests as well. From here onward, only results for HLL flux are shown for easier interpretation.

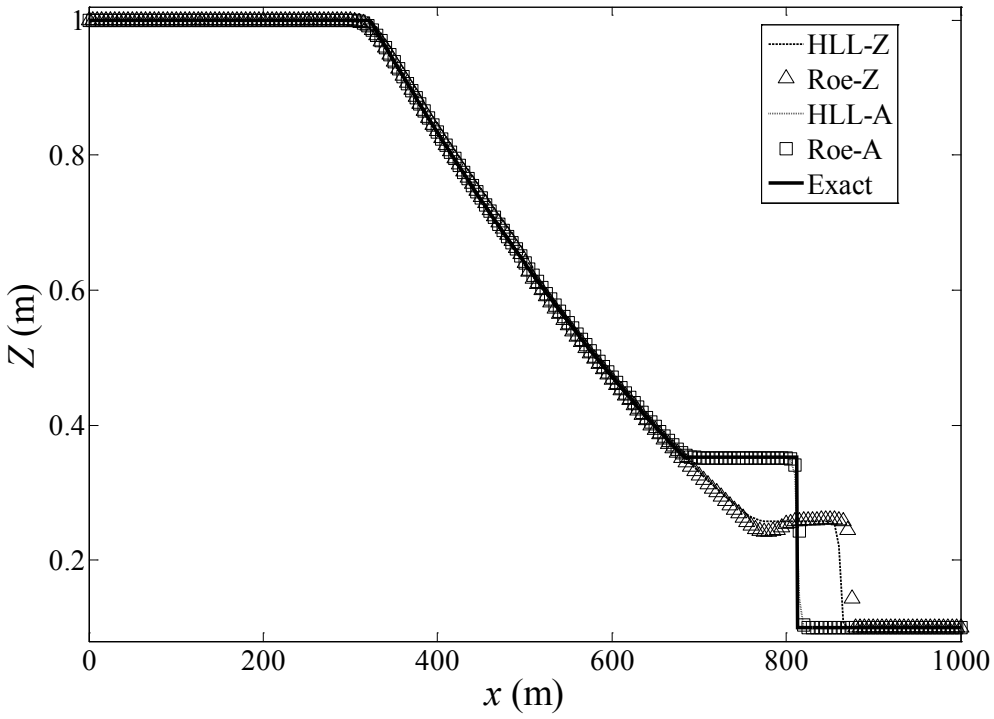

Figure 3.1 Comparison of water surface for dam-break problem in triangular channel

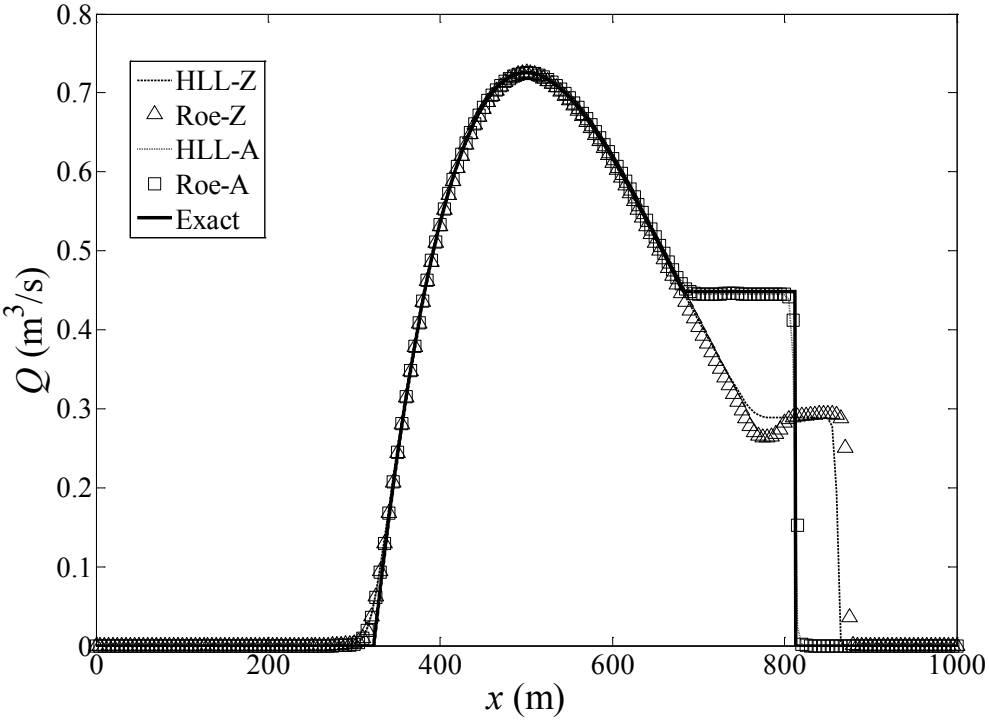

Figure 3.2 Comparison of flow rate for dam-break problem in a triangular channel

For the dry bed test in the triangular channel, the water surface based slope limiter failed to provide results for the grid size and time step size mentioned before. It is found that a minimum water depth of 0.007 m as initial condition downstream of the dam and a reduced time step of 0.00025 s have to be used for the water surface based slope limiter to work. The results for the water depth (Figure 3.3) show that the small initial downstream depth changes the solution at the leading edge of the wave. In the case of water surface slope limiter a shock is visible at the leading edge of the wave front. The area based slope limiter scheme is capable of capturing the leading edge of the wave front. The dependency of results on the mesh size is shown in Figure 3.5 and Figure 3.6 with HLL-A scheme. As predicted, higher resolution provides more accurate results.

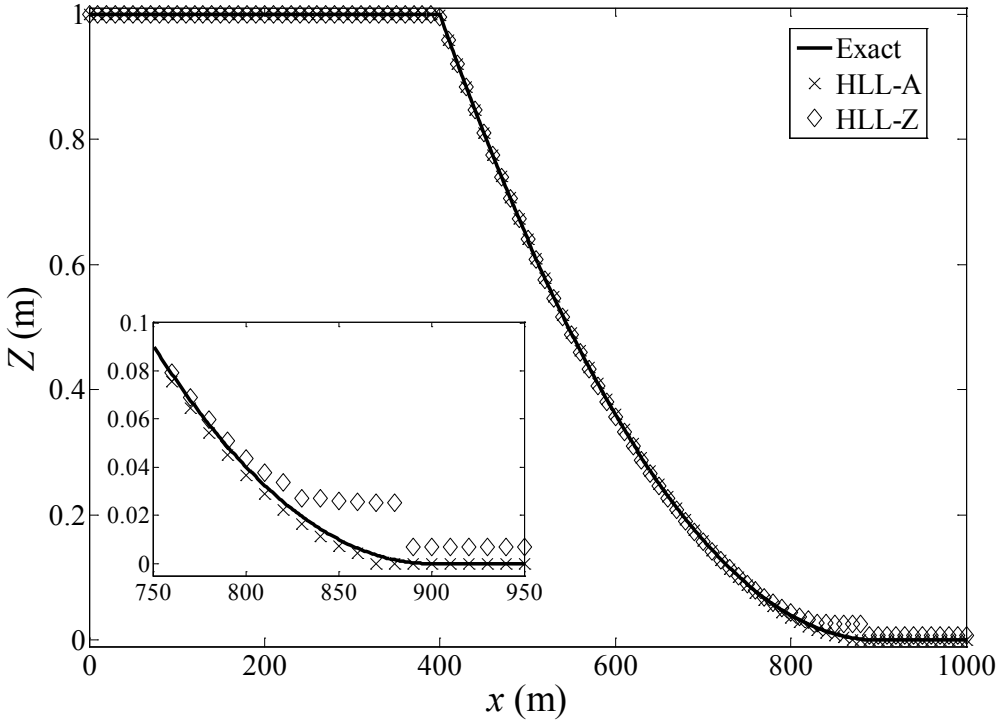

Figure 3.3 Comparison of water surface for dry bed dam-break in triangular channel

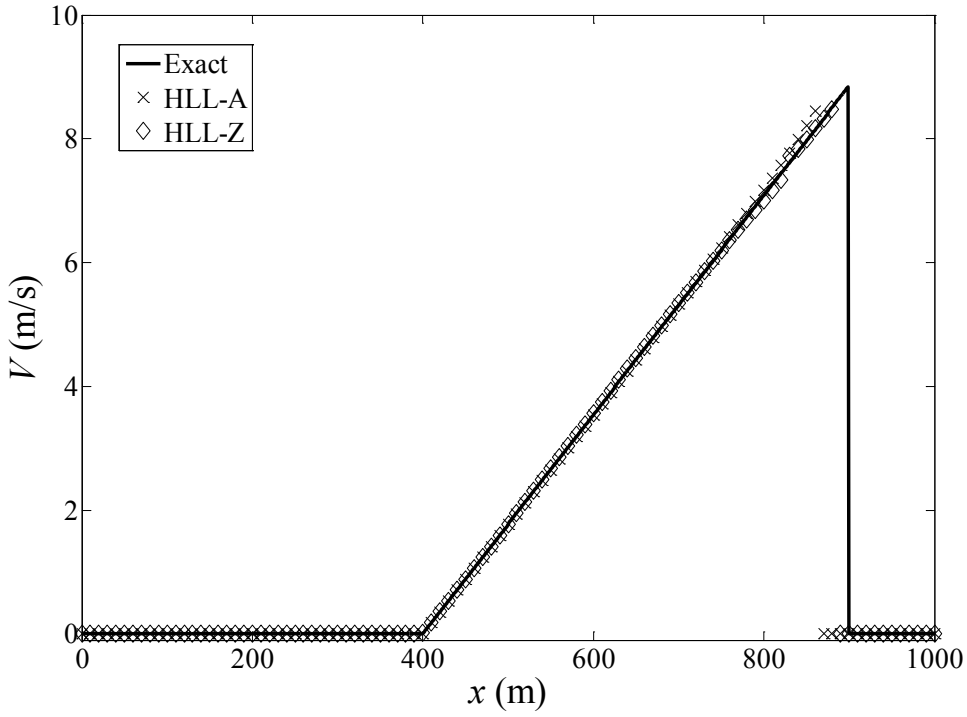

Figure 3.4 Comparison of flow velocity for dry bed dam-break in triangular channel

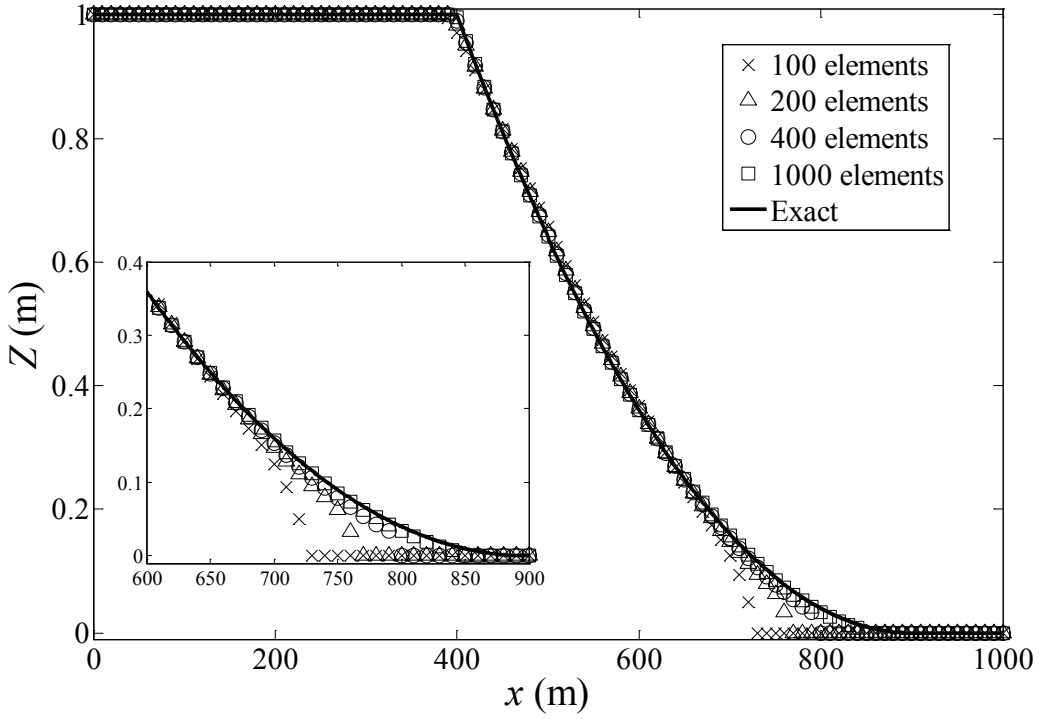

Figure 3.5 Water surface for dry bed problem in triangular channel with different mesh

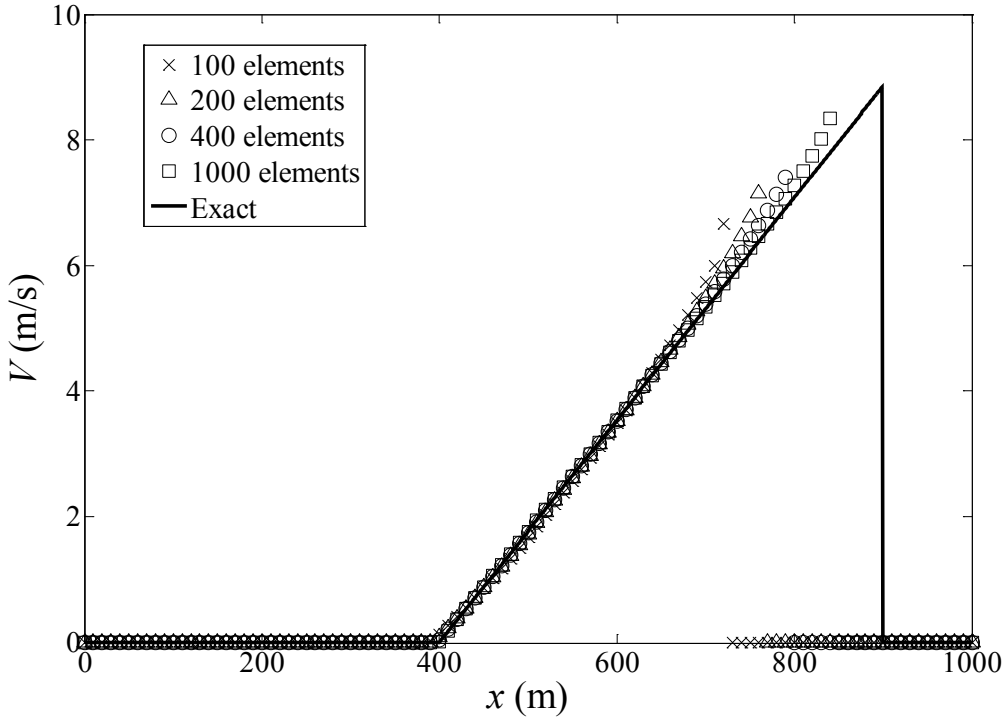

Figure 3.6 Velocity for dry bed problem in triangular channel with different mesh

3.2 Dam-break in a parabolic channel

In this test, a 1000 m long horizontal, frictionless, parabolic channel with top width $b = h^{0.5}$ is used. The dam was located at 500 m from the upstream end of the channel. The water depth upstream of the dam was 1.0 m and downstream water depth was 0.1 m. The test is run using 400 elements with $\Delta x = 2.5$ m and $\Delta t = 0.125$ s. Numerical solutions of water surface and flow rate at 100 s after the removal of the dam are shown in Figure 3.7 and Figure 3.8, respectively.

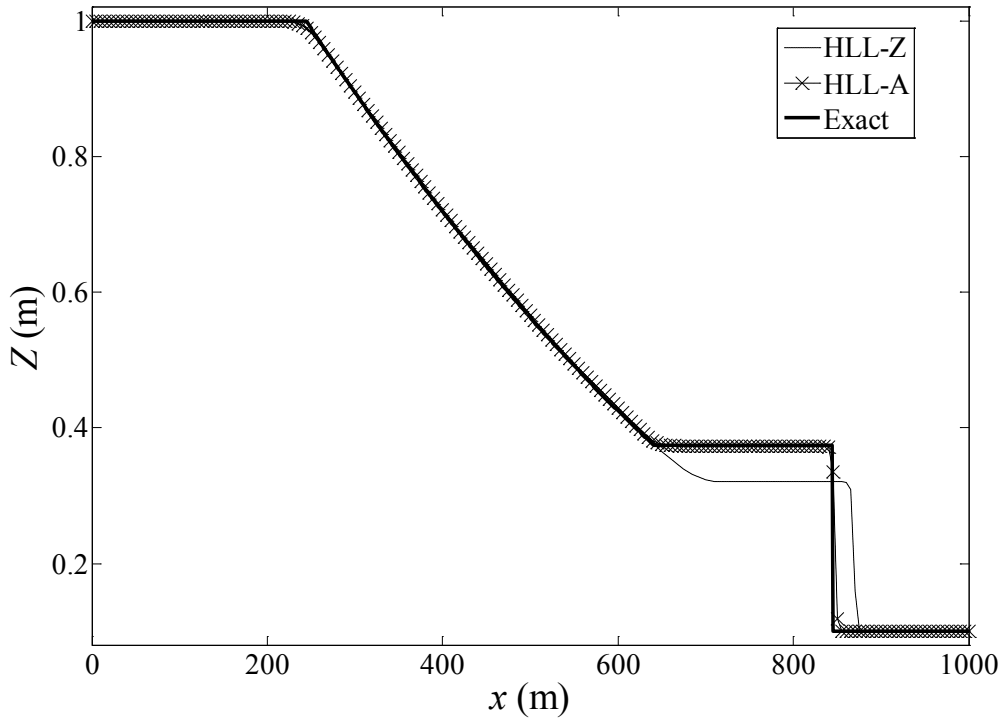

Figure 3.7 Comparison of water surface for dam-break problem in a parabolic channel

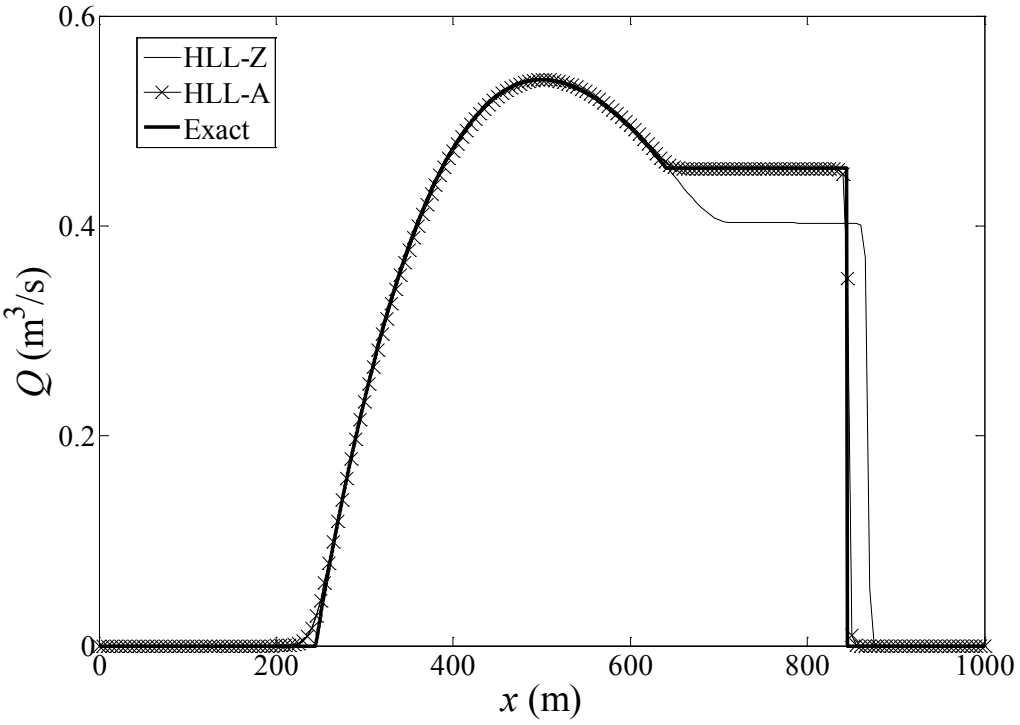

Figure 3.8 Comparison of flow rate for dam-break problem in a parabolic channel

Numerical results in the parabolic channel show similar performance to that in a triangular channel with the flow area slope limiter providing results that are more accurate. As can be observed from the results, the water surface slope limiter incurs less error for a parabolic channel than in a triangular channel.

3.3 Dam-break in a trapezoidal channel

In this test, the classical dam-break problem is simulated in a horizontal, frictionless, trapezoidal channel. The channel has a length of 1000 m with side slope of 2H:1V ($\beta = 2$) and bottom width of 1 m. The dam was located at the middle of the channel. Initially the upstream water depth was 1 m, and the downstream water depth

was 0.1 m (Sanders, 2001). The test is run using 400 elements with $\Delta x = 2.5$ m and $\Delta t = 0.125$ s. The numerical solutions at 103.1 s after the dam removal for water surface and flow rate are presented in Figure 3.9 and Figure 3.10, respectively. The results show similar trend as for triangular and parabolic channels. As before, the flow area slope limiter gives numerical results in agreement with the exact solution, while the water surface slope limiter generates larger errors. However, the errors in the water surface and flow rate are less than the previous two tests.

Further investigations show that as the side slope (β) decreases, the differences between the results based on the flow area and water surface slope limiters decrease. That is, as the channel cross-section deviates from rectangular channel the differences in the results based on the two slope limiters increase. It is obvious and as shown in the next test, the two slope limiters are mathematically the same and provide exactly the same results for a rectangular, prismatic channel.

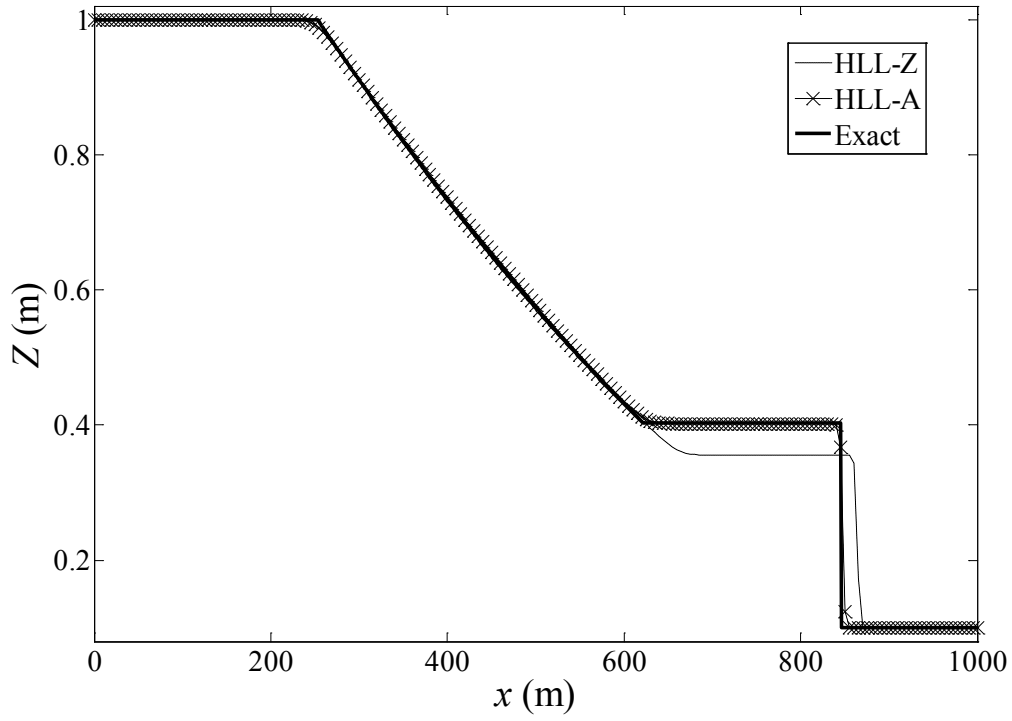

Figure 3.9 Comparison of water surface for dam-break problem in a trapezoidal channel

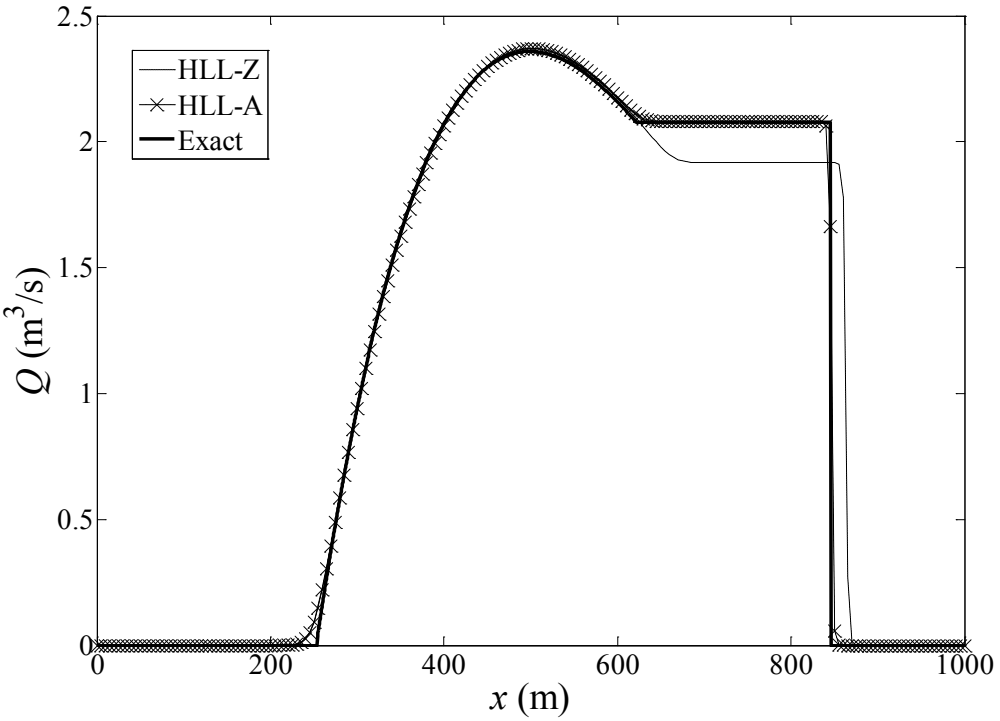

Figure 3.10 Comparison of flow rate for dam-break problem in a trapezoidal channel

3.4 Dam-break in a rectangular channel

As discussed before, the results obtained from the two slope limiters should be the same for a rectangular, horizontal, prismatic channel for both dry and wet bed conditions. A horizontal, frictionless, rectangular channel is considered in this test. The channel is 1200 m long and 10 m wide. The dam was located at 500 m from upstream end of the channel. The upstream water depth was 10 m and downstream water depth was set to 2 m. In this test, 120 elements are used with $\Delta x = 10$ m and $\Delta t = 0.25$ s. Numerical solutions for the water surface and flow rate at 30 s after dam removal are shown in Figure 3.11 and Figure 3.12, respectively.

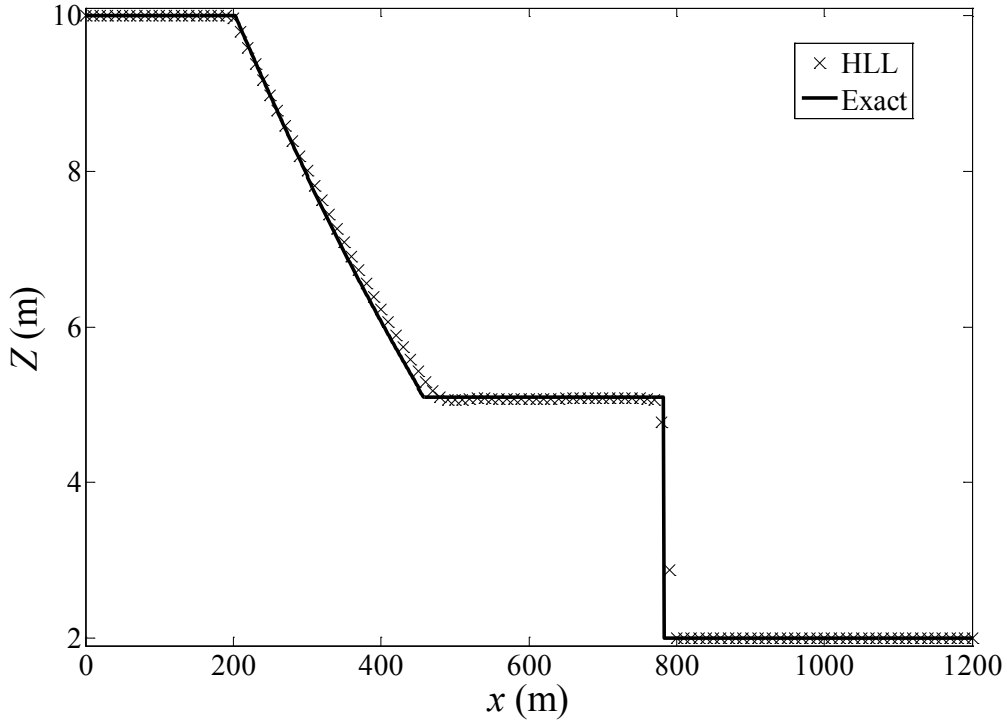

Figure 3.11 Comparison of water surface for dam-break problem in a rectangular channel

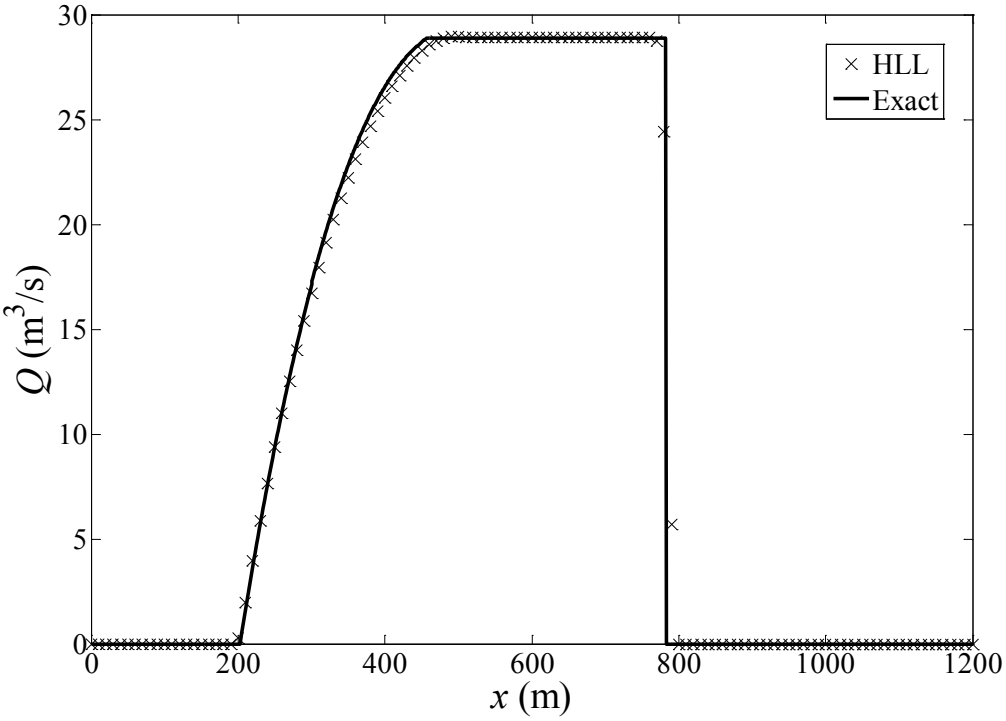

Figure 3.12 Comparison of flow rate for dam-break problem in a rectangular channel

The accuracy of the results obtained using the two slope limiters for the previous four prismatic channels are shown in Table 3.1. The average error is based on the difference between the predicted and analytical water surface levels over the whole domain. The flow cross-section is shown as functions of water depth. As the exponent of the depth decreases, the accuracy of the results obtained using water surface slope limiter improves.

Table 3.1 Accuracy of slope limiters in prismatic channels

Channel Type	Area (A)	Order of h	Average Error of Z Limiter	Average Error of A Limiter
Triangular	h^2	2	12.0%	1.2%
Parabolic	$(2/3)h^{3/2}$	1.5	6.8%	1.1%
Trapezoidal	$bh+\beta h^2$	1~2	6.0%	1.2%
Rectangular	bh	1	1.0%	1.0%

3.5 Dam-break in a rectangular flume with friction

In this test, the numerical model is applied to a dam-break problem in a rectangular, horizontal flume for which measured water surface profiles after the dam-break event are available (Schoklitsch, 1917). The flume used was 0.096 m wide, 0.08 m high and 20 m long. The dam was located at the middle of the flume, with water ponded to a height of 0.074 m upstream of the dam and a dry bed downstream. The flume was made of smooth wood. The Manning's roughness coefficient of 0.009 $s/m^{1/3}$ is used in the simulation. The removal of the dam is assumed instantaneous, and the water flow after the dam removal is simulated. Element size of 0.1 m and time step of 0.0001 s are used in this test.

Figure 3.13 shows the computed water surface profiles with measured data at 3.75 seconds and 9.40 seconds after the removal of the dam. The computed water surface profiles are in good agreement with the measured profiles. The results show that the scheme is capable of modeling the progressive wave after the dam removal over an initially dry bed with friction.

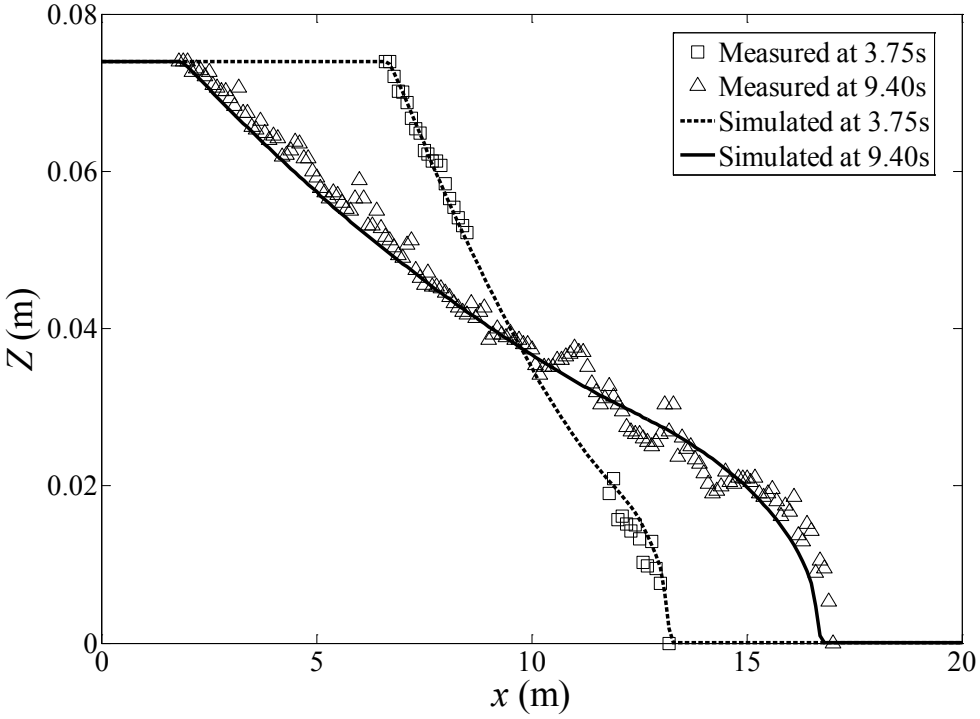

Figure 3.13 Computed and measured water surface at 3.75 s and 9.40 s

3.6 Wetting and drying in a parabolic bowl

Thacker (1981) derived analytical solutions for the one-dimensional shallow water flow equations in a frictionless, parabolic bowl with a moving shoreline. The analytic solutions are useful for testing the wetting and drying capability of numerical schemes of the shallow water flow equations (Xing et al., 2010).

The parabolic bed profile of the domain is defined by

$$z_b(x) = h_o\left(\frac{x^2}{a^2} - 1\right) \tag{3.1}$$

with constants h_0 and a as shown in Figure 3.14. In the region where water depth is nonzero, the analytic solutions for the water surface and velocity are given, respectively, as

$$Z(x,t) = \frac{-B^2\cos(2\omega t) - B^2 - 4B\omega\cos(\omega t)x}{4g} \tag{3.2}$$

$$u(x,t) = B\sin(\omega t) \tag{3.3}$$

where B is a constant and

$$\omega = \frac{2\pi}{T} = \frac{\sqrt{2gh_o}}{a} \tag{3.4}$$

The location of the moving shoreline is given by

$$x = -\frac{a^2\omega B}{2gh_o}\cos(\omega t) \pm a \tag{3.5}$$

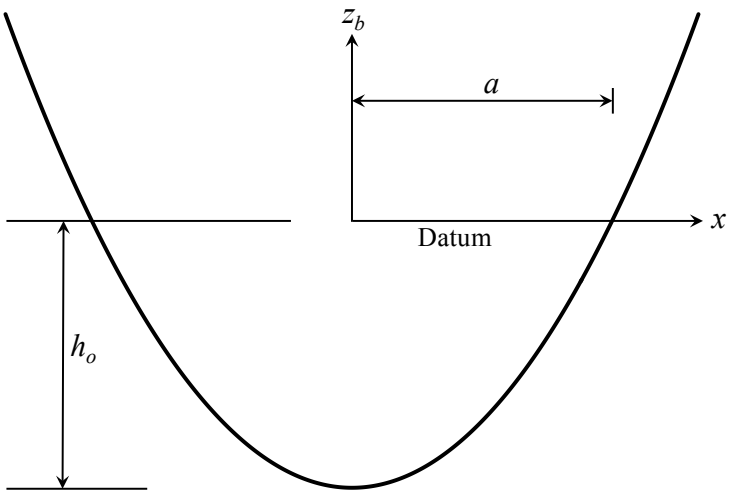

Figure 3.14 Parabolic bowl bed profile

The constants used in this test are $a = 2500$ m, $h_o = 10$ m, and $B = 5$ m/s, which give the oscillation period of $T = 1121$ s, and the parabolic bowl is of unit width. The computational domain extends from -4000 m to 4000 m and 100 elements are used with $\Delta x = 80$ m and $\Delta t = 1.121$ s. The dry bed criterion (h_{dry}) of 10^{-2} m is used. The initial water surface and velocity are given by Equations (3.2) and (3.3). The simulation is conducted for one full period. The numerical results for the water surface and flow rate are shown in Figures 3.15-3.18 and Figures 3.18-3.22, respectively. Results show that the area based slope limiter gives a better solution than that based on water surface, and the scheme with area slope limiter is capable of conserving mass and momentum during the wetting and drying episodes. Water volume calculated at different times is the same as the initial volume with area slope limiter.

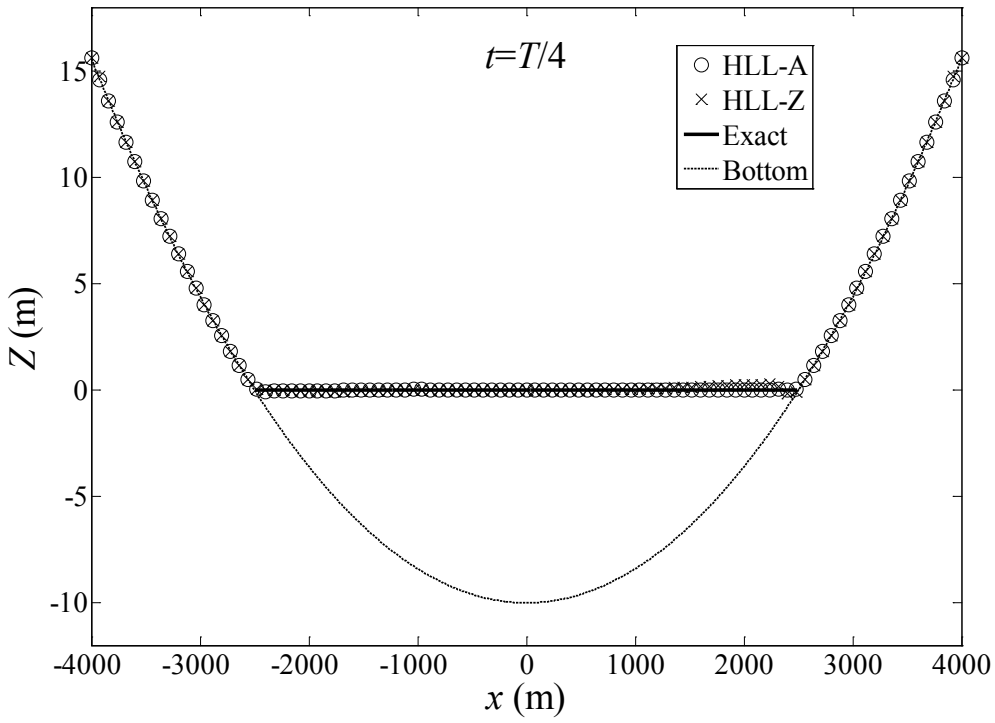

Figure 3.15 Comparison of water surface in the parabolic bowl at $t=T/4$

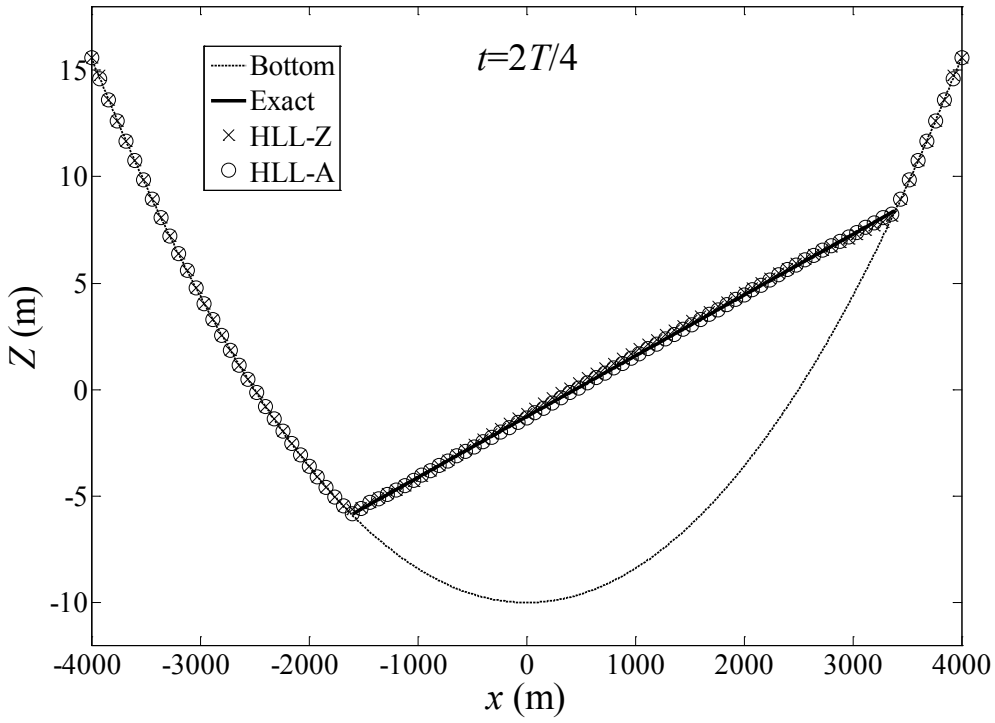

Figure 3.16 Comparison of water surface in the parabolic bowl at $t=2T/4$

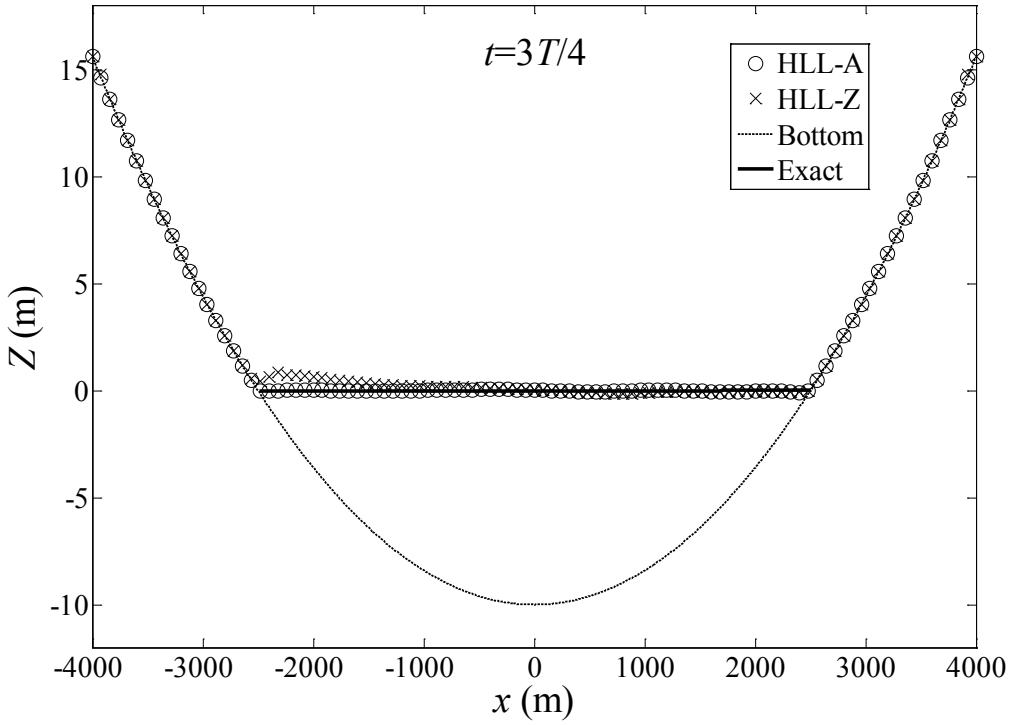

Figure 3.17 Comparison of water surface in the parabolic bowl at $t=3T/4$

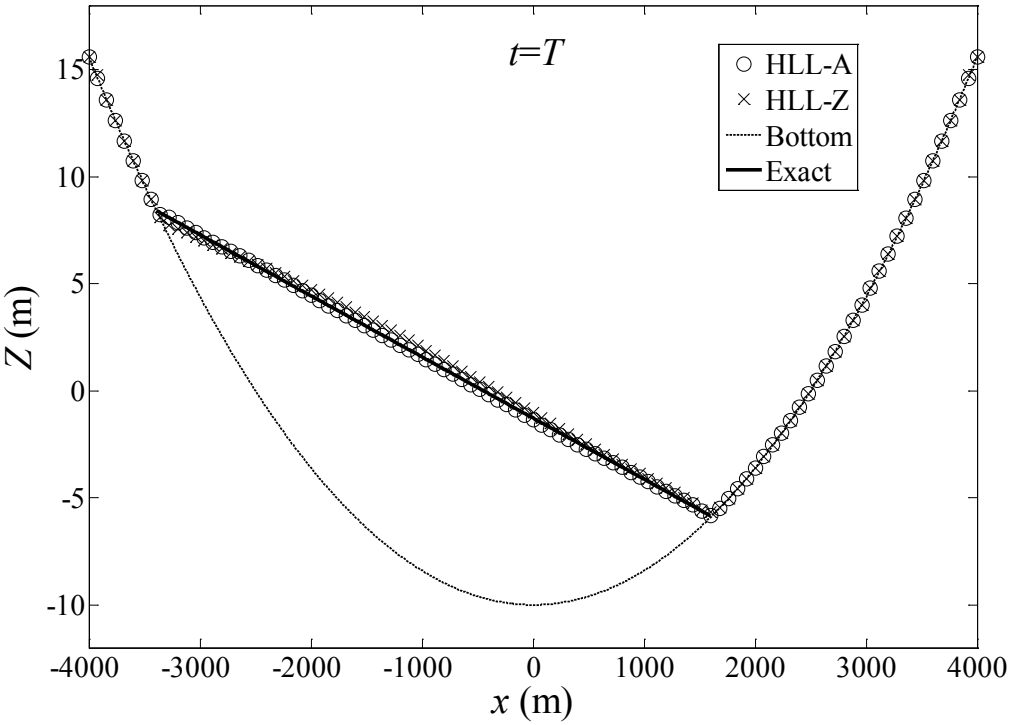

Figure 3.18 Comparison of water surface in the parabolic bowl at $t=T$

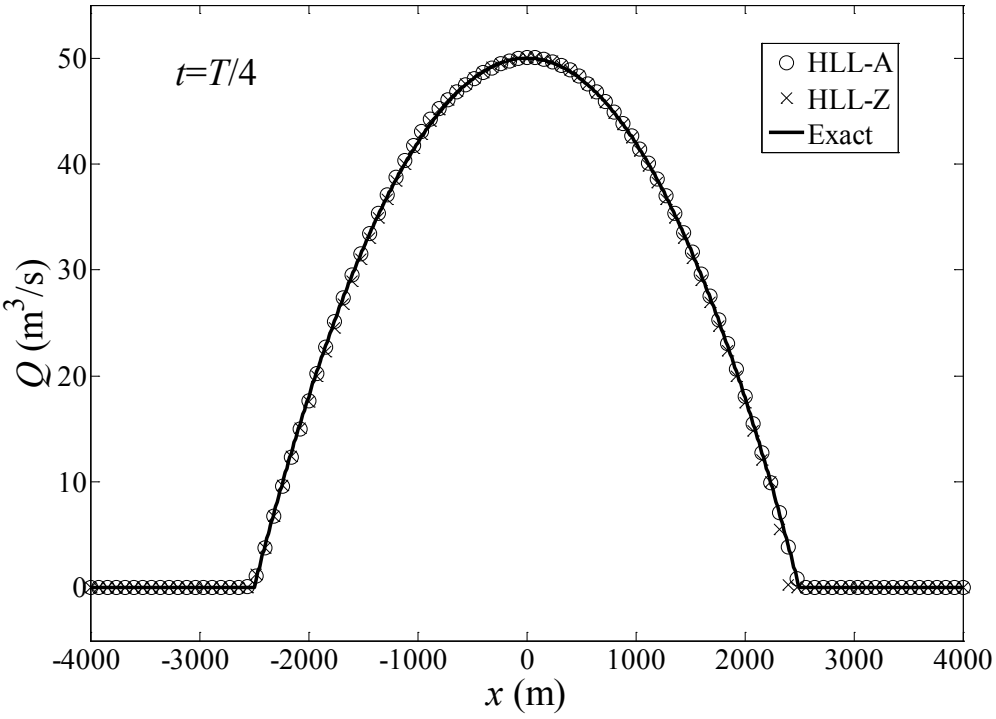

Figure 3.19 Comparison of flow rate in the parabolic bowl at $t=T/4$

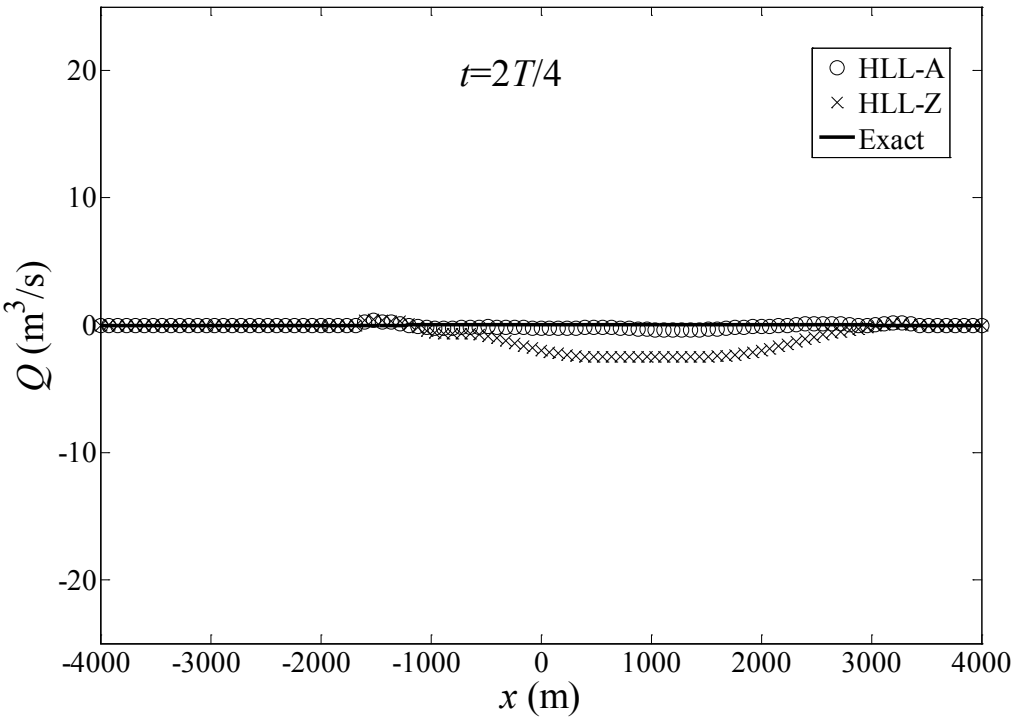

Figure 3.20 Comparison of flow rate in the parabolic bowl at $t=2T/4$

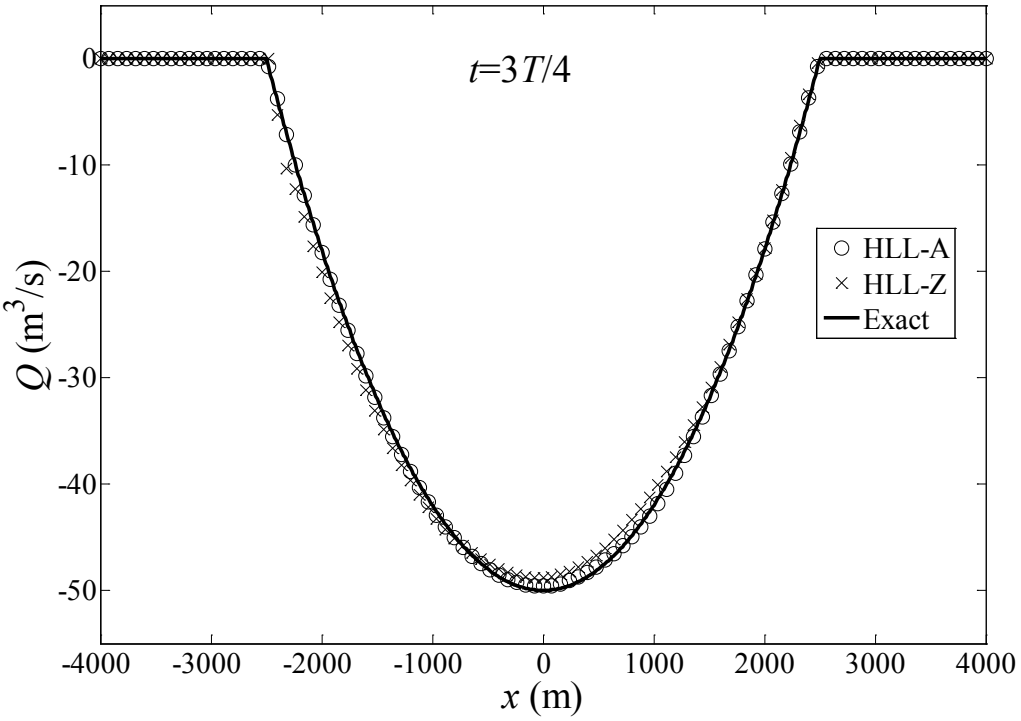

Figure 3.21 Comparison of flow rate in the parabolic bowl at $t=3T/4$

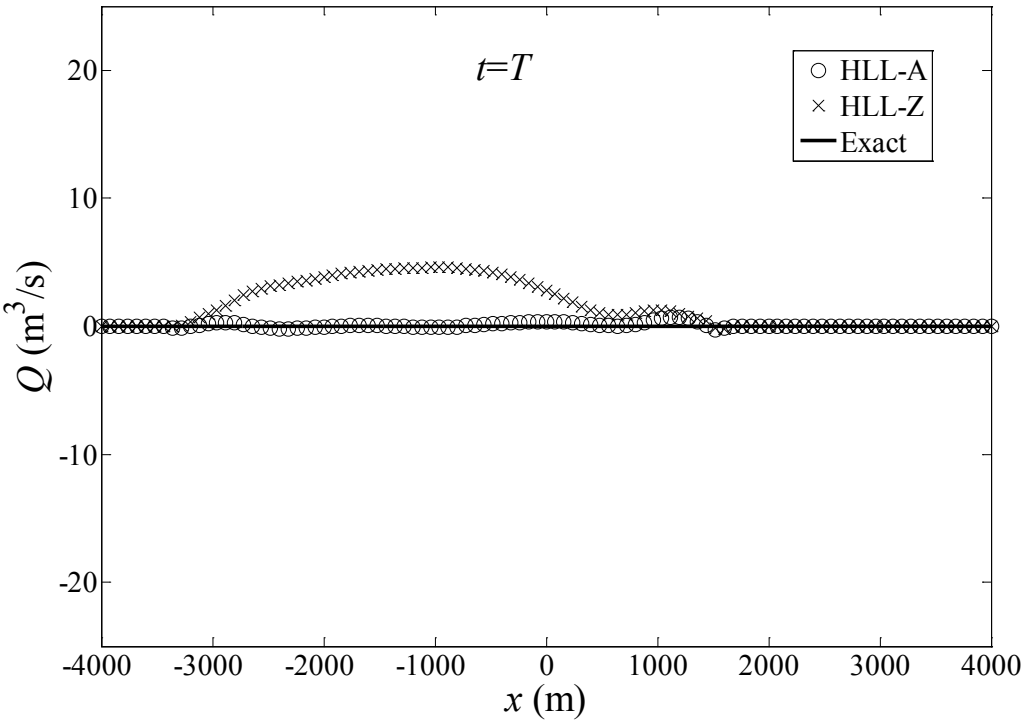

Figure 3.22 Comparison of flow rate in the parabolic bowl at $t=T$

3.7 Hydraulic jump in a rectangular channel

Gharangik and Chaudhry (1991) undertook a physical model study to measure water surface profiles of hydraulic jumps for various upstream and downstream boundary conditions. The study was conducted in a 14 m long and 0.46 m wide rectangular, horizontal flume. Two cases (labeled as 'a' and 'b') are selected to validate the current model. For the cases 'a' and 'b', the upstream velocities were 3.831 m/s and 1.826 m/s, the upstream depths were 0.031 m and 0.064 m, and downstream depths were 0.265 m and 0.168 m, respectively. These conditions correspond to upstream Froude numbers of 6.947 and 2.305, and downstream Froude numbers of 0.278 and 0.542, respectively. The given discharge and upstream water depth are used as upstream boundary conditions (compatible with supercritical flow at the upstream end of the channel). At the downstream end, the water depth maintained in the physical model at the end of the channel is used as a boundary condition. The initial condition for the water surface is set by linearly varying the water depth between the inlet and outlet. The Manning's roughness coefficient is set to 0.008 $s/m^{1/3}$.

The final computed water surface and flow rate for the two cases are shown in Figure 3.23 and 3.24, respectively. Element size of 0.1 m and time step of 0.002 s are used in this test. Figure 3.23 shows that the locations and water surface profiles for the two hydraulic jumps are predicted accurately by the model. In Figure 3.24, small oscillations at the toe of the jumps are observed in the discharge and may be due to the breakdown of the hydrostatic pressure assumption. Overall, the scheme is capable to model hydraulic jumps accurately.

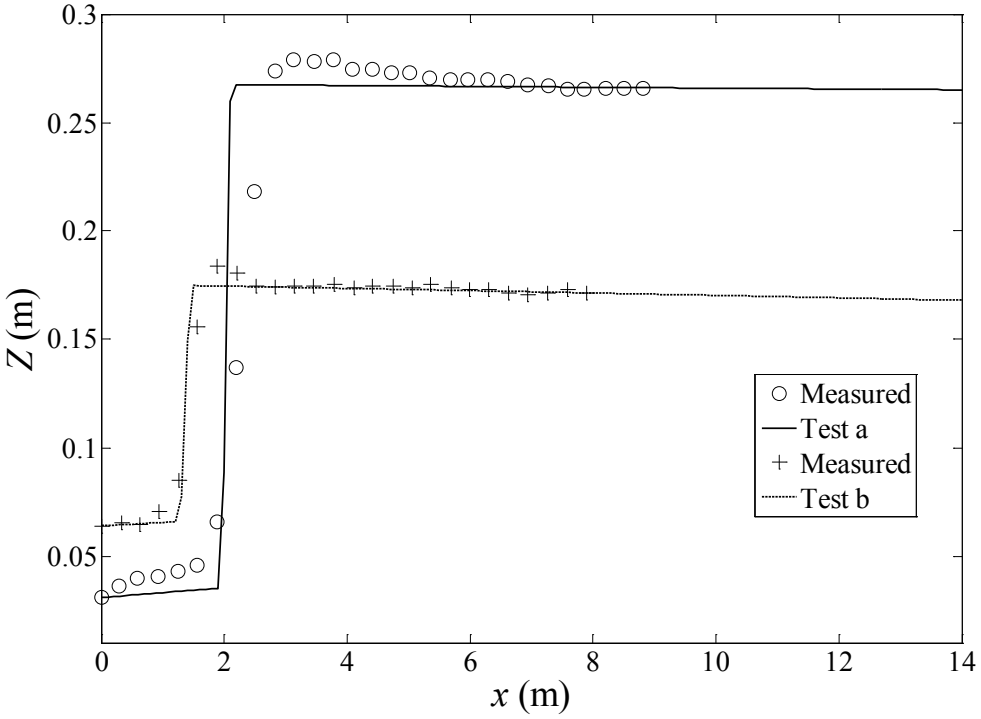

Figure 3.23 Computed and measured water surface profiles for hydraulic jumps

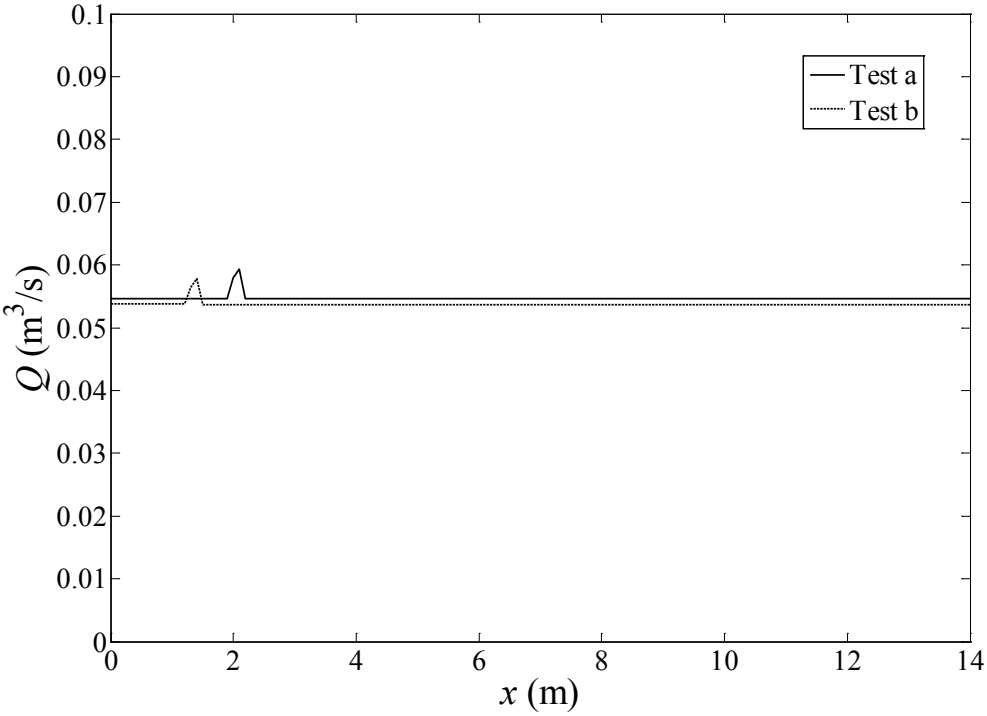

Figure 3.24 Computed flow rate variation for hydraulic jumps

3.8 Hydraulic jump in a divergent channel

Khalifa (1980) measured water surface profiles in hydraulic jumps in a divergent channel. The experiments were performed in a 2.5 m long horizontal channel with a rectangular cross-section. The channel width (m) was given as

$$b(x) = \begin{cases} 0.155; & 0 \le x \le 0.65 \\ 0.155 + 0.236\left(x - 0.65\right); & 0.65 < x < 1.94 \\ 0.46; & 1.94 \le x \le 2.5 \end{cases} \tag{3.6}$$

The inlet discharge was set at 0.0263 m^3/s and the upstream water depth was maintained at 0.088 m to impose a supercritical flow condition. The water depth at the downstream boundary was 0.195 m, ensuring that a hydraulic jump would form in the diverging section of the channel. The above conditions are used to simulate the physical model test. The test is simulated using a time step size of 0.00375 s and a constant element size of 0.025 m.

Numerical results along with the measured data are shown in Figure 3.25 and Figure 3.26. The computed water surface profiles are compared with the measured data along the centerline. The jump location and water surface profile are well predicted using the one-dimensional model. The flow rate is conserved by both schemes as shown in Figure 3.26.

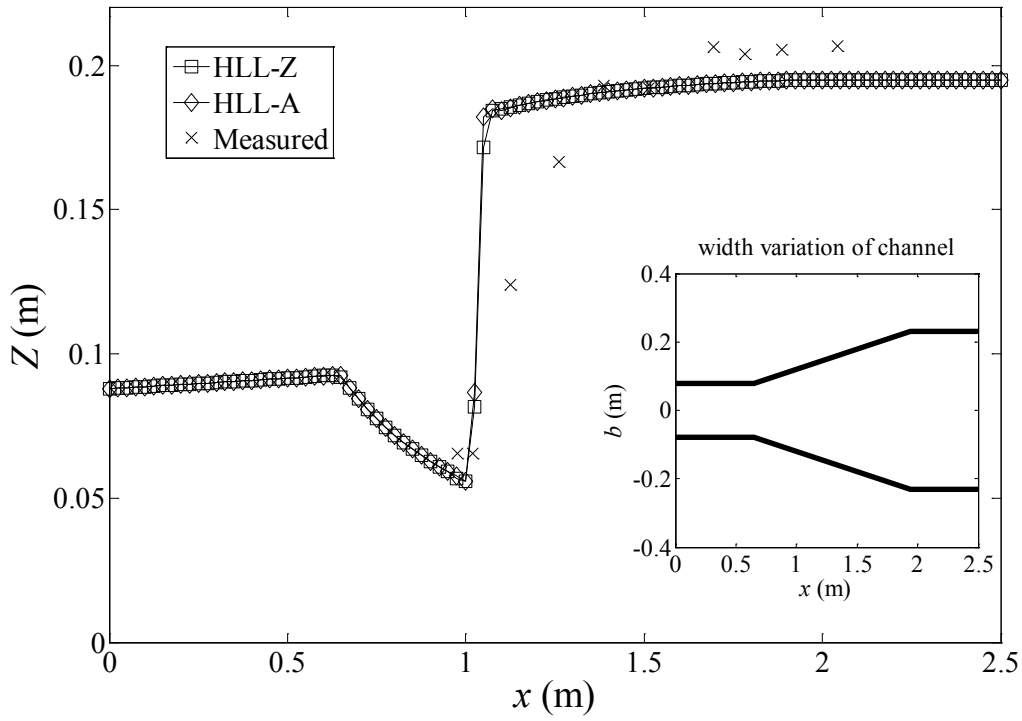

Figure 3.25 Comparison of water surface for hydraulic jump in a divergent channel

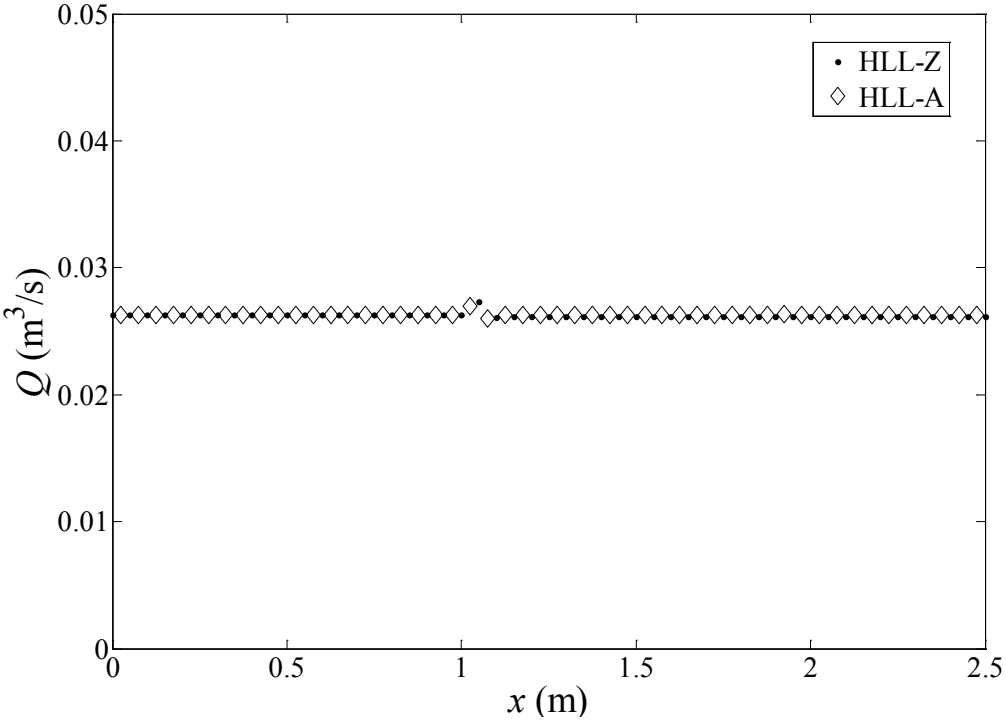

Figure 3.26 Comparison of flow rate for hydraulic jump in a divergent channel

3.9 Dam-break in a converging/diverging flume

Bellos et al. (1992) conducted a variety of experiments to investigate the movement of two-dimensional flood waves after an instantaneous dam-break in a converging/diverging channel. The authors conducted various experiments for different bed slopes under both wet and dry bed conditions. The flume had a rectangular cross-section with variable width. A gate was installed at the minimum width of the flume $(x = 8.5 \text{ m})$. The geometry of the flume is provided in Table 3.2 and the plan view is shown in Figure 3.27. The wet-bed and dry-bed numerical tests with horizontal bed are used in this study. Based on the experiment data, the depth upstream of the gate is set to 0.30 m for both cases, and the downstream depth for wet bed case is 0.101 m. The Manning's roughness coefficient is chosen to be 0.012 $s/m^{1/3}$. Element size of 0.1 m is used for both cases. The time step sizes of 0.003 s for wet bed and 0.0002 s for dry bed problems are used. The dry bed criterion of 10^{-4} m is used in this test. Numerical results are compared with data collected in the physical model tests at four observational stations located at $x = 0$ m, 4.5 m, 13.5 m, and 18.5 m.

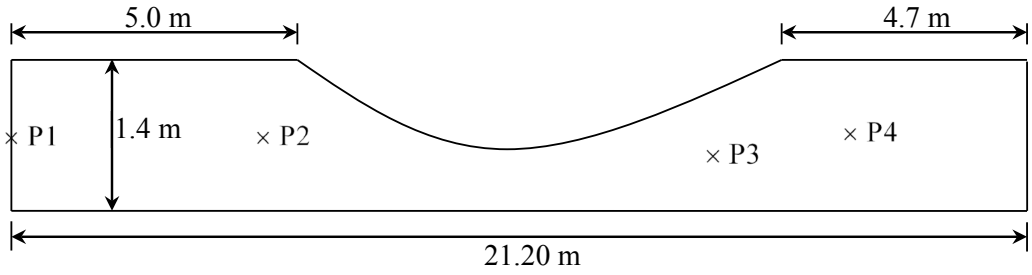

Figure 3.27 Geometry of converging/diverging flume

Table 3.2 Channel width variation for converging/diverging flume

***x* (m)**	0.0	5.0	5.5	6.0	6.5	7.0	7.5	8.0	8.5
***b* (m)**	1.4	1.4	1.22	1.05	0.90	0.77	0.67	0.62	0.60
***x* (m)**	9.0	9.5	10.0	10.5	11.0	11.5	12.0	12.5	13.0
***b* (m)**	0.61	0.62	0.64	0.68	0.75	0.82	0.91	0.99	1.08
***x* (m)**	13.5	14.0	14.5	15.0	15.5	16.1	16.5	21.2	
***b* (m)**	1.15	1.24	.28	1.33	1.37	1.39	1.40	1.40	

Numerical results for the dry bed test are shown in Figure 3.28 for observational stations P1 and P4 along with the available measured data. Numerical results for the wet bed test are shown in Figure 3.29 for observational station P2 and P3. In Figure 3.28, numerical results provide accurate results for the dry bed test. In Figure 3.29, numerical results have small oscillations at locations where the water surface changes rapidly. In general, all the schemes are capable of accurately simulating both dry bed and wet bed conditions in this test.

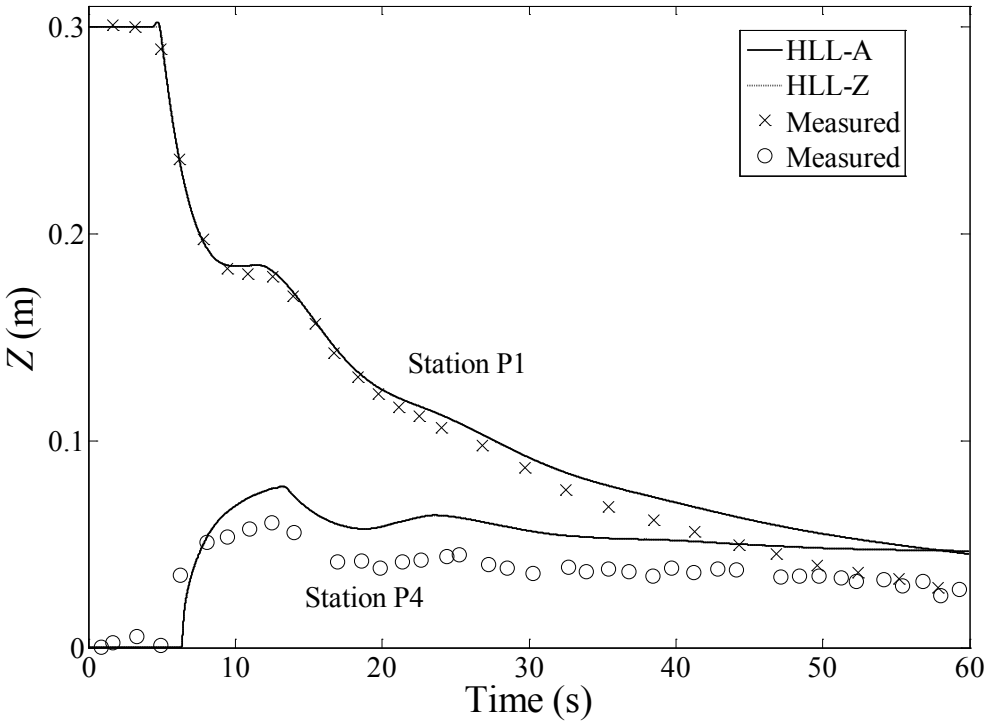

Figure 3.28 Water surface at P1 and P4 for dry bed case in converging/diverging flume

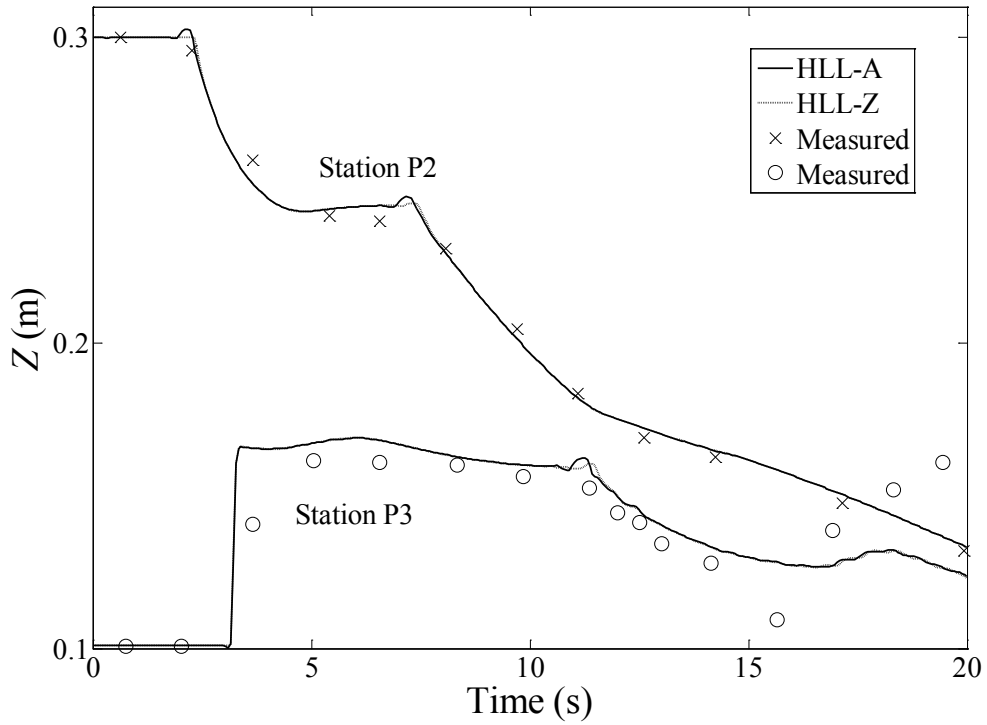

Figure 3.29 Water surface at P2 and P3 for wet bed case in converging/diverging channel

3.10 WES partial dam-break

Hydraulic experiments for a partial dam-break with minimum bed resistance were conducted at the Waterways Experiments Station (WES) by the U.S. Army Corps of Engineers (1960) are used to compare the accuracy of the numerical model for real world partial dam-break scenarios. The test flume was 121.92 m (400 ft) in length, 1.2192 m (4 ft) in width, with bed slope of 0.005. The 0.3048 m (1 ft) high dam was located in the middle of the flume. The water surface upstream was initially as high as the top of the dam, while the bed was dry downstream. Following Khan (2000), the Manning's coefficient is taken to be 0.009 s/m$^{1/3}$ for the minimum bed resistance case. The domain is discretized using 484 elements with $\Delta x = 0.25$ m and $\Delta t = 0.0125$ s. The dry bed criterion (h_{dry}) of 10^{-4} m is used in this test. Based on the experimental conditions, the width of the partial dam opening is set to 0.7315 m (2.4 ft). The channel configuration is illustrated in Figure 3.30.

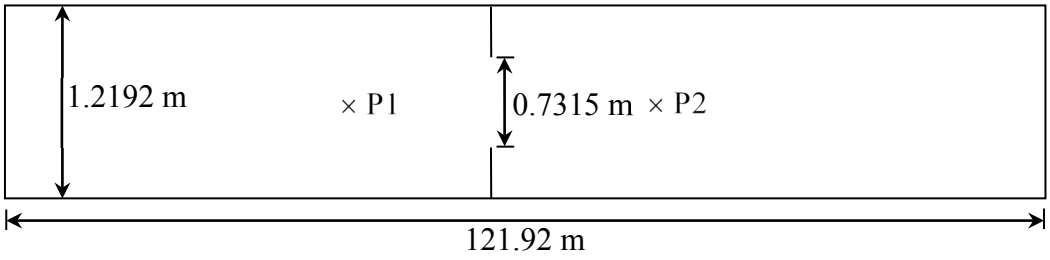

Figure 3.30 Channel configuration of WES partial dam-break test

Numerical results for the water surface level variation with time at stations 6.096 m (20 ft) upstream (P1) and 7.62 m (25 ft) downstream (P2) of the dam are shown in Figure 3.31. The wave front arrival time is predicted accurately by all schemes with different slope limiters. However, the water surface profile at P1 is under predicted by the water surface and water depth based slope limiters. In Figure 3.32, a comparison between computed and measured velocity profiles at P2 is presented. Numerical results are in good agreement with the measured data with the area based slope limiter providing better performance. The higher velocity predicted at the beginning may be due to the initial conditions related to dam removal.

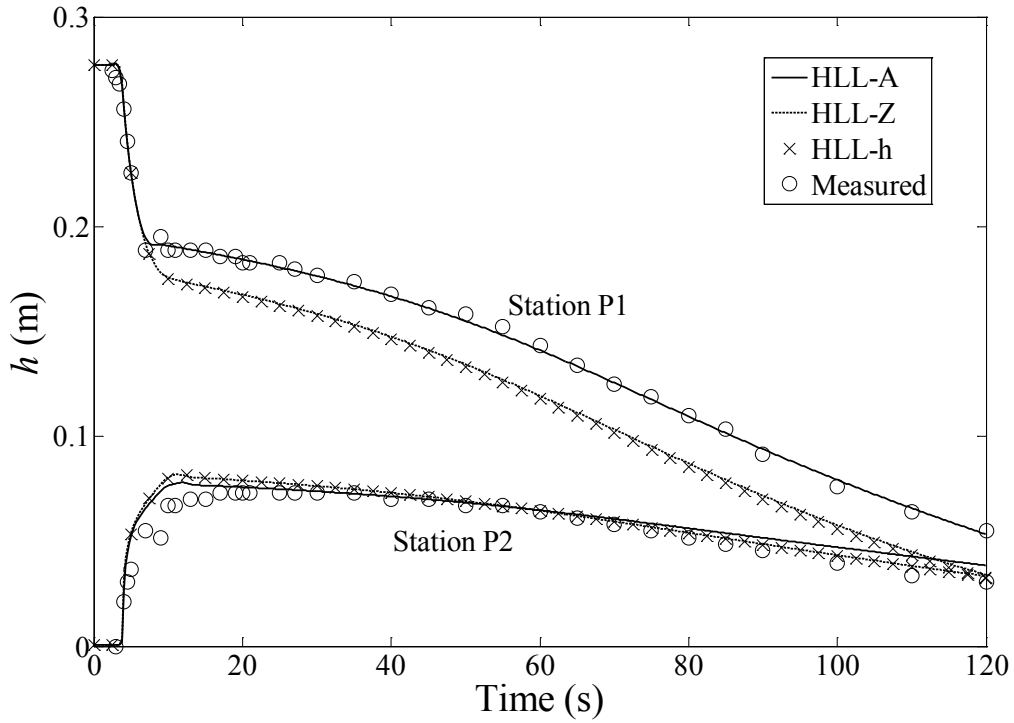

Figure 3.31 Water surface at P1 and P2 for WES partial dam-break

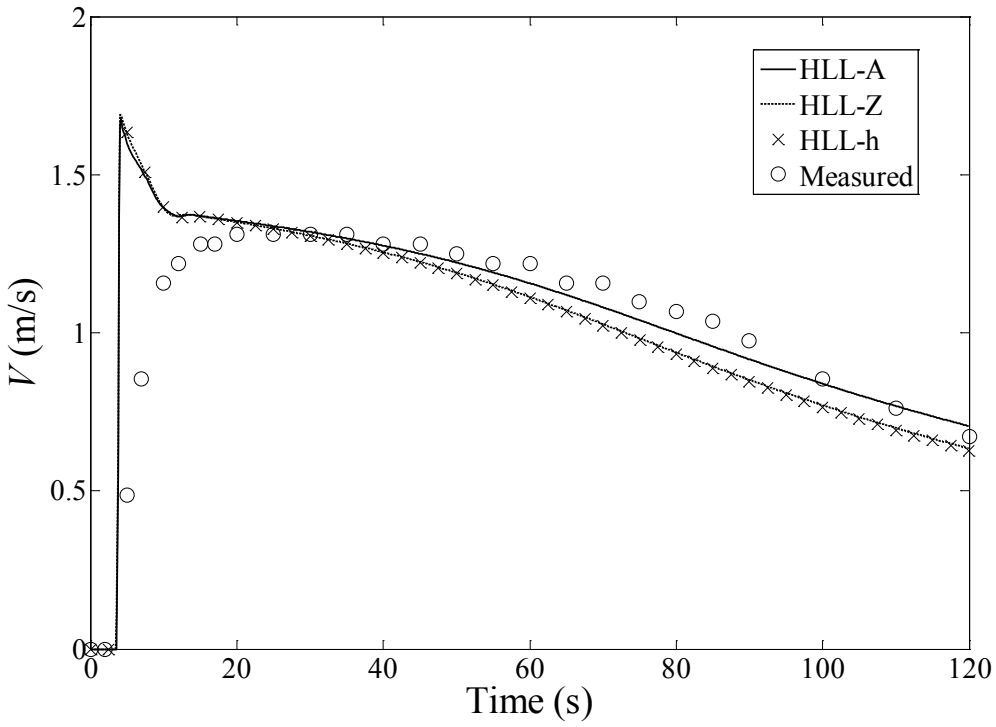

Figure 3.32 Velocity at P2 for WES partial dam-break

3.11 Teton dam failure

The one-dimensional numerical model is applied to model the Teton dam failure that took place on June 5, 1976. The Teton dam was a 92.96 m (305 feet) high earth-fill dam with a 914.4 m (3000 feet) long crest located on the Teton River in southeastern Idaho. The inundated area after the dam-break is shown in Figure 3.33. River cross-sections, Manning's roughness coefficient, reservoir storage depletion, and the flow rate at the dam site were documented by the U.S. Geological Survey (Ray and Kjelstrom, 1978). The flooded area and measured cross-sections, shown as straight lines across the river, are shown in Figure 3.33. The cross-sections used in the computation are interpolated from the available data. Results using different mesh sizes showed that the

effects of the mesh size on accuracy are minimal. This may be because of the relatively long simulation period and linearly interpolation of the cross-section from survey data. The discharge at the dam site is shown in Figure 3.34. The dam site discharge and water surface level are used as inflow boundary conditions, corresponding to the supercritical inflow condition. Since the initial flow conditions before the dam-break were not specified, a downstream dry bed is assumed as an initial condition for simulation. In addition, inflows from Henry's Fork and Snake River are ignored as these inflows are small compared to the large flood event. The simulation ended at 10 hours after the dam-break.

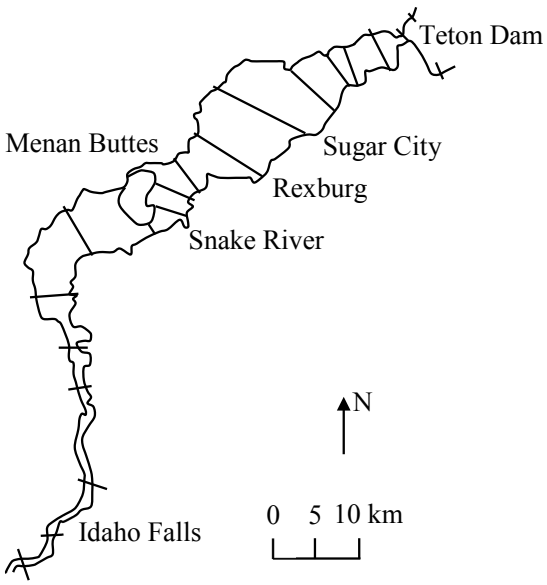

Figure 3.33 Flood area downstream of Teton River

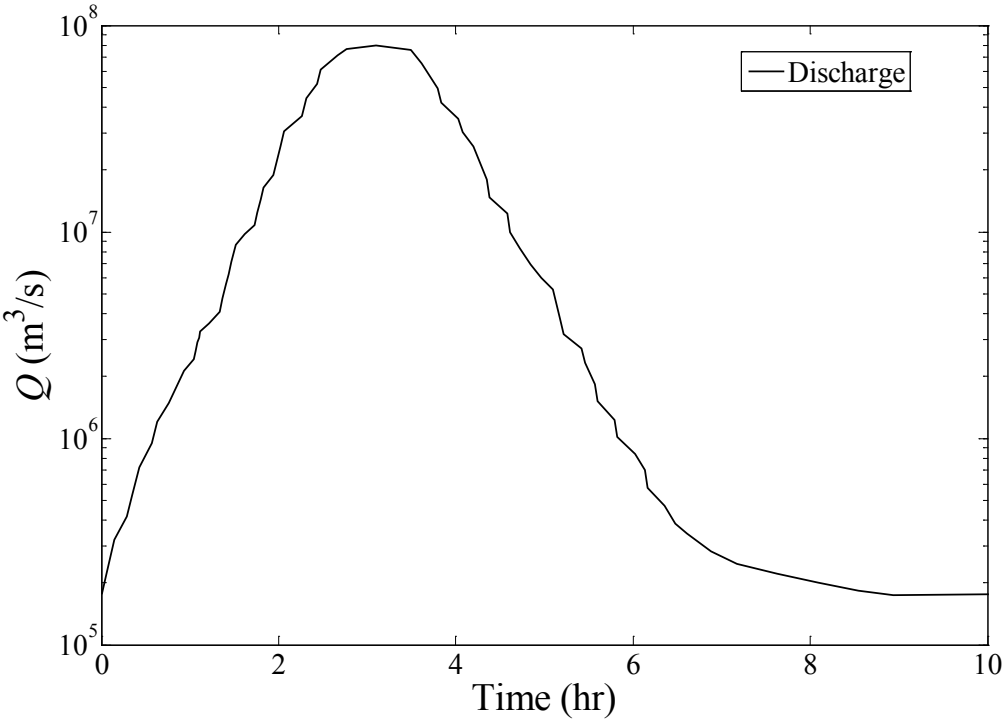

Figure 3.34 Discharge at the dam site after dam-break

Figure 3.35 and Figure 3.36 show the computed water surface and Froude number at 10 hours after the dam-break. Figure 3.37 shows the maximum water surface during the flood event along the river. As shown in Figure 3.35, the water surface exhibits large variation in the study reach. In Figure 3.37, the computed maximum water surface elevation along the river reach compares well with the measured data. The difference between the computed result and the measured data in the middle of the river (30-50 km) is mainly due to omission of the side flow from the Snake River. The results demonstrate that the numerical scheme is capable of modeling dam-break problems in natural rivers and can provide satisfactory results.

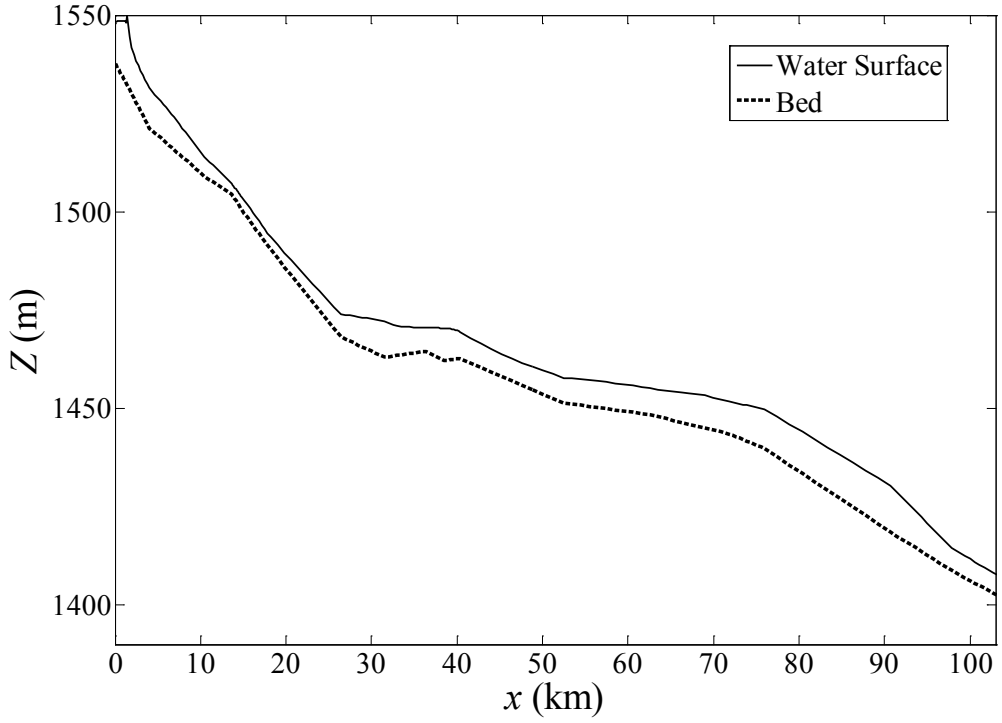

Figure 3.35 Water surface along the river at time=10 hour after dam-break

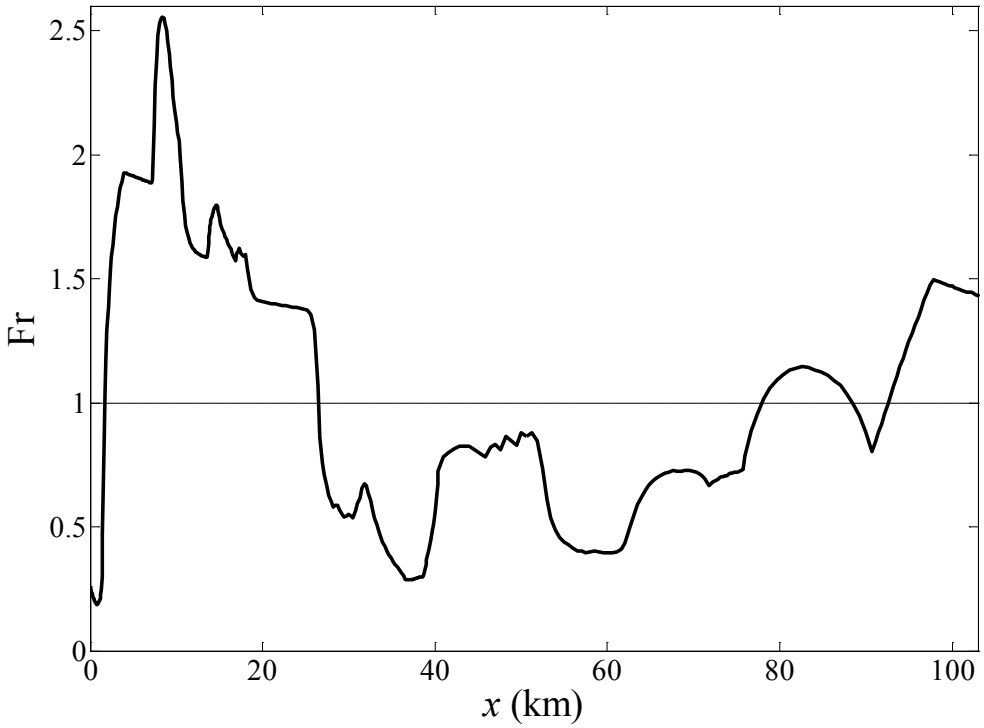

Figure 3.36 Froude number along the river at time=10 hour after dam-break

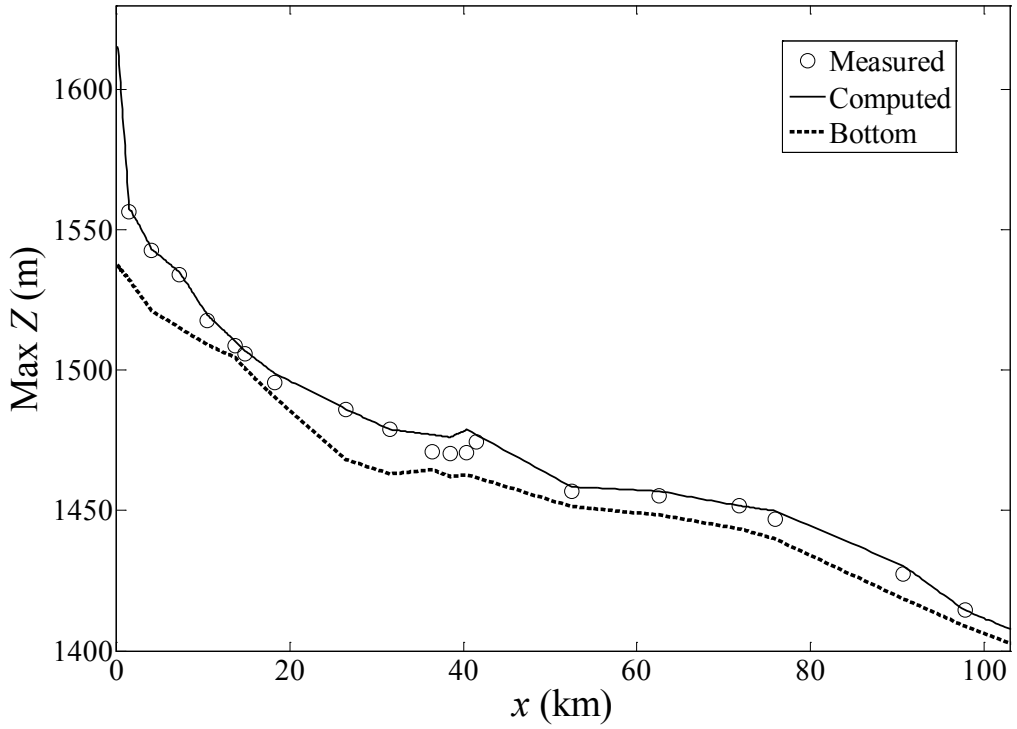

Figure 3.37 Maximum water elevations during the flood event

3.12 Toce River case

A physical model at a 1:100 scale of a reach of the Toce River valley (Northern Alps, Italy) was developed at the ENEL-HYDRO laboratory in Milan, Italy. The physical model tests were used in the CADAM project (Soares Frazão and Testa, 1999). Modeling parameters, such as topographic data, inflow hydrograph, and Manning's coefficient, were specified by Electricité de France (EDF). Results of the physical model tests were also provided so that modelers could make an objective comparison of their numerical modeling results.

The topography of Toce River physical model is shown in 3.38, covering an area of approximate 50 m × 12 m. To measure the water surface level, 32 water level gauges

were installed in the physical model. Selected gauges along the main river axis (P1, P5, P18, P21, and P26) are used to compare the simulated results. For simulation, 62 cross-sections are used (Figure 3.39). The elements used in the computation are of non-uniform size and their lengths vary from 0.25 m to 1.94 m.

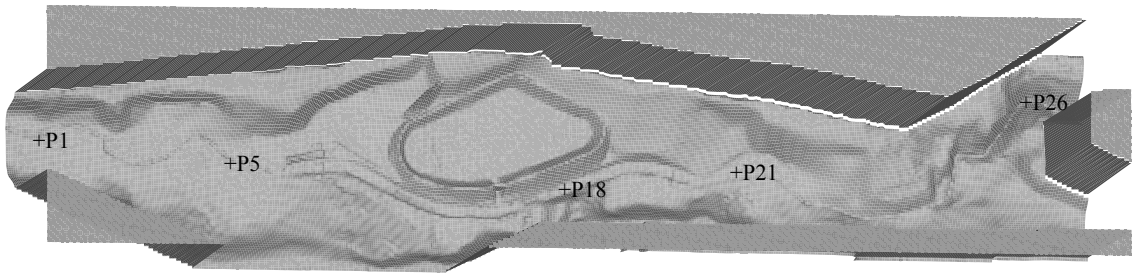

Figure 3.38 Plan view of Toce River topography

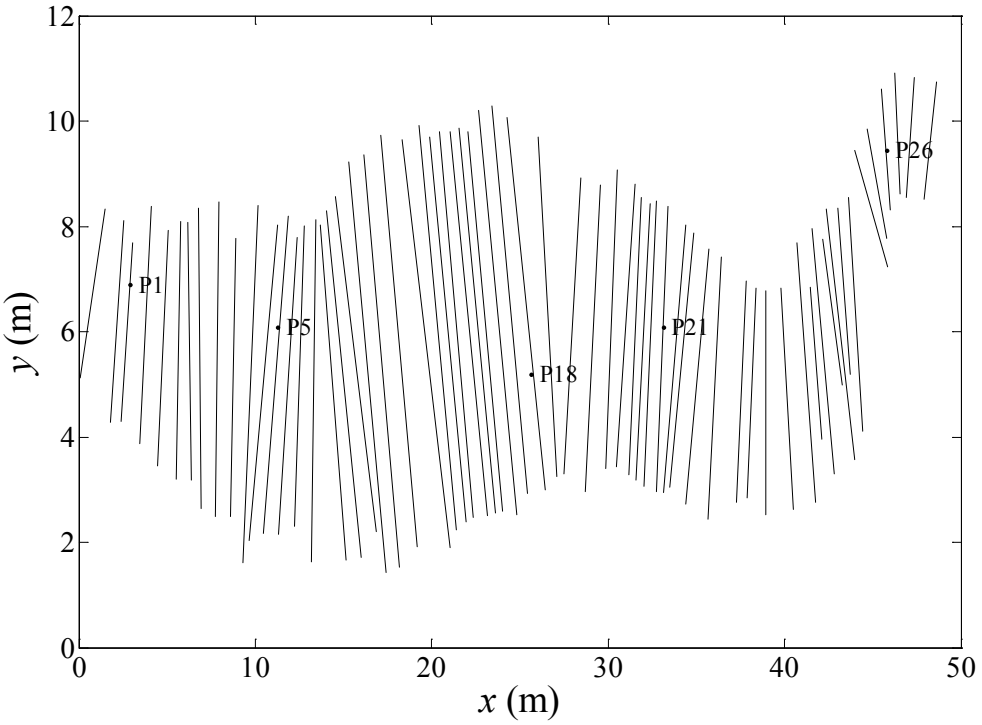

Figure 3.39 Location of computational cross-section of Toce River

A rectangular tank was located at the upstream (left) end of the physical model. The inflow hydrograph at the rectangular tank is shown in Figure 3.40 and is used as the inflow boundary condition. The flow conditions at the inlet and outlet ends of the physical model were forced to be critical and the same conditions are applied in the computation. The channel downstream of the tank was initially dry.

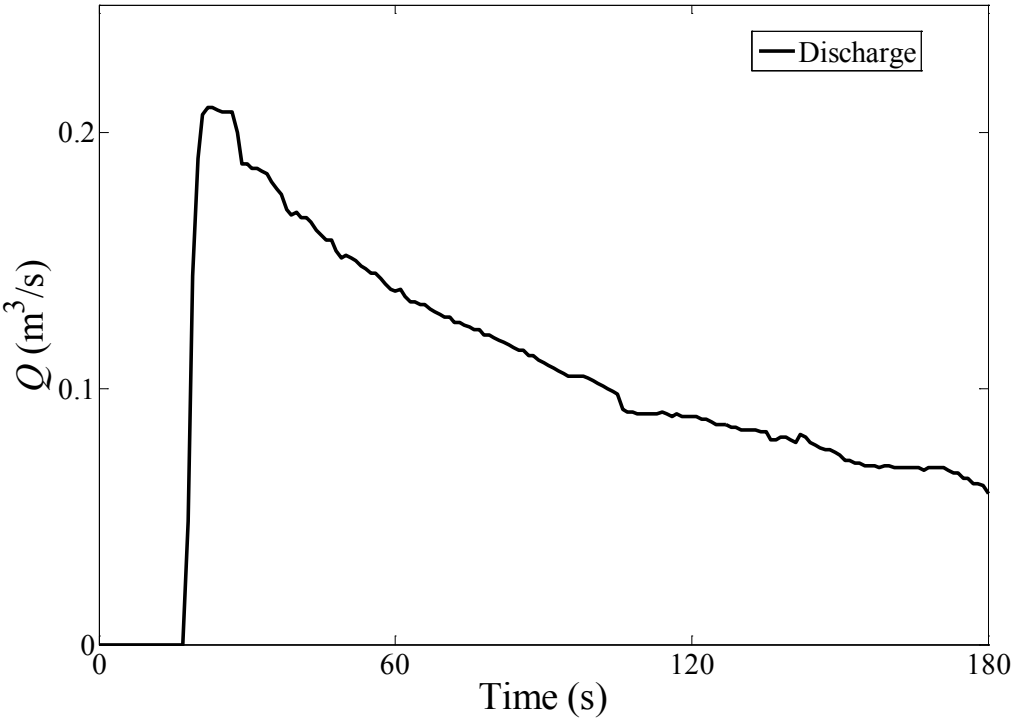

Figure 3.40 Inflow boundary conditions at the river inlet

The value of Manning's roughness coefficient is taken to be 0.0162 s/m$^{1/3}$ based on the value proposed in the physical model study. The numerical simulation is run for 180 seconds. The computed water surface and Froude number at 100 seconds are shown in Figure 3.41 and Figure 3.42. The predicted water surface level, as displayed in Figure

3.41, shows a lot of variation due to bed slope and channel width changes. Several hydraulic jumps can be identified as confirmed by the Froude number variation along the channel shown in Figure 3.42.

The computed results of maximum water level are plotted along with measured data from the physical model study and results from ISIS model in Figure 3.43. The ISIS model was based on the finite difference Preissmann implicit scheme (Rosu and Ahmed, 1999). The computed results of maximum water level, as shown in Figure 3.43, are in good agreement with the physical model measurements. The root-mean-square error (RMSE) is 0.0473 m between ISIS model and measured data, and is 0.0347 m between the present model and measured data. The present model provides better results than the ISIS model at the downstream end of the river.

Figure 3.44 shows a comparison of computed stage hydrographs with the measured data at five gauge points. Besides the coarse mesh in Figure 3.39, a refined mesh with four elements between every cross-section is used to investigate the effect of mesh size. The arrival time of the surge and the variation of the water surface elevation with time show good agreement with the measured data. The refined mesh gives better prediction of the arrival times at P1 and P5, while the coarse mesh performs better at P18, P21 and P26. These two meshes give similar result for water surface at P1 and P5, while the refined mesh performs better at P21 and P26.

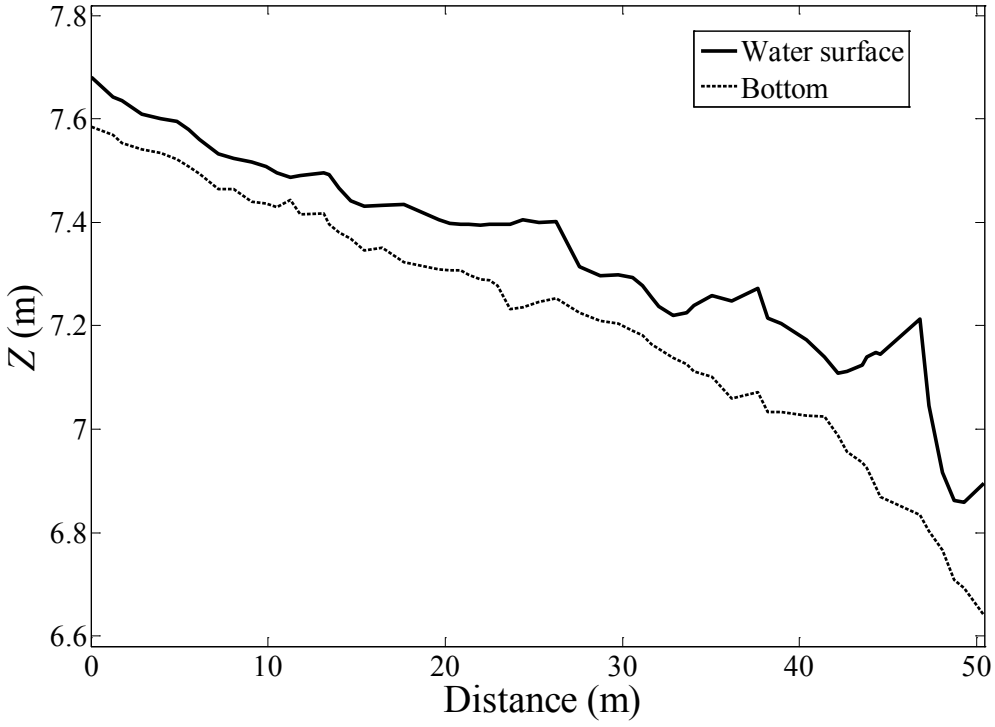

Figure 3.41 Computed water surface profile at time=100 s

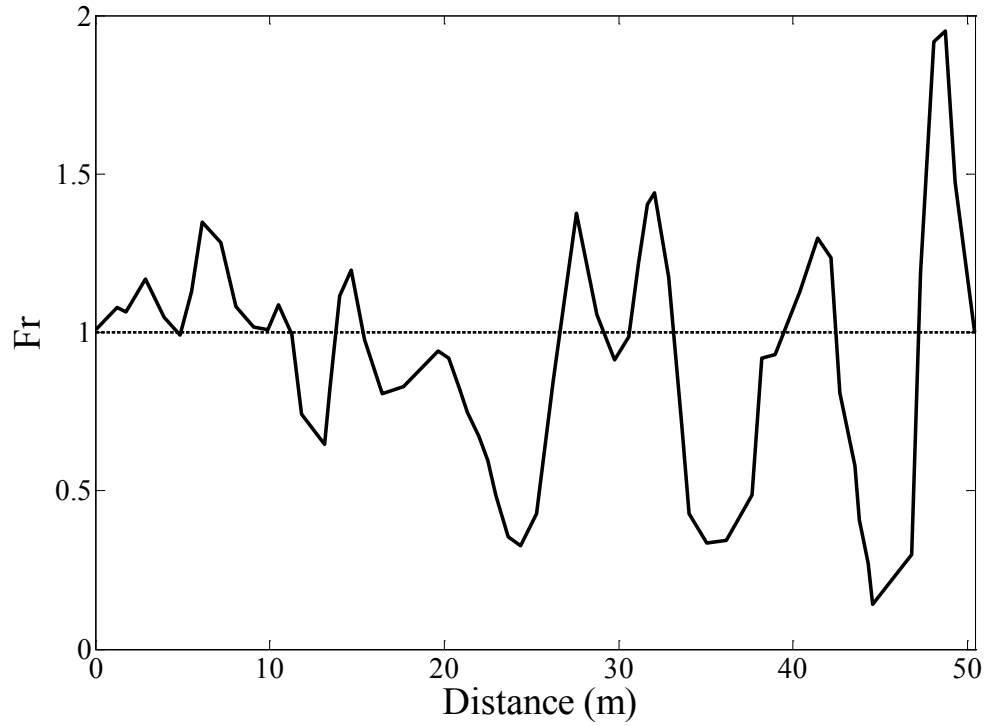

Figure 3.42 Computed Froude number along the river at time=100 s

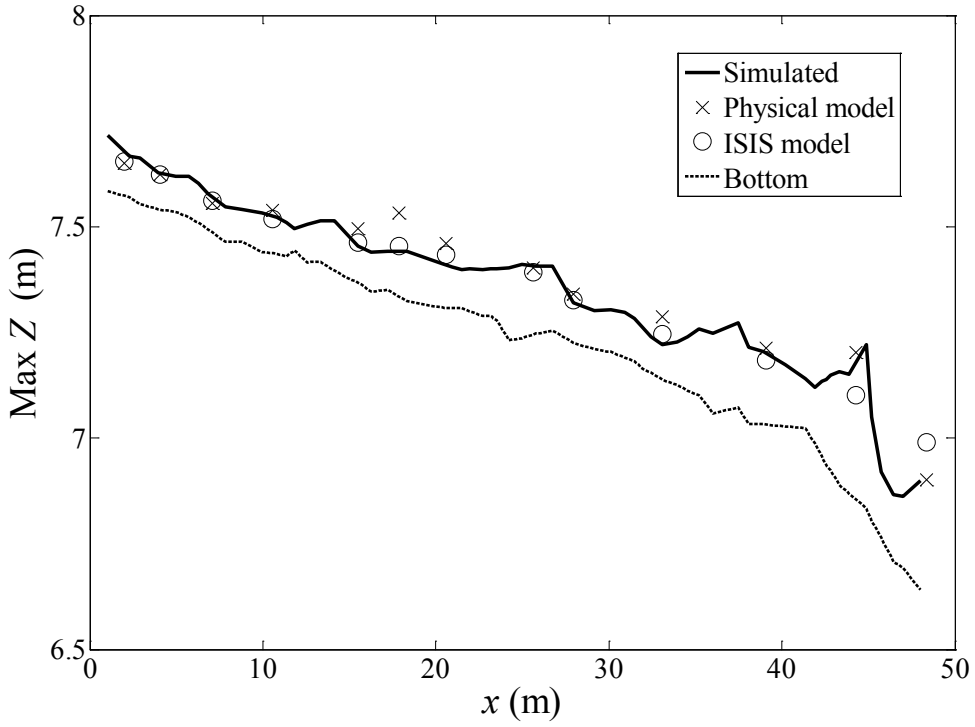

Figure 3.43 Computed maximum water level of Toce River

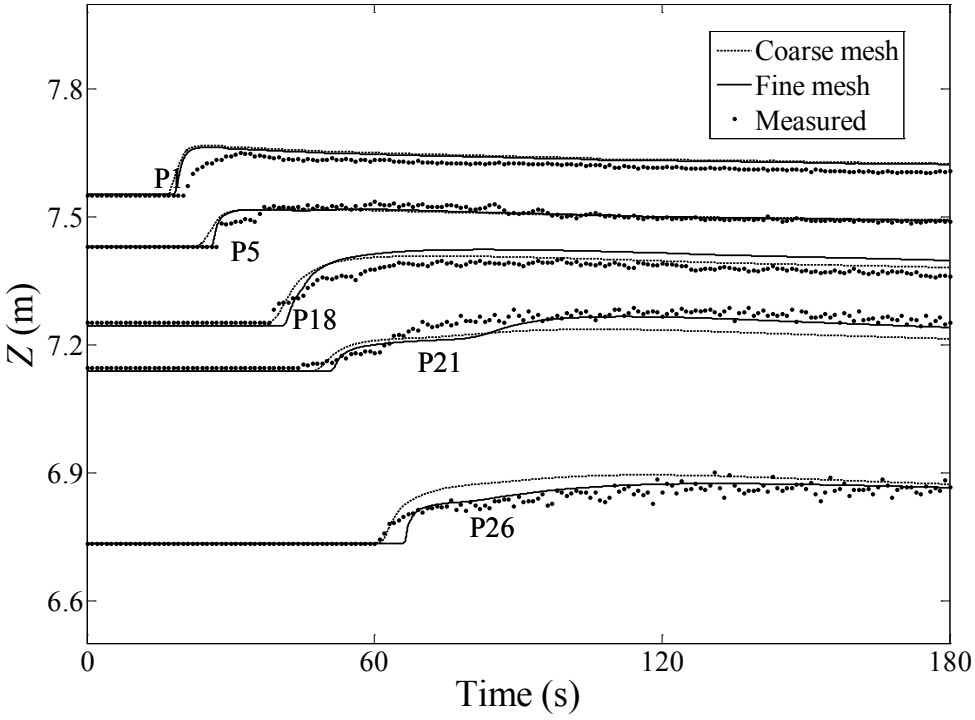

Figure 3.44 Computed and measured stage hydrographs

3.13 East Fork River case

In this test, the numerical scheme is used to model a flood event in the East Fork River, Wyoming. The East Fork River flows in the Wind River Range of Wyoming, west of the Continental Divide and east and southeast of Mt. Bonneville. The study reach configuration is shown in Figure 3.45.

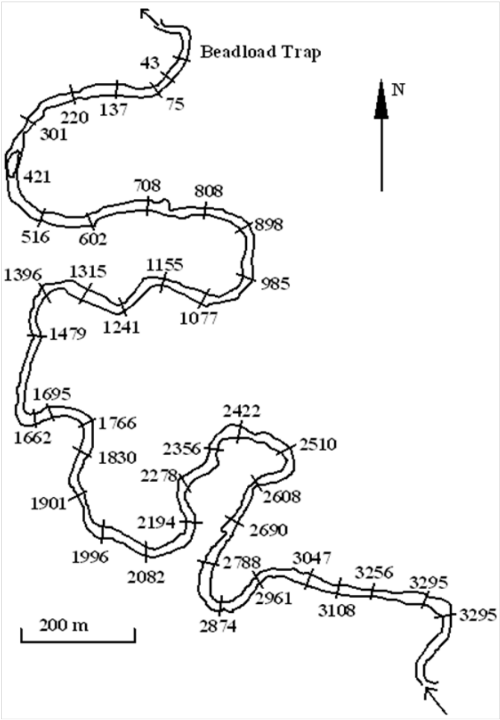

Figure 3.45 Map of the 3.3 km study reach in the East Fork River (Emmett et al., 1980)

The meandering study reach is approximately 3.3 km in length and terminates downstream at a bedload trap constructed across the river. The number shown at each cross-section in the figure is the centerline distance (in meters) upstream from the bedload trap (section 0000). Bed elevation at 39 cross-sections were measured daily during a month-long period (Meade et al., 1980). Simulations performed with different

mesh sizes showed that the results were independent of mesh size. The influence of the sediment transport and changes of channel bed (due to short simulation period) are not considered in this test.

The simulation period of the river flow is 12 days from June 1 to June 12, 1979. The hourly discharge measured at section 3295 is used as the inflow boundary condition (Emmett et al., 1980), while the hourly gage height at section 0000 is used as outflow boundary condition. Subcritical flow condition existed at the inflow and outflow boundary and the boundary conditions used in the model reflect that fact. The average water depth on June 1 is used as initial depth, while the initial flow rate is set to 6.0 m^3/s throughout the study reach. Since the value of the roughness coefficient is unavailable, the dependency of numerical results on roughness coefficient is investigated.

The computed and measured water surface at sections 2505 and section 3295 are shown in Figure 3.46, while the discharges at section 0000 are shown in Figure 3.47. In Figure 3.48, the computed water surface at noon on June 12, 1979 is compared with the measured water surface. Results show that a constant Manning's roughness coefficient of 0.028 $s/m^{1/3}$ gives the best results that are in agreement with measured data, increase of roughness would increase water surface and vice versa. For the case of $n = 0.028$, the difference in the measured and computed values at the beginning is mostly due to the uncertainty in the initial conditions, the difference during the last four days may originate from the sediment transport within the reach. In general, the numerical results with $n = 0.028$ are in good agreement with the measured data and the test demonstrates that the model is capable of simulating flood flows in natural rivers.

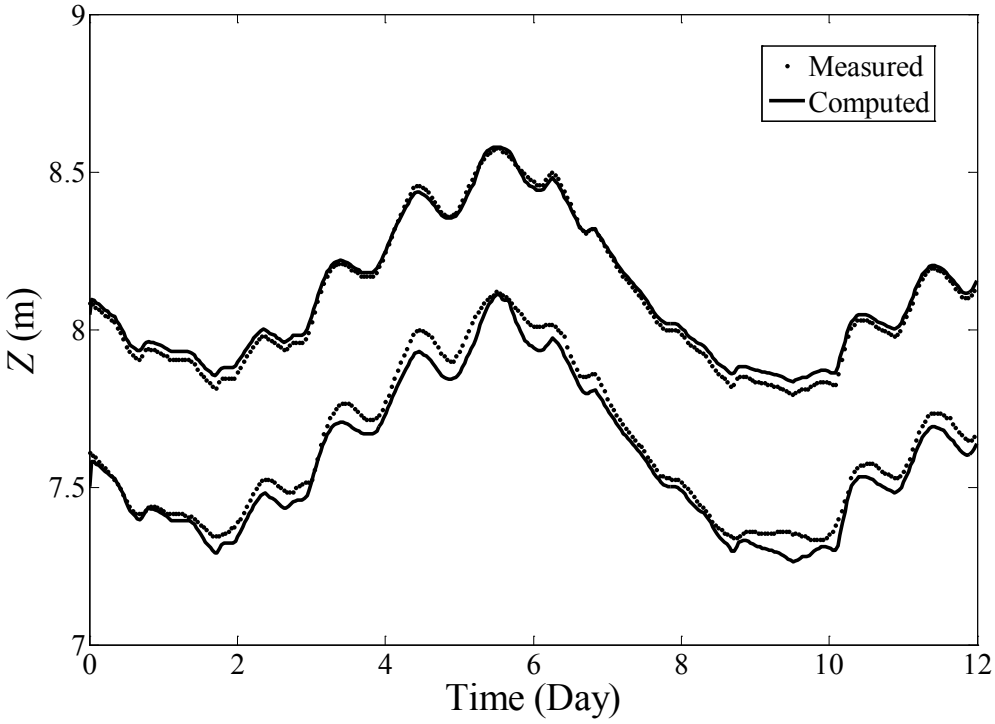

Figure 3.46 Water surface at section 3295 and section 2505 (lower line)

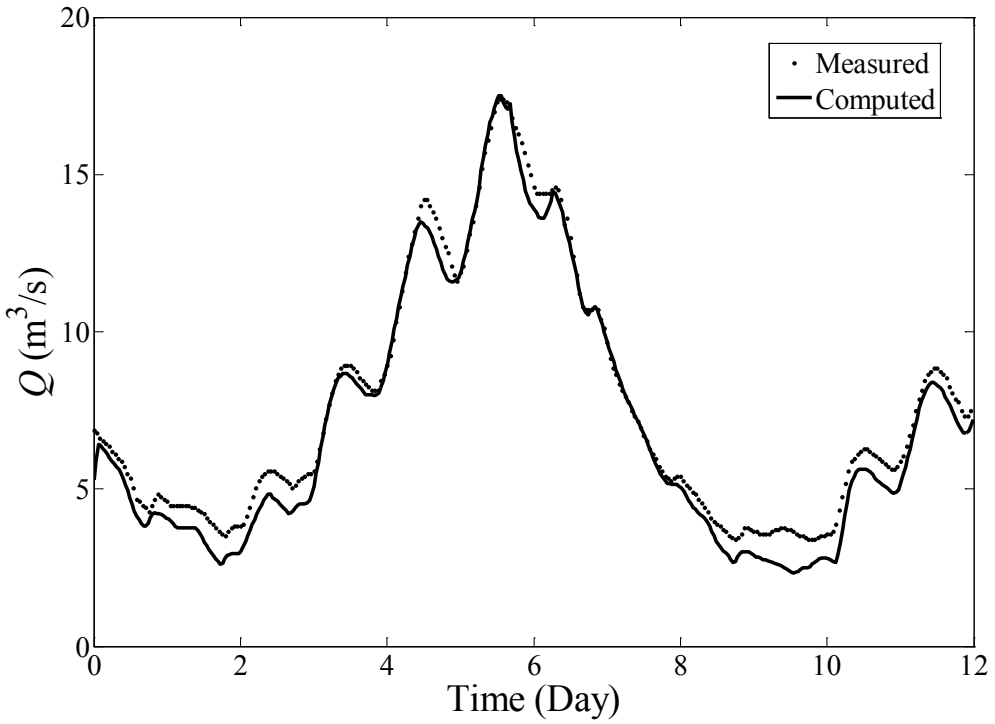

Figure 3.47 Computed and measured discharge at section 0000

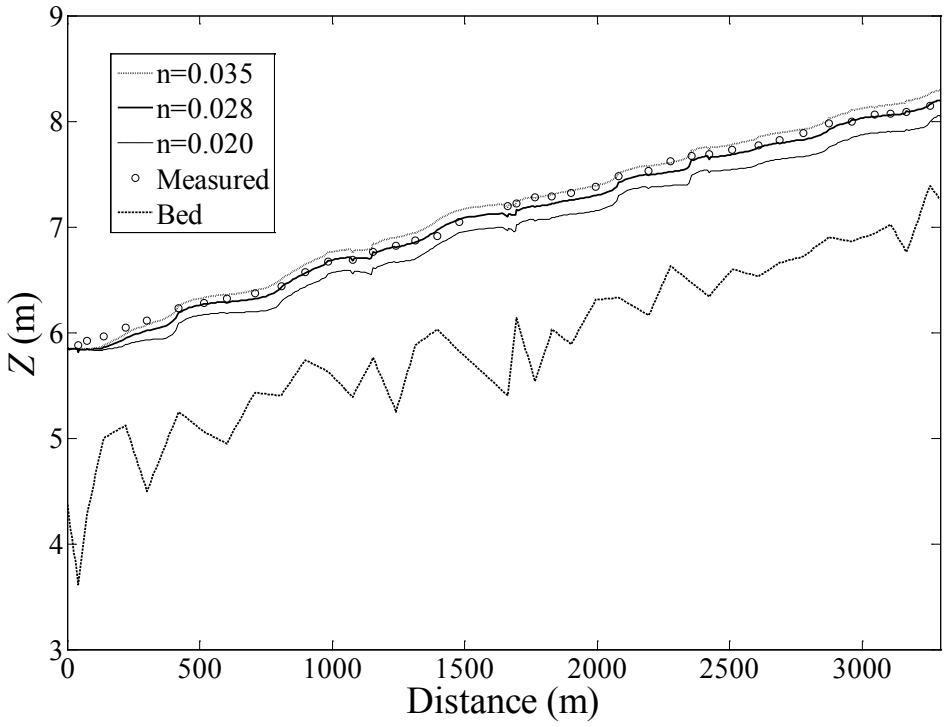

Figure 3.48 Computed and measured water surface around noon June 12, 1979

CHAPTER FOUR

NUMERICAL SCHEME FOR TWO-DIMENSIONAL FLOWS

In this chapter, the two-dimensional shallow water equations are presented. Details of the numerical scheme to model the two-dimensional shallow water equations with discontinuous Galerkin finite element method are provided. The treatment of numerical flux and slope limiters used in the study is presented. The wetting and drying procedure is also outlined.

4.1 Governing equations

The two-dimensional shallow water equations are derived by integrating the Navier-Stokes equations along the depth of the fluid body. Several assumptions are made such as hydrostatic pressure distribution and uniform velocity profile in the vertical direction. The advantage is that free surface location is determined as part of the solution. The two-dimensional shallow water flow equations can be applied in situations where vertical acceleration may be neglected and the horizontal extent is much greater than the depth of flow (Li and Liu, 2001; Lai, 2010).

The widely used form of the depth-averaged, two-dimensional, shallow water flow equations can be written as

$$\frac{\partial \mathbf{U}}{\partial t} + \frac{\partial \mathbf{E}(\mathbf{U})}{\partial x} + \frac{\partial \mathbf{G}(\mathbf{U})}{\partial y} = \mathbf{S} \tag{4.1}$$

where the vectors of conserved variables **U**, fluxes (**E**, **G**) in the x and y directions, and the sources term **S** can be written, respectively, as follows

$$\mathbf{U} = \begin{pmatrix} h \\ hu \\ hv \end{pmatrix}; \qquad \mathbf{S} = \begin{pmatrix} 0 \\ -gh\dfrac{\partial z_b}{\partial x} - g\dfrac{n^2 u\sqrt{u^2+v^2}}{h^{7/3}} \\ -gh\dfrac{\partial z_b}{\partial y} - g\dfrac{n^2 v\sqrt{u^2+v^2}}{h^{7/3}} \end{pmatrix} \tag{4.2}$$

$$\mathbf{E}(\mathbf{U}) = \begin{pmatrix} hu \\ hu^2 + gh^2/2 \\ huv \end{pmatrix}; \quad \mathbf{G}(\mathbf{U}) = \begin{pmatrix} hv \\ huv \\ hv^2 + gh^2/2 \end{pmatrix}$$

where $h =$ water depth, $z_b =$ bottom elevation, u and v are the velocity components in the x and y directions, respectively, $g =$ gravitational acceleration, and $n =$ Manning's roughness coefficient.

The eigenvalues and eigenvectors for the shallow water equations are given, respectively, by Equations (4.3) and (4.4).

$$\lambda_1 = un_x + vn_y - \sqrt{gh}; \;\; \lambda_2 = un_x + vn_y; \;\; \lambda_3 = un_x + vn_y + \sqrt{gh} \tag{4.3}$$

$$\mathbf{k}_1 = \begin{pmatrix} 1 \\ u - \sqrt{gh}n_x \\ v - \sqrt{gh}n_y \end{pmatrix}; \; \mathbf{k}_2 = \begin{pmatrix} 1 \\ -\sqrt{gh}n_y \\ \sqrt{gh}n_x \end{pmatrix}; \; \mathbf{k}_3 = \begin{pmatrix} 1 \\ u + \sqrt{gh}n_x \\ v + \sqrt{gh}n_y \end{pmatrix} \tag{4.4}$$

The two-dimensional shallow water equations can also be written in following form

$$\mathbf{U} = \begin{pmatrix} h \\ q_x \\ q_y \end{pmatrix}; \quad \mathbf{S} = \begin{pmatrix} 0 \\ -gh\dfrac{\partial Z}{\partial x} - g\dfrac{n^2 q_x \sqrt{q_x^2 + q_y^2}}{h^{7/3}} \\ -gh\dfrac{\partial Z}{\partial y} - g\dfrac{n^2 q_y \sqrt{q_x^2 + q_y^2}}{h^{7/3}} \end{pmatrix} \tag{4.5}$$

$$\mathbf{E}(\mathbf{U}) = \begin{pmatrix} q_x \\ q_x^2 / h \\ q_x q_y / h \end{pmatrix}; \qquad \mathbf{G}(\mathbf{U}) = \begin{pmatrix} q_y \\ q_x q_y / h \\ q_y^2 / h \end{pmatrix}$$

where $Z =$ water surface level, $q_x = hu$ and $q_y = hv$ are the unit width flow rates in the x and y directions, respectively. In this formulation, the net hydrostatic pressure is included in the source term. The numerical treatment of this new source that accounts for an accurate estimate of numerical flux needs to be provided. The advantage of this form is that it eliminates unphysical bed slope generate flow as in one-dimensional case. Similar to the one-dimensional case, since the physical characteristics of the equations are independent of the mathematical form of the equations, the actual eigenvalues and eigenvectors based on Equation (4.2) should be used for the approximate Riemann solver.

4.2 Formulation of Discontinuous Galerkin method

Eq. (4.1) can be written in a vector form as

$$\frac{\partial \mathbf{U}}{\partial t} + \nabla \bullet \mathbf{F} = \frac{\partial \mathbf{U}}{\partial t} + \frac{\partial \mathbf{E}}{\partial x} + \frac{\partial \mathbf{G}}{\partial y} = \mathbf{S} \tag{4.6}$$

where $\mathbf{F} = (\mathbf{E}, \mathbf{G})$. A typical layout of non-overlapping triangular elements in the DG method is shown in Figure 4.1. The main element (0) for which the computations are

performed and the three surrounding elements (1, 2, and 3) are shown in the figure. The number of vertices at a node depends on the number of elements sharing that node.

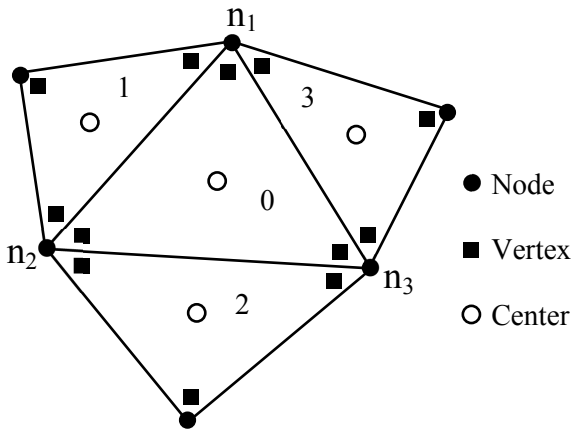

Figure 4.1 Formulation of triangular elements in DG method

The discontinuous Galerkin formulation is written for each element. The variation of any variable with an element is represented by the values of the variable at vertices and shape or interpolating functions. The modified variables and any function of these variables can be written as

$$\hat{\mathbf{U}} = \mathbf{N}_j \mathbf{U}_j; \ \hat{\mathbf{F}} = \mathbf{F}(\hat{\mathbf{U}}); \ \hat{\mathbf{S}} = \mathbf{S}(\hat{\mathbf{U}}) \tag{4.7}$$

where $\mathbf{N}_j$ is a diagonal matrix of basis or interpolating functions, $\mathbf{U}_j$ are the approximations of the conserved variables at vertices, and the summation notation is assumed. Equation (4.6) is then multiplied by the weight functions, $\mathbf{N}_i$, taken to be the same as the shape functions, $\mathbf{N}_j$, for the Galerkin method. The flux term is integrated by parts and the resulting equation can be written as

$$\int_{\Omega_e} \mathbf{N}_i \frac{\partial \hat{\mathbf{U}}}{\partial t} d\Omega + \int_{\Gamma_e} \mathbf{N}_i (\hat{\mathbf{F}} \bullet \mathbf{n}) d\Gamma - \int_{\Omega_e} \nabla \mathbf{N}_i \bullet \hat{\mathbf{F}} \, d\Omega = \int_{\Omega_e} \mathbf{N}_i \hat{\mathbf{S}} \, d\Omega \tag{4.8}$$

where $\hat{\mathbf{F}} \bullet \mathbf{n}$ is the numerical intercell flux, $\mathbf{n}$ is an outward unit normal vector at an element's boundary, Ω_e represents element area, and Γ_e is the perimeter of the element. Since discontinuous elements are connected by numerical flux across the boundaries of elements, it is crucial to calculate the numerical flux accurately in the DG method.

4.3 Numerical flux and dry bed treatment

The numerical flux in Equation (4.8) can be evaluated using upwind numerical flux functions. Since discontinuous elements are dealt with in the discontinuous Galerkin method, a generalized local Riemann problem can be solved for the numerical flux. The two-dimensional shallow water flow equations is a three-wave system, numerical results show that the HLLC flux is more accurate than the HLL and Roe flux (Erduran et al., 2002). The HLLC flux for two-dimensional shallow water equations are given below. Introducing the rotation matrix and its inverse as follows

$$\mathbf{T} = \begin{bmatrix} 1 & 0 & 0 \\ 0 & n_x & n_y \\ 0 & -n_y & n_x \end{bmatrix}; \ \mathbf{T}^{-1} = \begin{bmatrix} 1 & 0 & 0 \\ 0 & n_x & -n_y \\ 0 & n_y & n_x \end{bmatrix} \tag{4.9}$$

where n_x and n_y are the components of the unit normal vector in the x and y directions, respectively. The rotational invariance of the flux yields

$$\mathbf{F} \bullet \mathbf{n} = \mathbf{E} n_x + \mathbf{G} n_y = \mathbf{T}^{-1} \mathbf{E}(\mathbf{T}\mathbf{U}) \tag{4.10}$$

and defining $\mathbf{Q} = \mathbf{TU}$, the numerical flux $\hat{\mathbf{F}} \bullet \mathbf{n}$ can be obtained through the evaluation of numerical flux $\hat{\mathbf{E}}$ by using Equation (4.11) given below

$$\hat{\mathbf{F}} \bullet \mathbf{n} = \mathbf{T}^{-1} \hat{\mathbf{E}}(\mathbf{Q}) \tag{4.11}$$

where $\hat{\mathbf{E}}(\mathbf{Q})$ follows the same functional relationship between $\hat{\mathbf{E}}$ and $\mathbf{Q}$ as that between $\hat{\mathbf{E}}(\mathbf{U})$ and $\mathbf{U}$. The HLLC flux is based on the assumption of a three-wave system, as illustrated in Figure 4.2, which is the case for the two-dimensional shallow water flow equations.

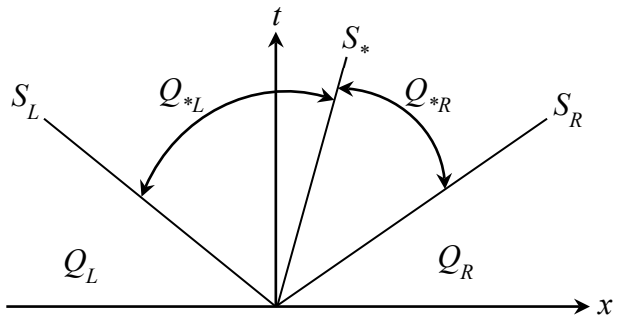

Figure 4.2 Structure of a three-wave HLLC solver

The numerical flux, $\hat{\mathbf{E}}$, computed from HLLC flux function is given by (Toro et al., 1994; Eskilsson and Sherwin, 2004)

$$\hat{\mathbf{E}}(\mathbf{Q}) = \begin{cases} \mathbf{E}(\mathbf{Q}_L) & \text{if } S_L \geq 0 \\ \mathbf{E}(\mathbf{Q}_L) + S_L(\mathbf{Q}_{*L} - \mathbf{Q}_L) & \text{if } S_L < 0 \leq S_* \\ \mathbf{E}(\mathbf{Q}_R) + S_R(\mathbf{Q}_{*R} - \mathbf{Q}_R) & \text{if } S_* < 0 < S_R \\ \mathbf{E}(\mathbf{Q}_R) & \text{if } S_R \leq 0 \end{cases} \tag{4.12}$$

where subscripts L and R stand for the left- and right-hand side of the element boundary, respectively. Moving in counterclockwise direction along the element boundary, the left-hand side always refers to the boundary of the element under consideration and the right-hand side indicates the boundary of the adjacent element. To determine the wave speed, the average velocities along the left and right boundaries under consideration are determined. The normal and tangential components of these velocities are determined and denoted as u_n and u_t, respectively. The wave speeds and rotated conserved variables in the star region can then be estimated as

$$S_L = \min\left(u_{nL} - \sqrt{gh_L},\quad u_n^* - \sqrt{gh^*}\right) \tag{4.13}$$

$$S_R = \max\left(u_{nR} + \sqrt{gh_R},\quad u_n^* + \sqrt{gh^*}\right) \tag{4.14}$$

$$u_n^* = \frac{1}{2}\left(u_{nL} + u_{nR}\right) + \sqrt{gh_L} - \sqrt{gh_R} \tag{4.15}$$

$$\sqrt{gh^*} = \frac{1}{2}\left(\sqrt{gh_L} + \sqrt{gh_R}\right) + \frac{1}{4}\left(u_{nL} - u_{nR}\right) \tag{4.16}$$

$$S_* = \frac{S_L h_R\left(u_{nR} - S_R\right) - S_R h_L\left(u_{nL} - S_L\right)}{h_R\left(u_{nR} - S_R\right) - h_L\left(u_{nL} - S_L\right)} \tag{4.17}$$

$$\mathbf{Q}_{*(L,R)} = h_{(L,R)}\left(\frac{S_{(L,R)} - u_{n(L,R)}}{S_{(L,R)} - S_*}\right)\begin{bmatrix} 1 \\ S_* \\ u_{t(L,R)} \end{bmatrix} \tag{4.18}$$

For dry bed problems, the numerical flux is evaluated through a two-wave HLL flux function given below

$$\hat{\mathbf{E}}(\mathbf{Q}) = \begin{cases} \mathbf{E}(\mathbf{Q}_L) & \text{if } 0 \le S_L \\ \dfrac{S_R\mathbf{E}(\mathbf{Q}_L) - S_L\mathbf{E}(\mathbf{Q}_R) + S_L S_R(\mathbf{Q}_R - \mathbf{Q}_L)}{S_R - S_L} & \text{if } S_L < 0 < S_R \\ \mathbf{E}(\mathbf{Q}_R) & \text{if } 0 \ge S_R \end{cases} \tag{4.19}$$

where the wave speed for right-hand dry bed and left-hand dry bed boundaries are given, respectively, as

$$S_L = u_{nL} - \sqrt{gh_L}\,; \quad S_R = u_{nL} + 2\sqrt{gh_L} \tag{4.20}$$

$$S_L = u_{nR} - 2\sqrt{gh_R}\,; \quad S_R = u_{nR} + \sqrt{gh_R} \tag{4.21}$$

Dry bed treatment similar to one-dimensional case is adopted here, a small depth is defined at dry node or a small depth criterion to track wet/dry front with zero depth at dry node. Numerical tests show that for horizontal beds or channel bed with small variation, these two dry bed treatments provide similar results. However, for large variations in bed geometry, the dry bed treatment with zero depth and small depth to track wet/dry front give more accurate results.

4.4 Source term treatment

Using the notation for the elements shown in Figure 4.1, the calculation of the water level slope in the source term can be determined with Green's theorem as given below (Ying et al., 2009)

$$\Omega_0 \frac{\partial Z}{\partial x} = \oint_{\Gamma_0} Z dy = \sum_{k=1}^{3} Z_{0k}\Delta y_k = Z_{01}(y_{n2} - y_{n1}) + Z_{02}(y_{n3} - y_{n2}) + Z_{03}(y_{n1} - y_{n3}) \tag{4.22}$$

$$-\Omega_0 \frac{\partial Z}{\partial y} = \oint_{\Gamma 0} Z dx = \sum_{k=1}^{3} Z_{0k} \Delta x_k = Z_{01}(x_{n2} - x_{n1}) + Z_{02}(x_{n3} - x_{n2}) + Z_{03}(x_{n1} - x_{n3}) \qquad (4.23)$$

where Z_{0k} is the water level at the boundary of elements 0 and k, and Ω_0 is the area of element 0. The water level, Z_{0k}, can be determined using the water surface elevations of elements 0 and k. First, the average water surface elevations at the center of all elements are determined and then the water surface elevations at the boundaries are interpolated using distance weighting. The discretization guarantees that if the water surface in the main element and the surrounding element is the same, then there will be no bed topography generated unphysical flows. Numerical results show that this treatment of source term is accurate.

The well-balanced property in wet domain is satisfied with Equation (4.5). The still water condition with a partially wet domain can be easily achieved by setting the source term **S** to zero in both the partially wet elements and dry elements. In addition, the slope limiter is not applied in elements with zero velocities. Although the source term in partially wet elements is forced to be zero, numerical tests in dam-break flows show that the flood waves are still accurately modeled.

4.5 Slope limiting procedure

It is well established that nonphysical oscillations are produced around discontinuities when higher order numerical schemes are used. Slope limiters are widely used to minimize the oscillations and stabilize numerical schemes. Jawahar and Kamath (2000) developed a six-step van Albada-type slope limiting procedure for finite volume

method. Tu and Aliabadin (2005) modified the slope limiter of Jawahar and Kamath (2000) to establish a five-step slope limiter for compressible flows. In this study, a four-step slope limiter scheme is introduced for the two-dimensional incompressible flows. Tu and Aliabadi (2005) applied the slope limiter on the primitive variables in compressible flows. In this study, the slope limiter is applied on the conserved variables for incompressible flows in order to conserve mass and momentum. So this procedure would be one step less. A concise and consistent way to calculate the element gradient is used here. The limiting procedure includes the following four steps.

Step 1: Compute the average solution of the conserved variable at the element centroid. Arithmetic mean of solutions at each node of an element is taken as the average solution.

$$\overline{U}_0 = \frac{1}{3}\sum_{i=1}^{3} U_{0,i} \tag{4.24}$$

Step 2: Compute the unlimited gradient in each element. Solution in each element is approximated by interpolation functions and vertex solutions.

$$\frac{\partial U}{\partial x} = \sum_{j=1}^{3} \frac{\partial N_j}{\partial x} U_{0,j}; \quad \frac{\partial U}{\partial y} = \sum_{j=1}^{3} \frac{\partial N_j}{\partial y} U_{0,j} \tag{4.25}$$

Step 3: Compute the limited gradient in each element. The limited gradient in an element is computed by taking the weighted average of the unlimited averages surrounding that element.

$$\left(\nabla U\right)_0^l = w_1\left(\nabla U\right)_1 + w_2\left(\nabla U\right)_2 + w_3\left(\nabla U\right)_3 \tag{4.26}$$

where the weighted factors are given as

$$w_1 = \frac{g_2 g_3 + \varepsilon}{g_1^2 + g_2^2 + g_3^2 + 3\varepsilon};\ w_2 = \frac{g_1 g_3 + \varepsilon}{g_1^2 + g_2^2 + g_3^2 + 3\varepsilon};\ w_3 = \frac{g_1 g_2 + \varepsilon}{g_1^2 + g_2^2 + g_3^2 + 3\varepsilon} \tag{4.27}$$

where ε is a small number introduced to prevent indeterminacy and

$$g_1 = \left\|(\nabla U)_1\right\|^2;\ g_2 = \left\|(\nabla U)_2\right\|^2;\ g_3 = \left\|(\nabla U)_3\right\|^2 \tag{4.28}$$

which are the square of the L_2 norm of the unlimited element gradients.

Step 4: Compute the limited conservative variables at vertices of each element. The requirements for the reconstructed solution to satisfy each component of limited gradient and preserve the average at the element centroid result in the following

$$\begin{cases} \left(\dfrac{\partial U}{\partial x}\right)_0^l = \displaystyle\sum_{j=1}^{3} \frac{\partial N_j}{\partial x} U_{0,j}^l \\ \left(\dfrac{\partial U}{\partial y}\right)_0^l = \displaystyle\sum_{j=1}^{3} \frac{\partial N_j}{\partial y} U_{0,j}^l \\ \overline{U}_0 = \dfrac{1}{3}\displaystyle\sum_{j=1}^{3} U_{0,j}^l \end{cases} \tag{4.29}$$

Equation (4.29) is solved to obtain the limited variable $U_{0,j}^l$ at each node in an element.

This slope limiter is also compared with the 2D Superbee slope limiter (Anastasiou and Chan, 1997). Numerical tests show this slope limiter is more accurate than or at least similar to the Superbee limiter.

4.6 Time integration

Previous studies (Cockburn and Shu, 1989; Cockburn et al., 1989; Cockburn et al., 1990) have shown that to conserve the TVD property, the Runge-Kutta time integration scheme should be one order higher than the spatial discretization. Since linear

interpolation or basis functions are used in this study, the second order two-stage TVD Runge-Kutta scheme is employed. Equation (4.8) can be written in the following form after numerical integration

$$\frac{\partial \mathbf{U}}{\partial t} = L(\mathbf{U}) \tag{4.30}$$

To advance the solution from time step n to n+1, the second order TVD Runge-Kutta scheme, as given by Gottlieb and Shu (1998), can be written as

$$\begin{cases} \mathbf{U}^{[1]} = \mathbf{U}^n + \Delta t L\left(\mathbf{U}^n\right) \\ \mathbf{U}^{n+1} = \frac{1}{2}\mathbf{U}^n + \frac{1}{2}\mathbf{U}^{[1]} + \frac{\Delta t}{2} L\left(\mathbf{U}^{[1]}\right) \end{cases} \tag{4.31}$$

and the time step, Δt, is restricted by the Courant-Friedrichs-Levy conditions, C, (Fagherazzi et al., 2004) as follows

$$\Delta t < C\left(\frac{L_{min}}{\max\left(\sqrt{u^2+v^2}+\sqrt{gh}\right)\max\left(1, p^2\right)} \right) \tag{4.32}$$

where L_{min} is the length of the smallest edge of the element and p is the order of the basis function. Based on the one-dimensional model, the value of C is restricted to 0.33 in this study.

CHAPTER FIVE

NUMERICAL TESTS FOR TWO-DIMENSIONAL FLOWS

In this chapter, the two-dimensional numerical model with DG method is validated through a number of numerical tests, including an oblique hydraulic jump, shock wave in channel contraction, wetting and drying in a parabolic bowl, circular dam-break, partial dam-break, flows in bends, and flows in natural rivers. Numerical results are also compared with analytical solutions or field measurements, if available.

5.1 Oblique hydraulic jump

The numerical scheme is first tested by simulating an oblique hydraulic jump in a horizontal, frictionless channel for which an exact solution is available. Researchers often used this test to examine the numerical schemes for the shallow water equations (Ying et al, 2009; Yoon and Kang, 2004; Anastasiou and Chan, 1997; Alcrudo and Garcia-Navarro, 1993). The plan view of the channel and the mesh used (with 5112 elements) are shown in Figure 5.1. An oblique hydraulic jump forms inside the channel when a supercritical flow is deflected by a converging wall. Water depth and velocities in the x and y directions at the inflow boundary are set to be 1.0 m, 8.57 m/s, and 0 m/s, respectively.

Figure 5.2 shows the computed water surface and Figure 5.3 shows the computed depth contours at steady state. The average water depth behind the jump is 1.51 m. The angle between the shock front of the hydraulic jump and x coordinate is 30°. These

results are in good agreement with the analytic solution of 1.5049 m depth and 30° angle (Alcrudo and Garcia-Navarro, 1993). The simulated and exact solutions of the water depth along the solid line (shown in Figure 5.1) are shown in Figure 5.4. The Superbee limiter provides results that are similar to the slope limiter proposed in Equations (4.24) – (4.29). Numerical results show that the scheme is capable of capturing the oblique shock in converging supercritical flow.

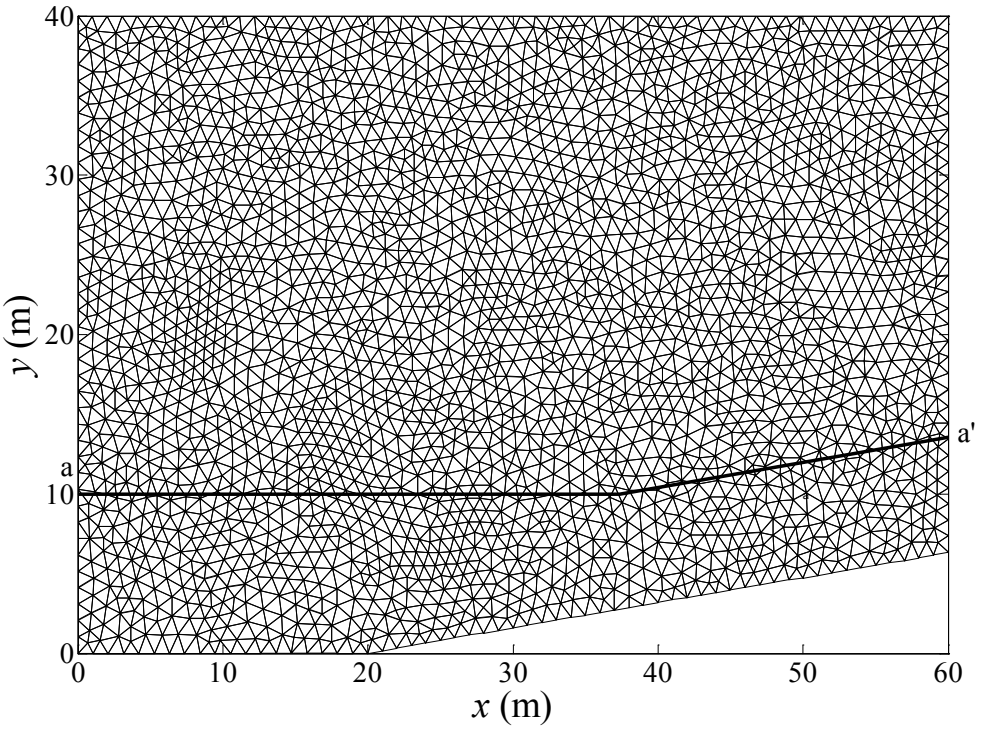

Figure 5.1 Computational domain and grid for the oblique hydraulic jump test

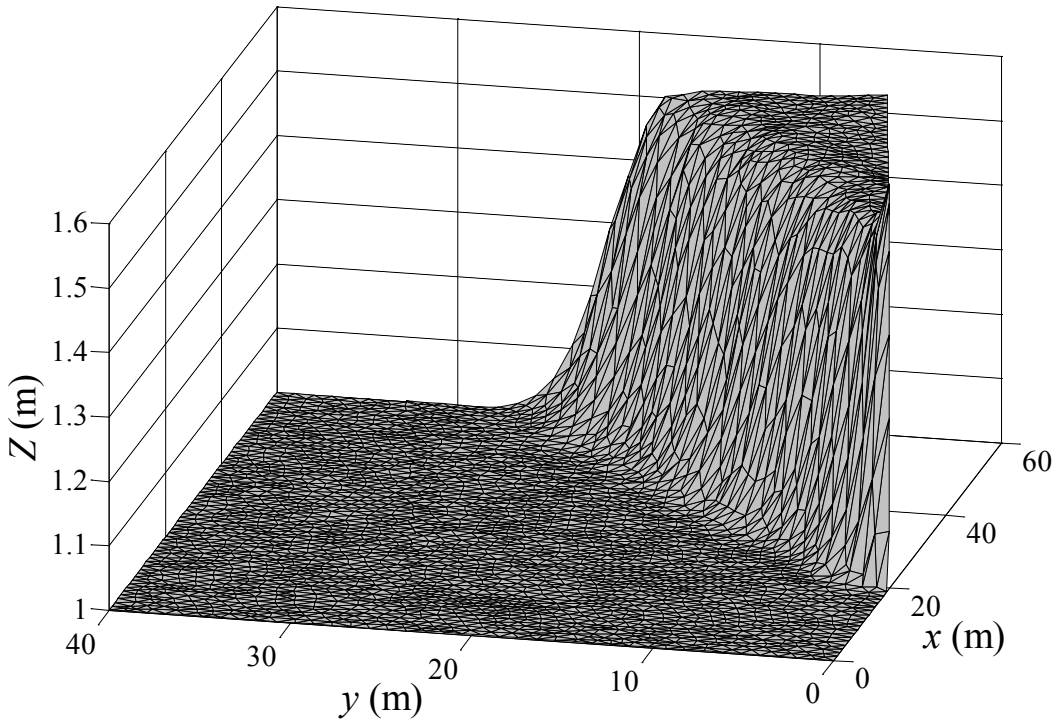

Figure 5.2 Computed water surface for the oblique hydraulic jump test

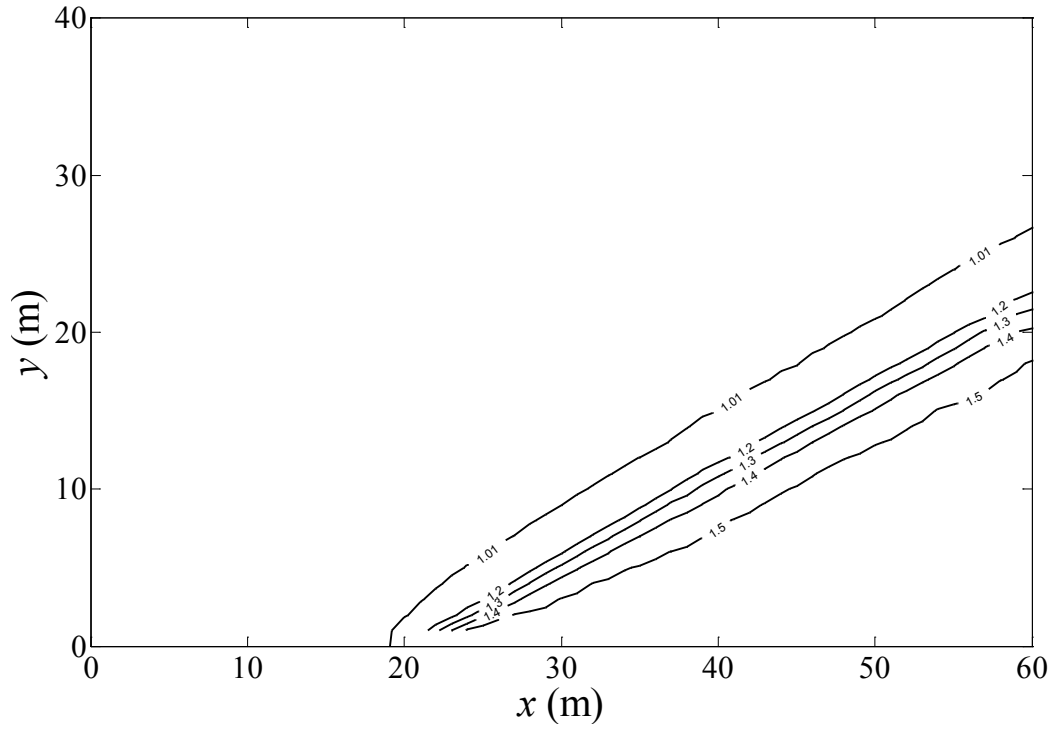

Figure 5.3 Computed water surface contour for the oblique hydraulic jump test

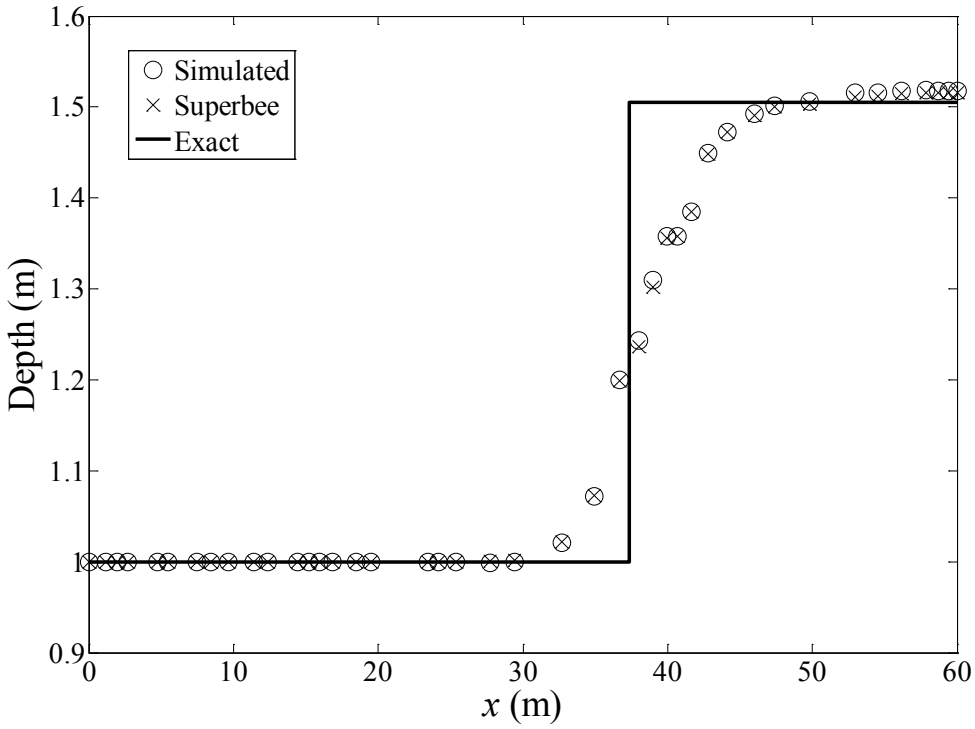

Figure 5.4 Computed and exact depth along solid line aa′

5.2 Shock wave in channel contraction

The steady supercritical shock wave due to channel contraction is simulated to test the numerical scheme. The plan view of shock wave in a symmetric channel contraction is illustrated in Figure 5.5. In the figure, L_{ab} is the length of the channel contraction, α_2 is the angle of wall deflection, β_2 and β_3 are the shock front angles. The flow velocities in regions 1, 2, and 3 are V_1, V_2, and V_3, respectively. Ippen and Dawson (1951) showed that a proper width ratio B_1/B_3 could minimize the disturbance in region 3 and limit the standing shock waves within the contraction part. In the following, the channel contraction suggested by Lin et al. (2005) is adopted, so that results can be compared with exact solutions and other numerical schemes. The geometry and

computational mesh of the channel is shown in Figure 5.6. The channel width at the upstream end is 20 m and the width at the downstream end is 10.548 m, angle of wall deflection (α_2) is 12 degrees, and the length of contraction (L_{ab}) is 22.234 m.

For the inflow boundary conditions, the Froude number is 2.7, the water depth is 1 m, the longitudinal velocity is 8.4566 m/s, and the lateral velocity is zero. The exact solution of shock wave angles is found to be as β_2=33.69° and β_3=48.10°, while the water depth in region 2 and region 3 are 1.868 m and 2.562 m, respectively.

Steady flow solutions for water depth are shown in Figure 5.7 and Figure 5.8 with a coarse mesh (3632 elements, see Figure 5.6). Figure 5.9 and Figure 5.10 show a comparison of the exact solution and the simulated water depth along the dash line and the solid line, respectively (see Figure 5.6). Results from the coarse mesh and a refined mesh (14528 elements) are compared to show that the numerical scheme can perform adequately even for a coarse mesh. Results using the refined mesh show better resolution at the shock, and weaker oscillation after the shock.

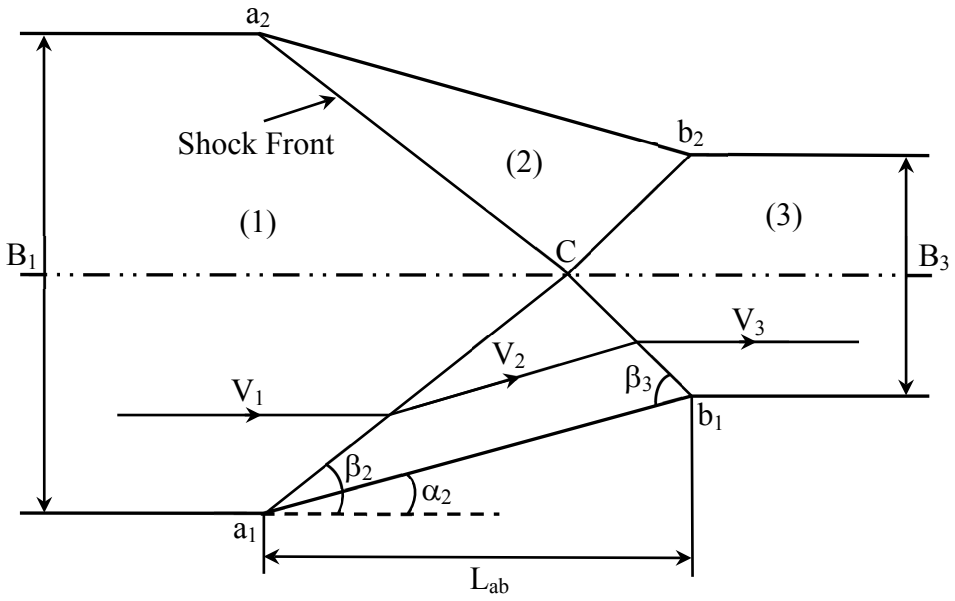

Figure 5.5 Plan view of shock wave in a symmetric channel contraction

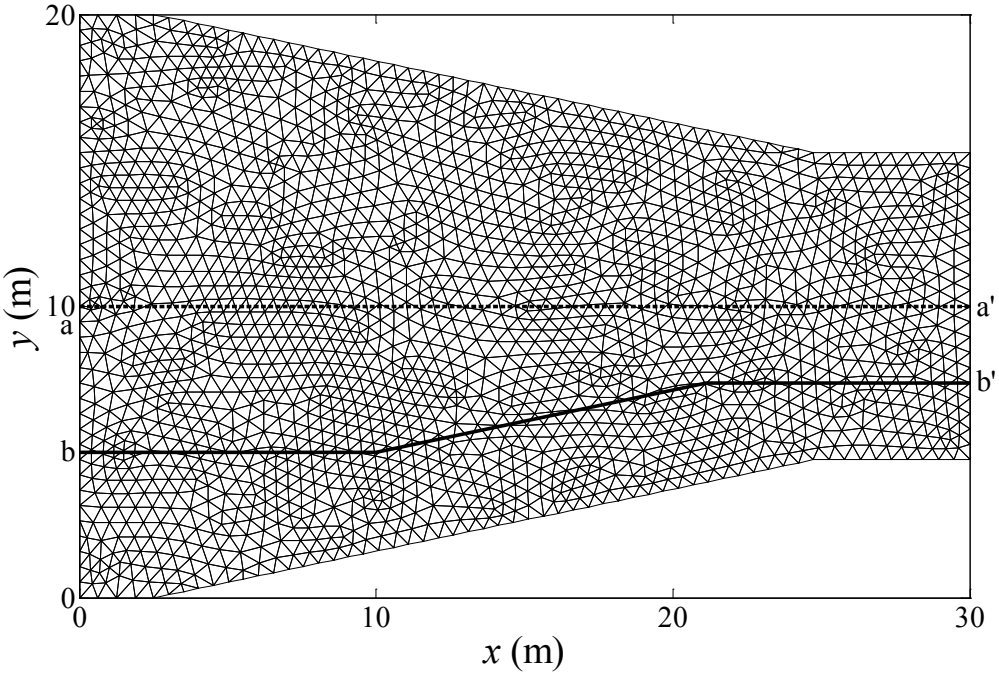

Figure 5.6 Computation domain and mesh for the symmetric channel contraction

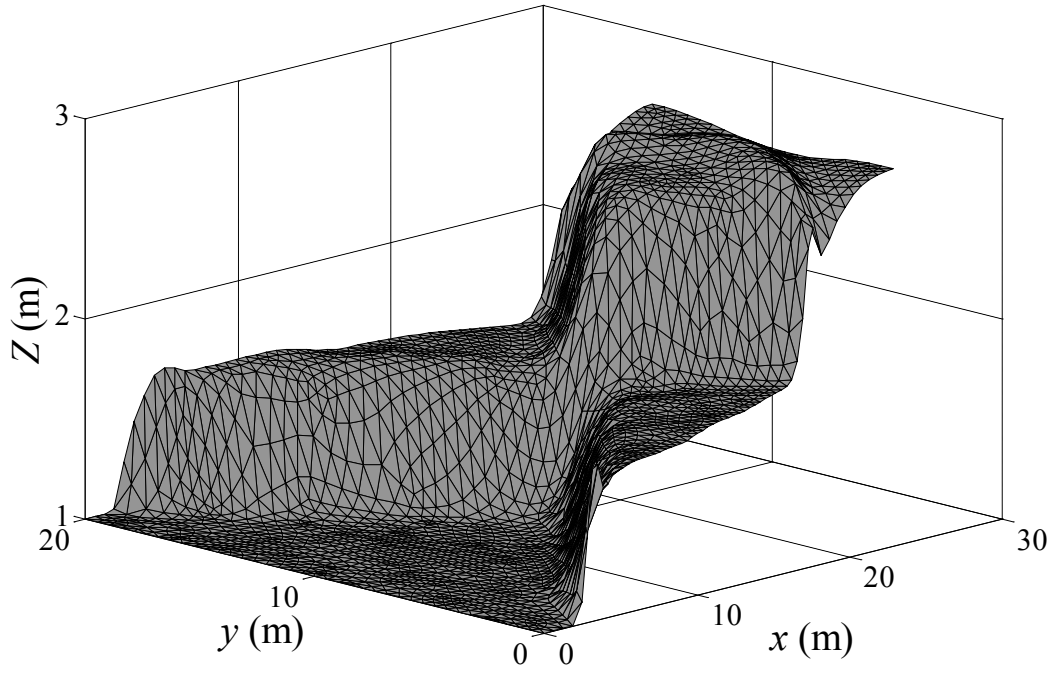

Figure 5.7 Water surface profile for in the symmetric channel contraction

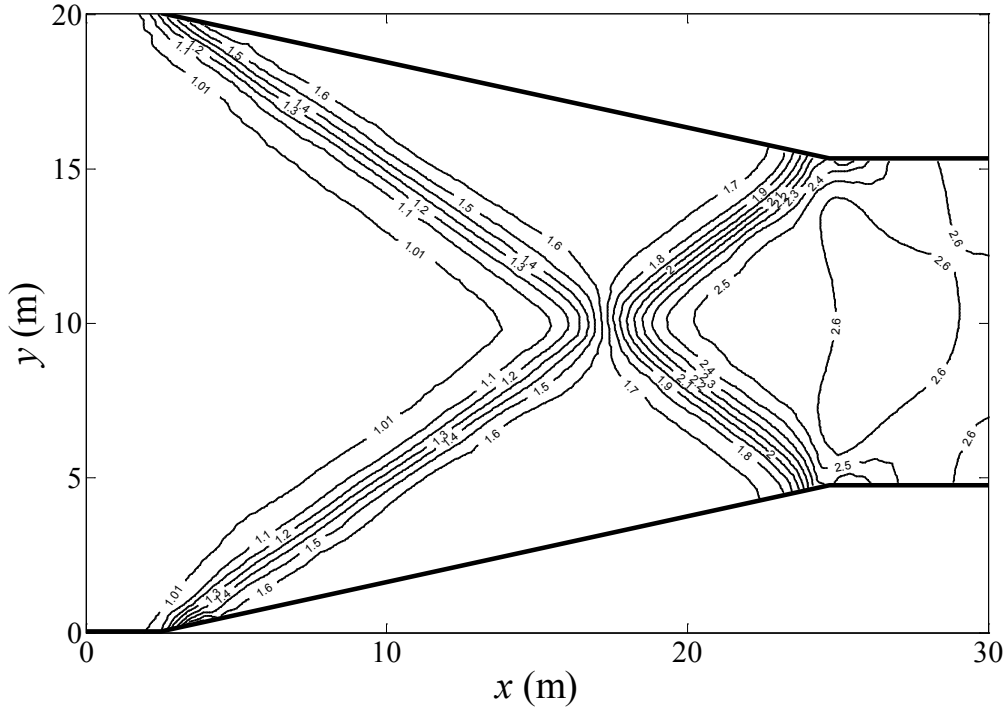

Figure 5.8 Water depth contour in the symmetric channel contraction

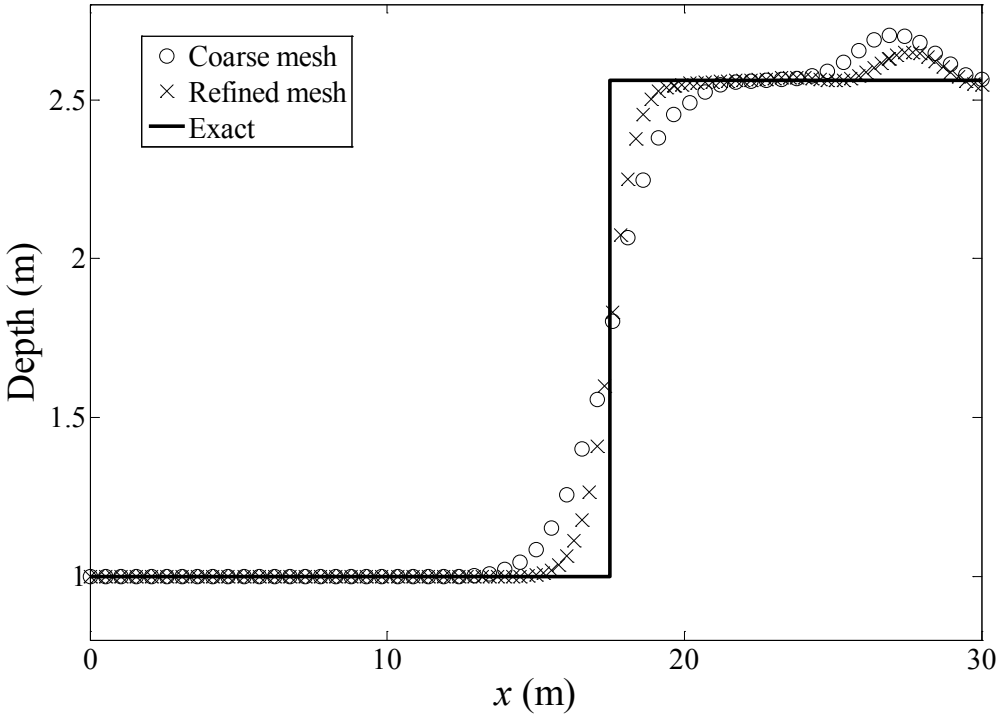

Figure 5.9 Comparison of water depths along the dash line

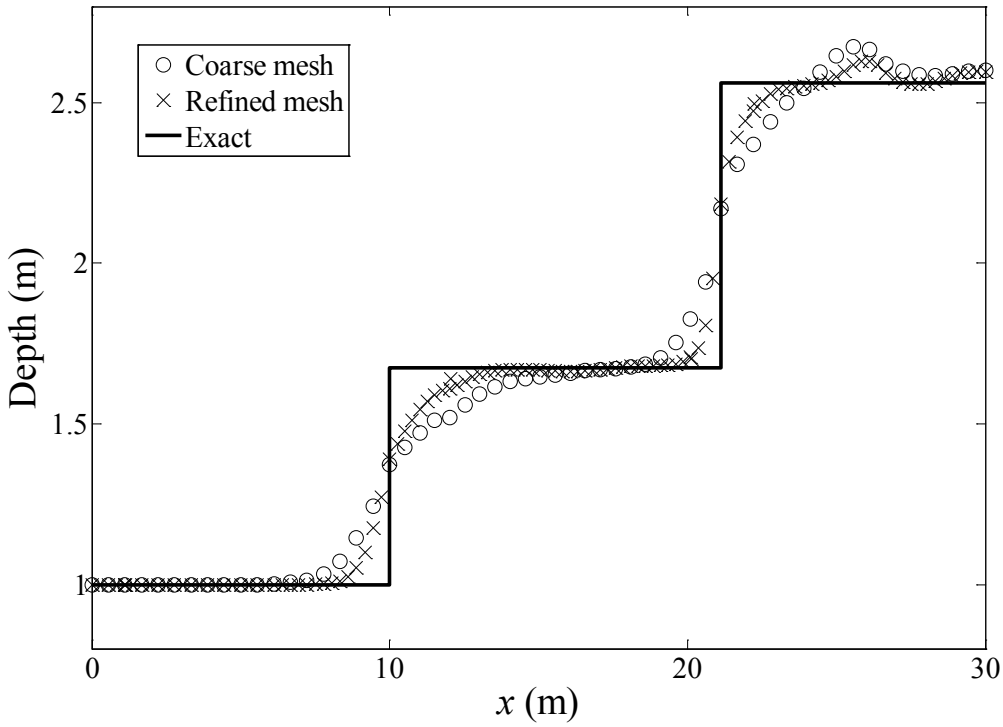

Figure 5.10 Comparison of water depths along the solid line

5.3 Wetting and drying in parabolic bowl

Thacker (1981) provided an analytical solution for the case of two-dimensional axisymmetric oscillating free surface in a parabolic bowl with a moving shoreline. The exact solution has been used by various researchers (Song et al., 2011; Bunya et al., 2009; Ern et al., 2008) to model the drying and wetting capabilities of the numerical schemes.

The bottom profile, z_b, of the parabolic bowl (Figure 5.11), is given by

$$z_b = D_o\left(\frac{r^2}{L^2}-1\right); \quad r=\sqrt{x^2+y^2} \tag{5.1}$$

where D_o is the distance to the bed from the datum at the center of the parabola and L is the distance from the center point to the zero elevation on the shoreline for the leveled water surface. The analytic solution for the water surface (initial profile as well as profile at any time) and the velocity components in the frictionless bowl in the region where water depth is nonzero are given by (Thacker, 1981)

$$Z\left(x,y,t\right)=D_o\left\{\frac{\sqrt{\left(1-A^2\right)}}{1-A\cos\left(\omega t\right)}-1-\frac{r^2}{L^2}\left[\frac{\left(1-A^2\right)}{\left(1-A\cos\left(\omega t\right)\right)^2}-1\right]\right\} \tag{5.2}$$

$$\left(u\left(x,y,t\right),v\left(x,y,t\right)\right)=\frac{1}{2}\frac{\omega A\sin\left(\omega t\right)}{1-A\cos\left(\omega t\right)}\left(x,y\right) \tag{5.3}$$

where ω and A are given by

$$\omega=\frac{2\pi}{T}=\frac{\sqrt{8gD_o}}{L} \tag{5.4}$$

$$A = \frac{\left(D_o + Z_o\right)^2 - D_o^2}{\left(D_o + Z_o\right)^2 + D_o^2} \tag{5.5}$$

and Z_o is the initial water surface elevation at the center of the bowl measured from datum. The region in which the water depth was nonzero was given by

$$r^2 < L^2\left(1 - A\cos(\omega t)\right)\left(1 - A^2\right)^{-0.5} \tag{5.6}$$

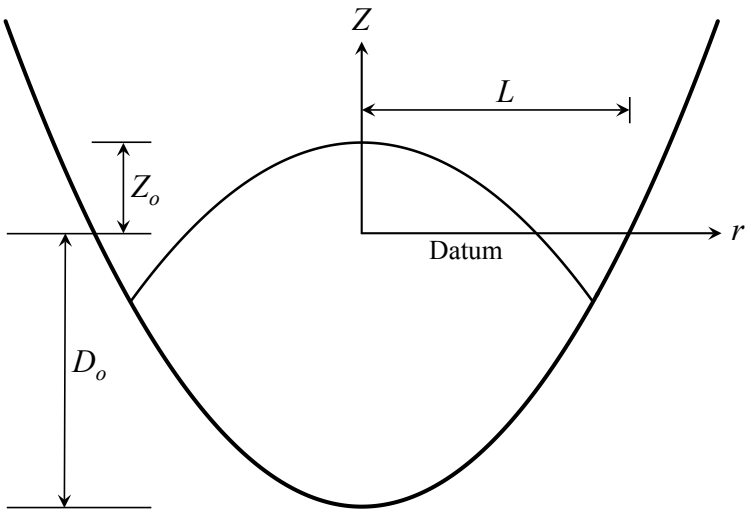

Figure 5.11 Bed profile and initial water surface level

In this numerical test, D_o is 3 m, Z_o is 1 m**,** and L is 3000 m, which gives oscillation period, *T*, of 2457 seconds. The computational domain extends from -4000 m to 4000 m in *x* and *y* directions and is triangulated with 27648 elements and 14033 nodes as shown in Figure 5.12 along with the initial water surface level. Simulated results for water surface and flow rate at different times along the line *y*=0 are shown in Figures 5.13 – 5.24 with two slope limiters. The results show that the wetting and drying process

are handled accurately by the scheme. In addition, the water surface profiles show that the mass is conserved. Overall, the simulated results are in excellent agreement with analytical solutions except for the flow rate at $t = T$, where the flow rate should be zero. The two limiters provide similar results in the beginning, but the Superbee limiter deteriorates in the drying process ($t = 5/6\ T$ and $t = T$) and mass is not conserved.

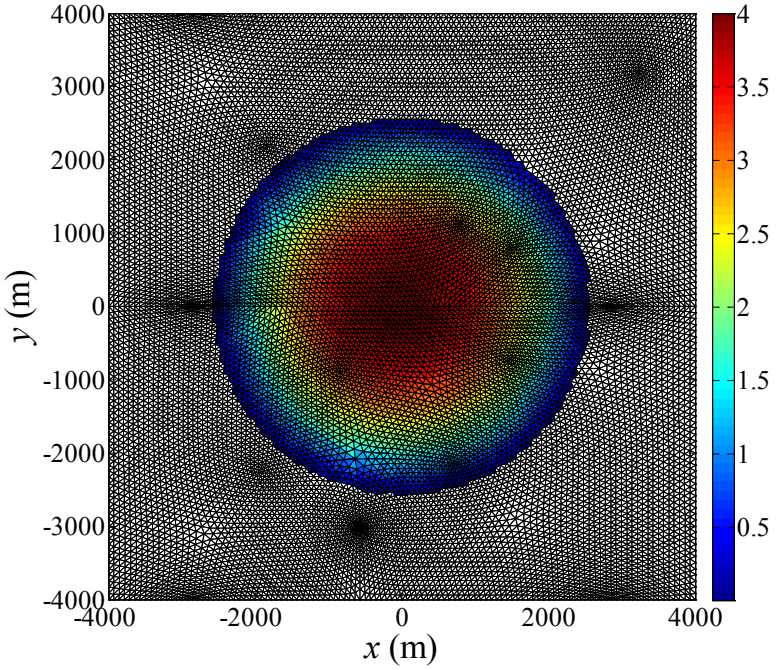

Figure 5.12 Computational domain and initial water depth for parabolic bowl problem

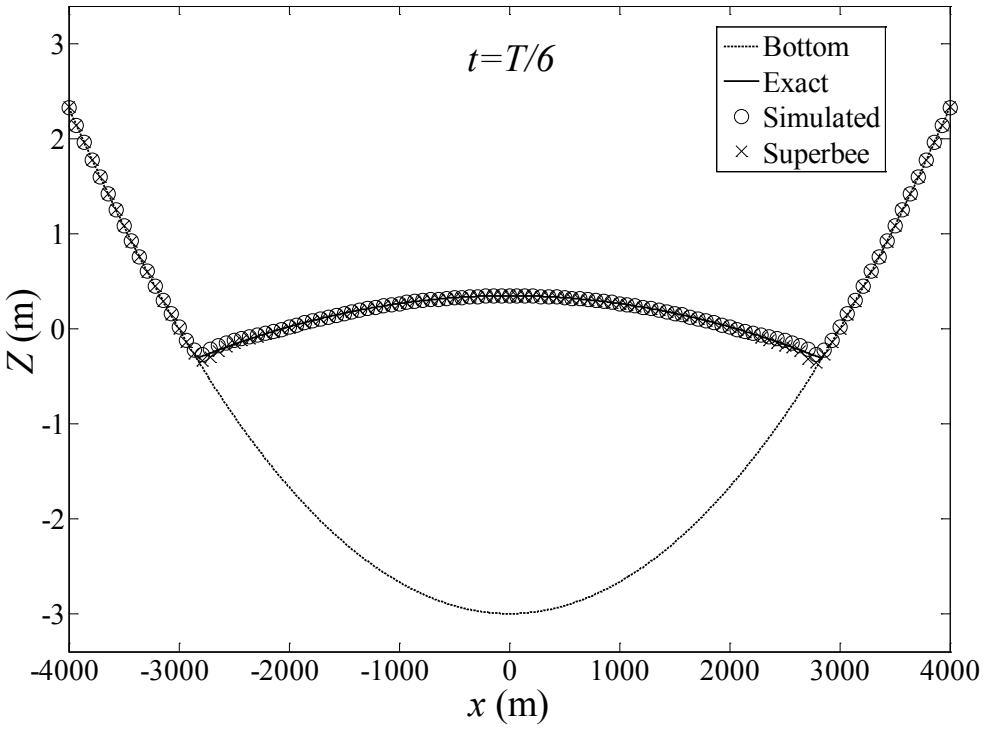

Figure 5.13 Comparison of simulated and exact water surface at $t=T/6$

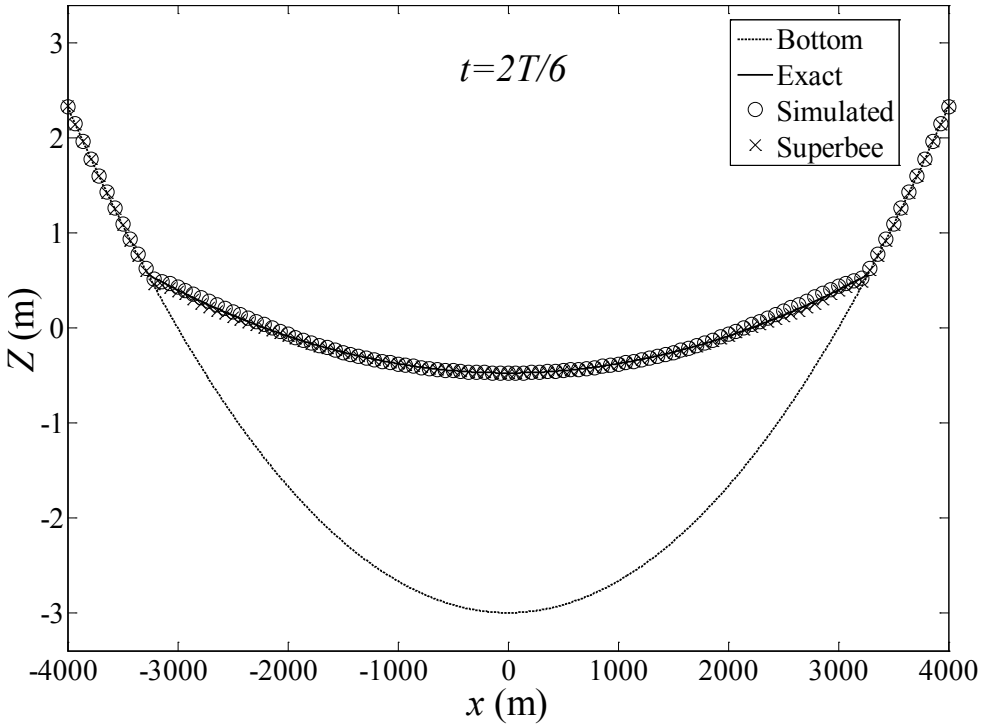

Figure 5.14 Comparison of simulated and exact water surface at $t=2T/6$

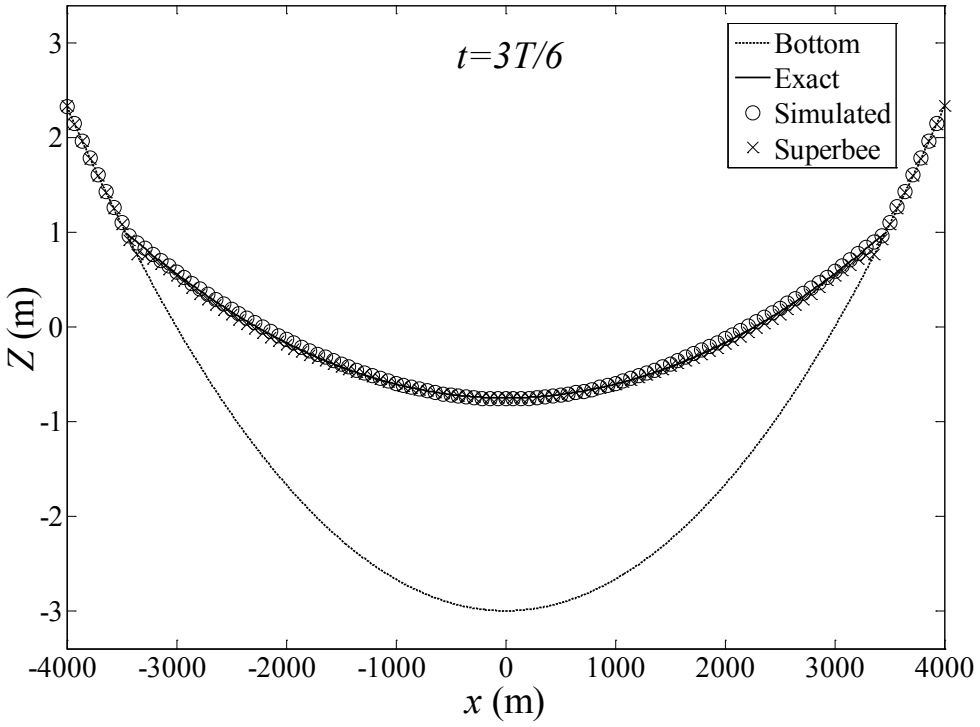

Figure 5.15 Comparison of simulated and exact water surface at t=3T/6

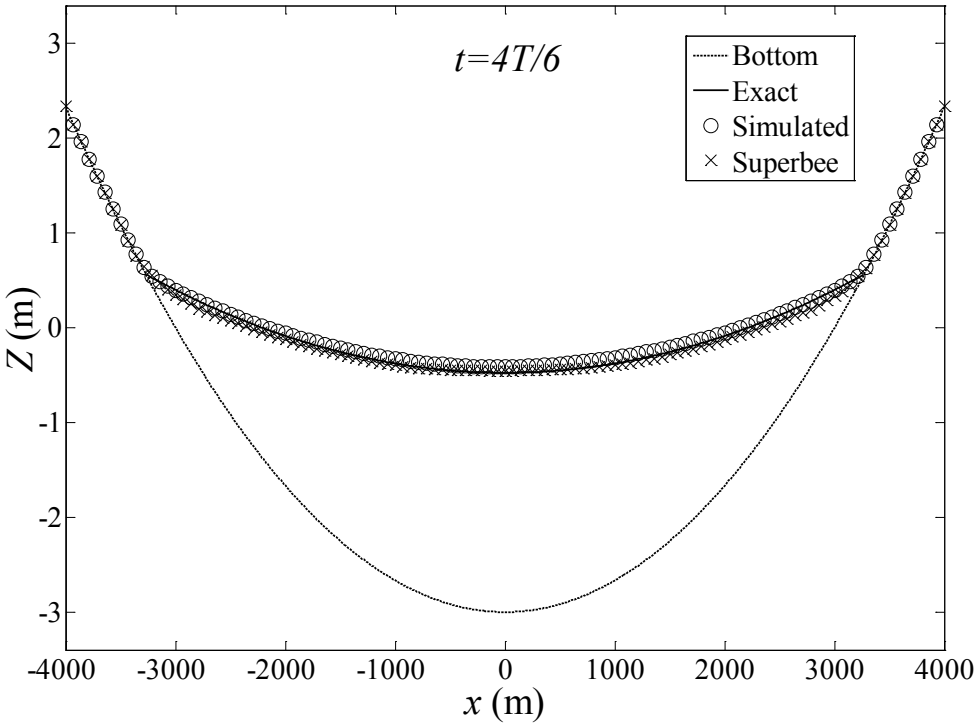

Figure 5.16 Comparison of simulated and exact water surface at t=4T/6

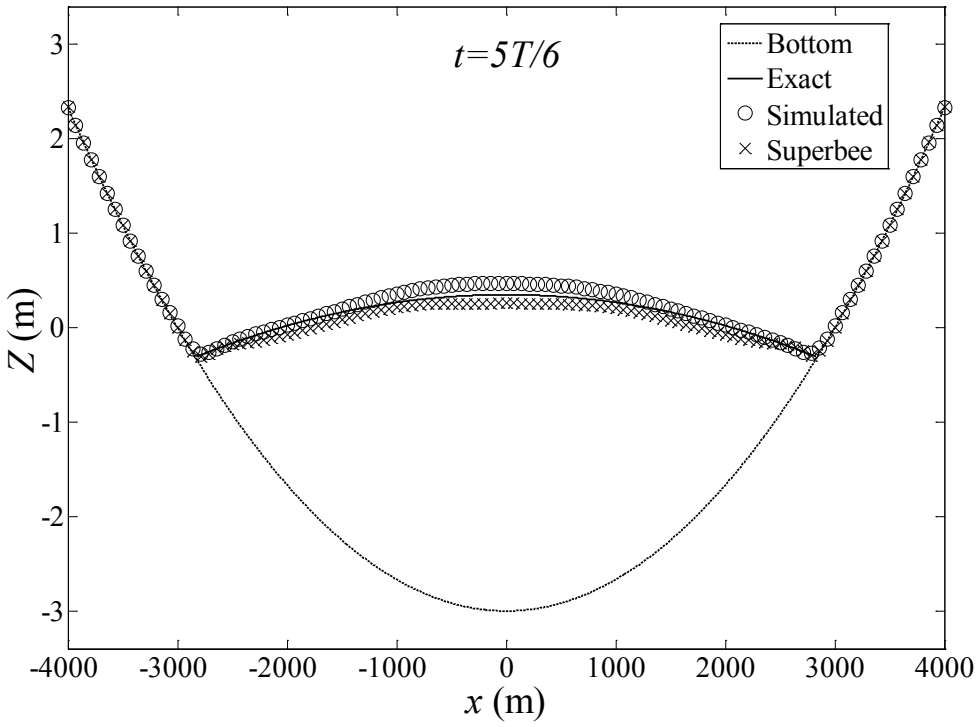

Figure 5.17 Comparison of simulated and exact water surface at t=5T/6

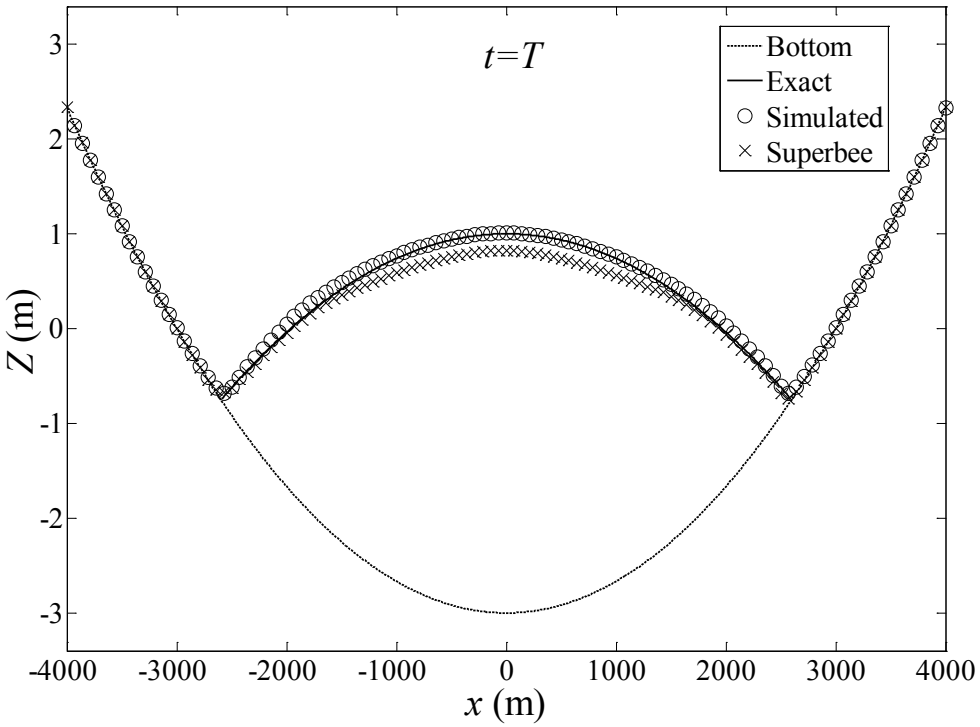

Figure 5.18 Comparison of simulated and exact water surface at t=T

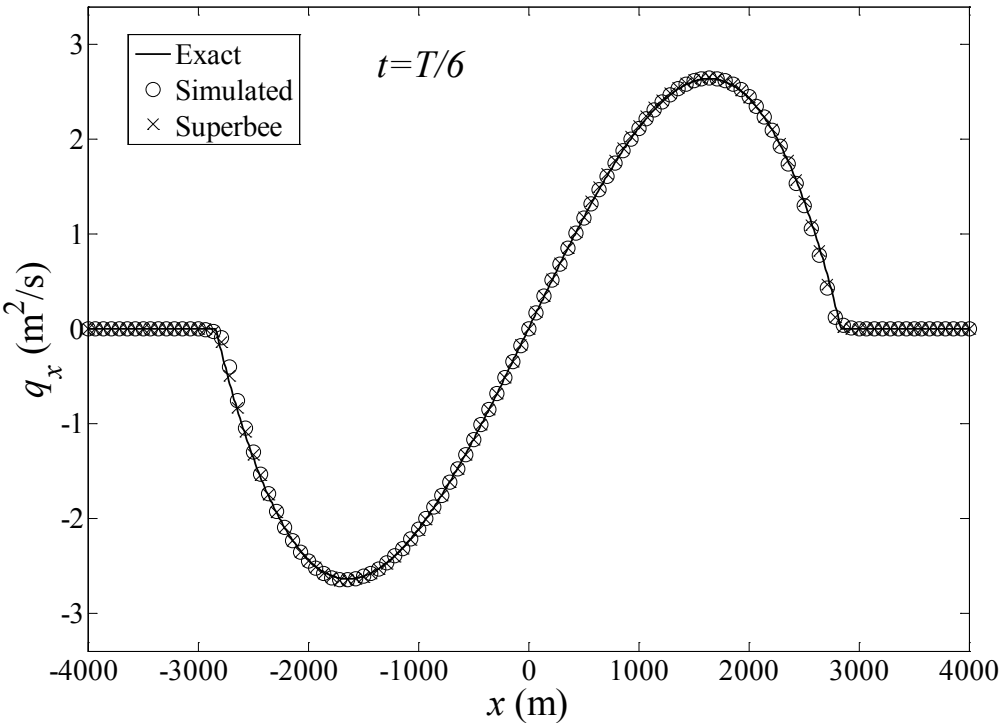

Figure 5.19 Comparison of simulated and exact flow rate at $t=T/6$

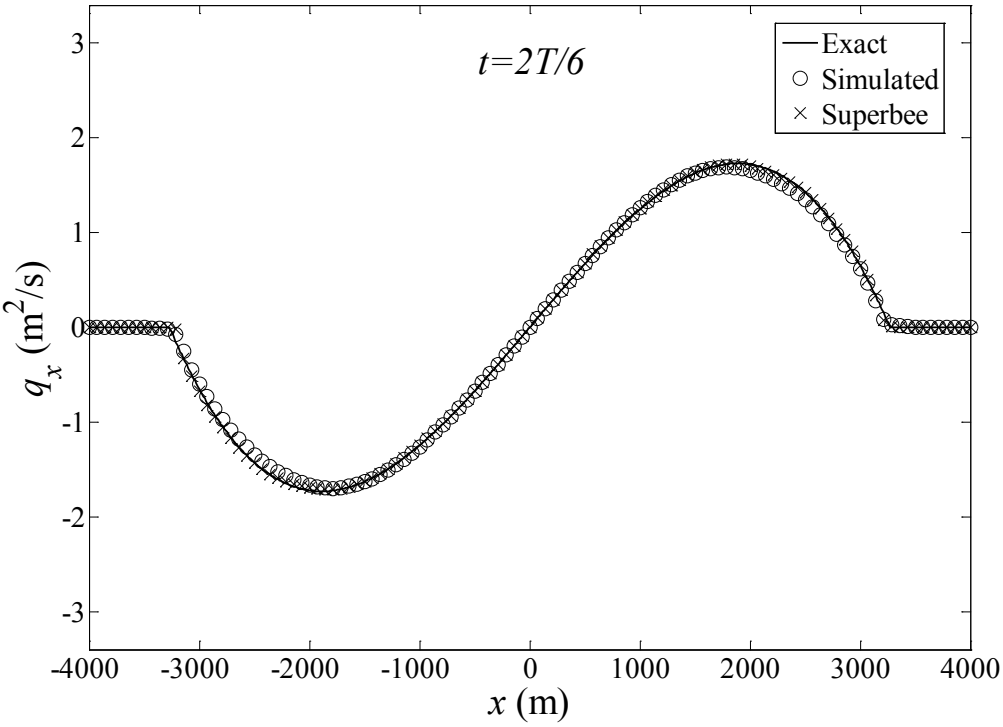

Figure 5.20 Comparison of simulated and exact flow rate at $t=2T/6$

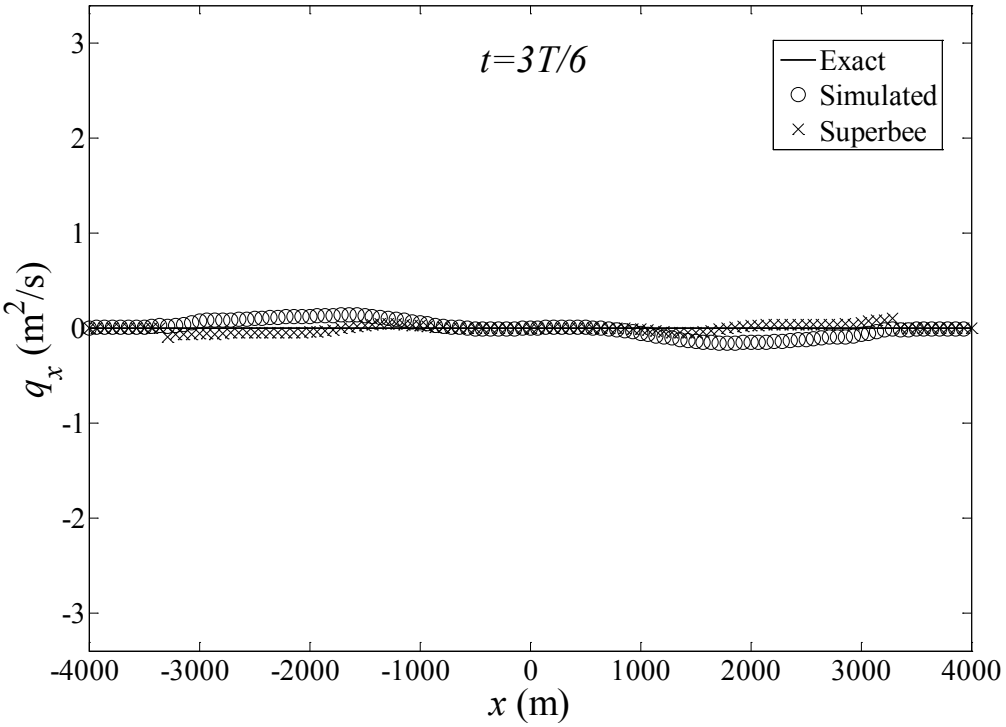

Figure 5.21 Comparison of simulated and exact flow rate at t=3T/6

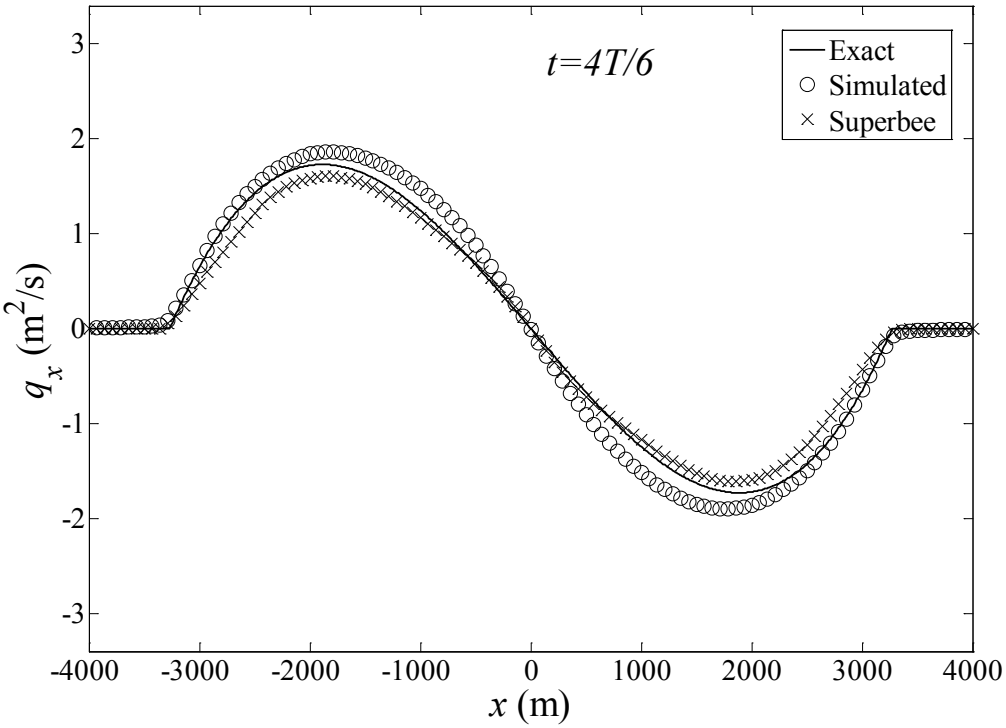

Figure 5.22 Comparison of simulated and exact flow rate at t=4T/6

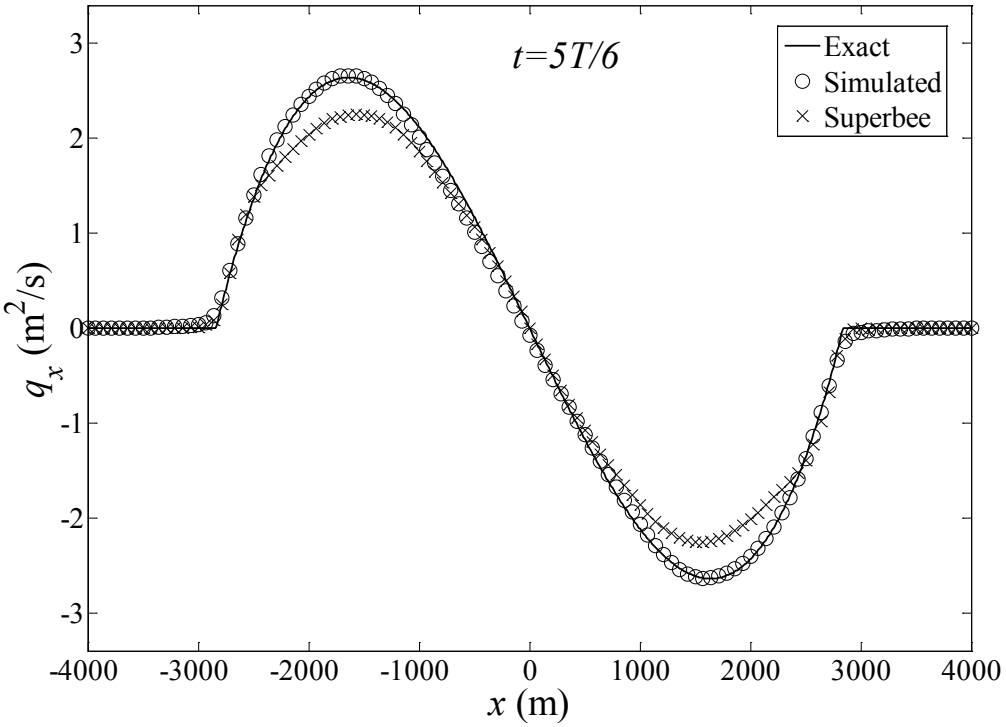

Figure 5.23 Comparison of simulated and exact flow rate at t=5T/6

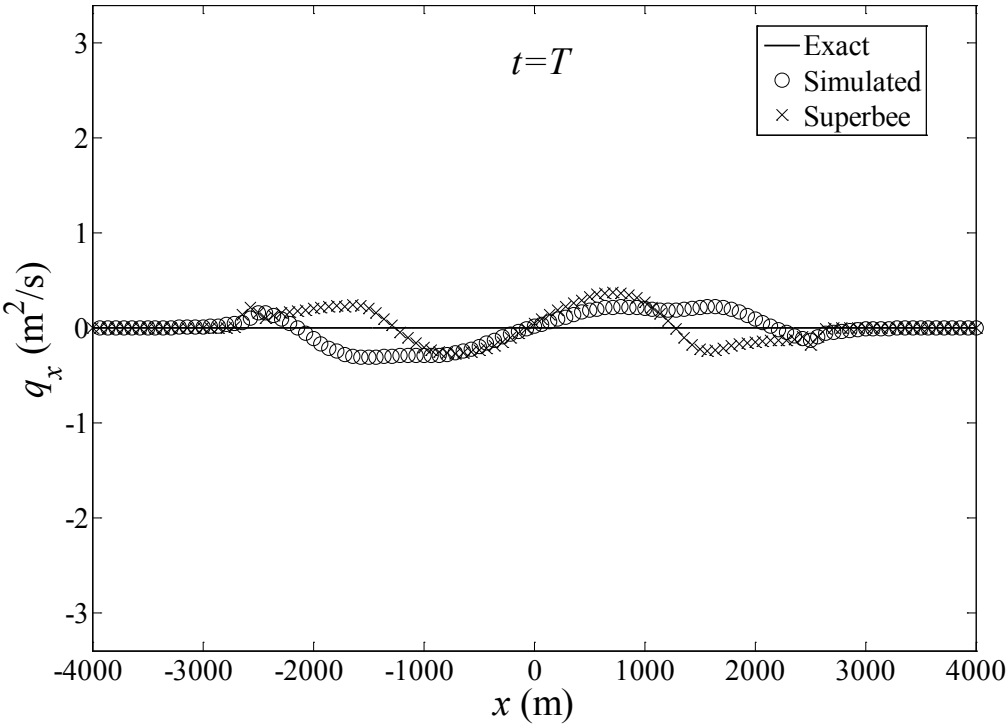

Figure 5.24 Comparison of simulated and exact flow rate at t=T

5.4 Circular dam-break

To test the symmetric shock capturing capability of the scheme, the idealized circular dam-break problem is used (Alcrudo and Garcia-Navarro, 1993; Anastasiou and Chan, 1997; Lin et al., 2003). The problem domain with horizontal bed is shown in Figure 5.25. The radius of the dam is 11 m. Initially, the water depth inside the dam is set to 10 m and water depth outside is 1 m. The circular dam is removed instantaneously and the flow in the domain is computed. Numerical results at 0.8 seconds after the removal of the dam are shown in Figure 5.26 and Figure 5.27. The corresponding velocity field is shown in Figure 5.28. The symmetry of the forward moving wave is well preserved. The initial water volume is 5909 m^3, and the water volume at 0.8 seconds is 5910 m^3, showing the mass is well conserved.

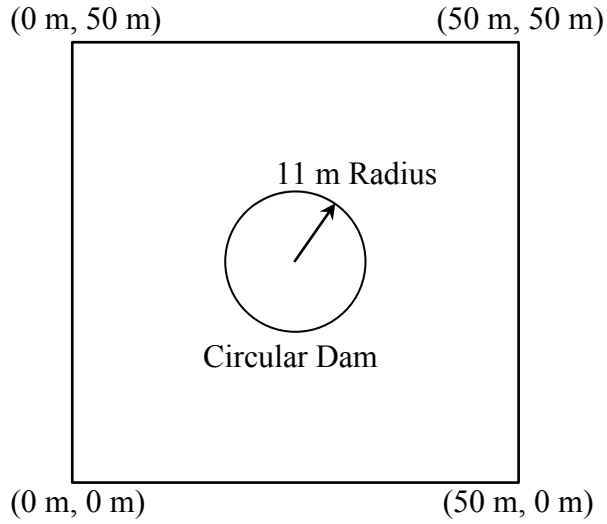

Figure 5.25 Configuration of circular dam-break test

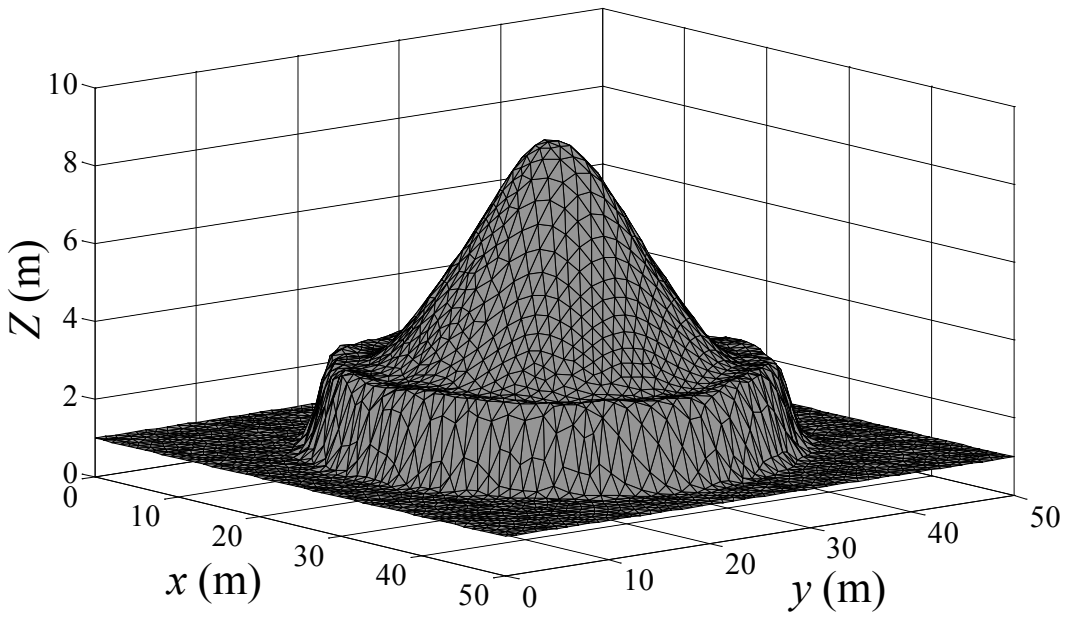

Figure 5.26 Computed water surface at 0.8 s after dam removal

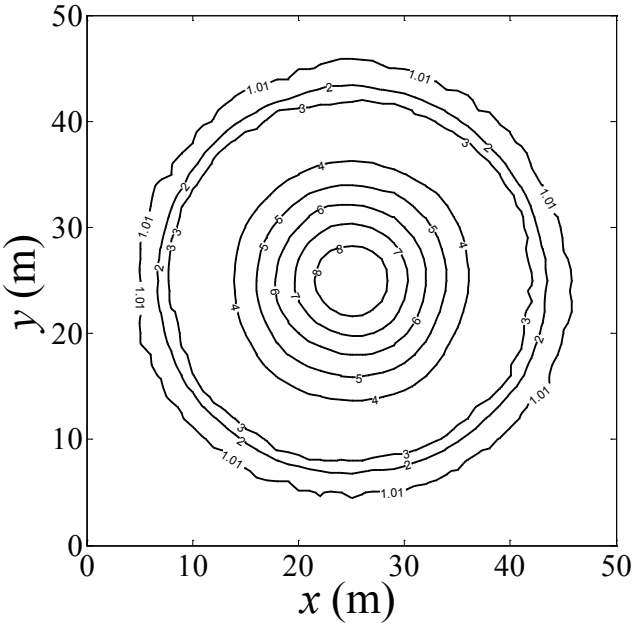

Figure 5.27 Computed water surface contour at 0.8 s after dam removal

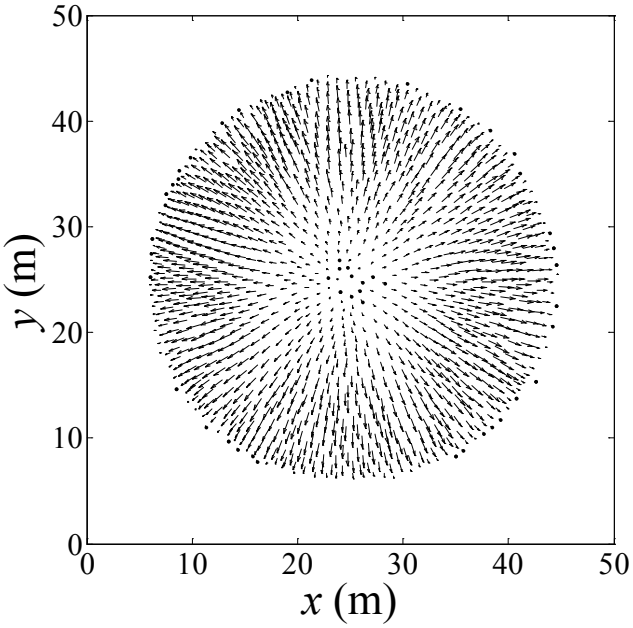

Figure 5.28 Computed velocity field at 0.8 *s* after dam removal

5.5 Shock wave in circular dam-break

The same domain as used in the previous test is adopted here with different initial conditions. The initial water depth is 1 m inside the dam and 10 m outside the dam. After removing the dam, the circular shock moves inwards, passes through the singularity and then expands outwards. The shock at 2 seconds is shown below in Figure 5.29 and Figure 5.30 as water surface in 3D view and water depth contour, respectively. The velocity field is shown in Figure 5.31. Water surface in Figure 5.29 shows the scheme is oscillation free and the diffusion effects are minimal. Water depth contours in Figure 5.30 show that the flow symmetry is well preserved with unstructured elements. The initial water volume is 21591 m^3, and the water volume at 2 seconds is 21590 m^3, showing the mass conservation is well preserved in this model.

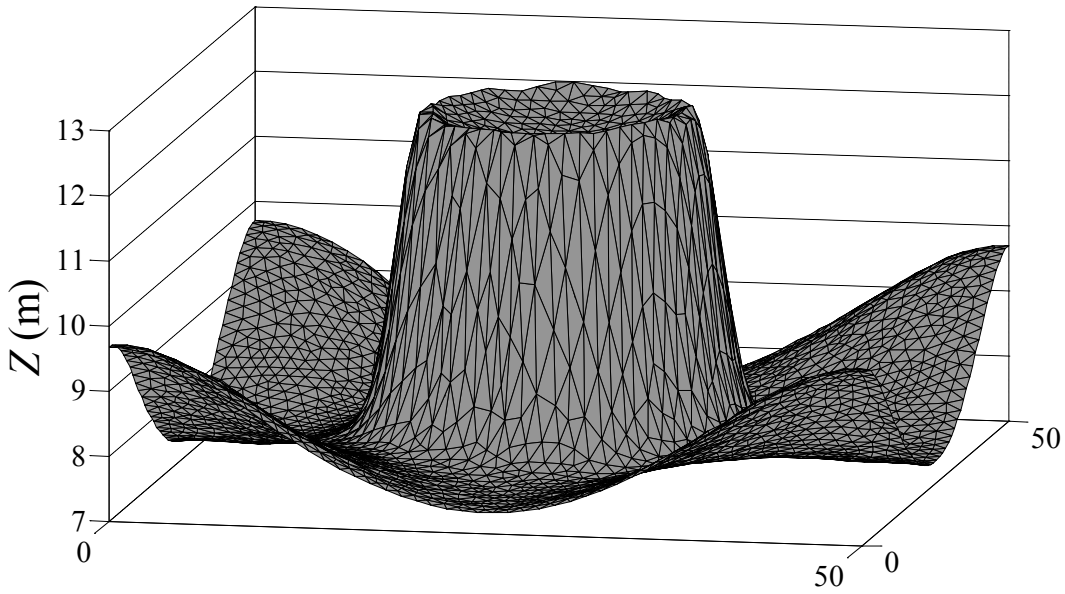

Figure 5.29 Computed water surface at 2 s

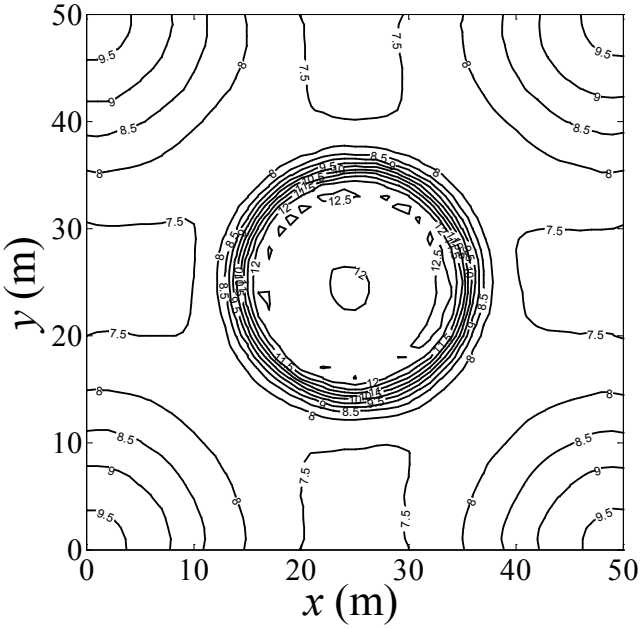

Figure 5.30 Computed water surface contour at 2 s

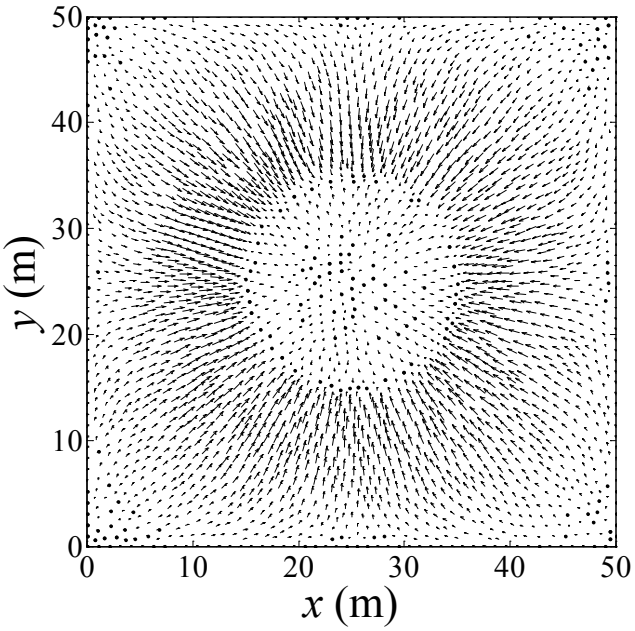

Figure 5.31 Computed velocity field at 2 s

5.6 Partial dam-break

The idealized partial dam-break problem has been investigated by previous researchers (Lin et al., 2003; Anastasiou and Chan, 1997; Alcrudo and Garcia-Navarro, 1993) to test the shock capturing capability of numerical schemes. In this study, both wet bed and dry bed partial dam-break problems over a horizontal bed are examined. The domain configuration and numerical discretization (using 5280 elements) are shown in Figure 5.32. The dam is located at the middle of the channel. The water depth upstream of the dam is 10 m and the downstream water depth is initially set at 5 m and 0 m for the wet bed and dry bed tests, respectively. The dam is assumed to fail instantaneously in both tests, and water is released through a 75 m wide breach. Simulation results for the water depth are computed at 7 seconds and 6 seconds after the dam failure for the wet

bed and dry bed tests, respectively. Results for water surface in 3-D view and water depth contour are shown in Figure 5.33 – 5.36. The two tests show that the scheme is capable of modeling shocks resulting from dam-break flows over dry and wet beds in irregular geometry.

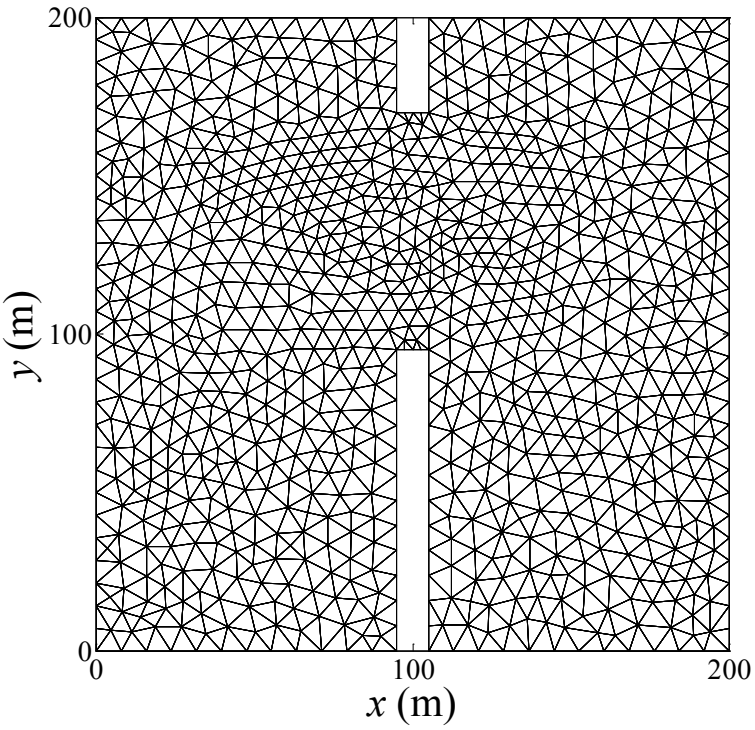

Figure 5.32 Computational domain and mesh discretization for the partial dam-break tests

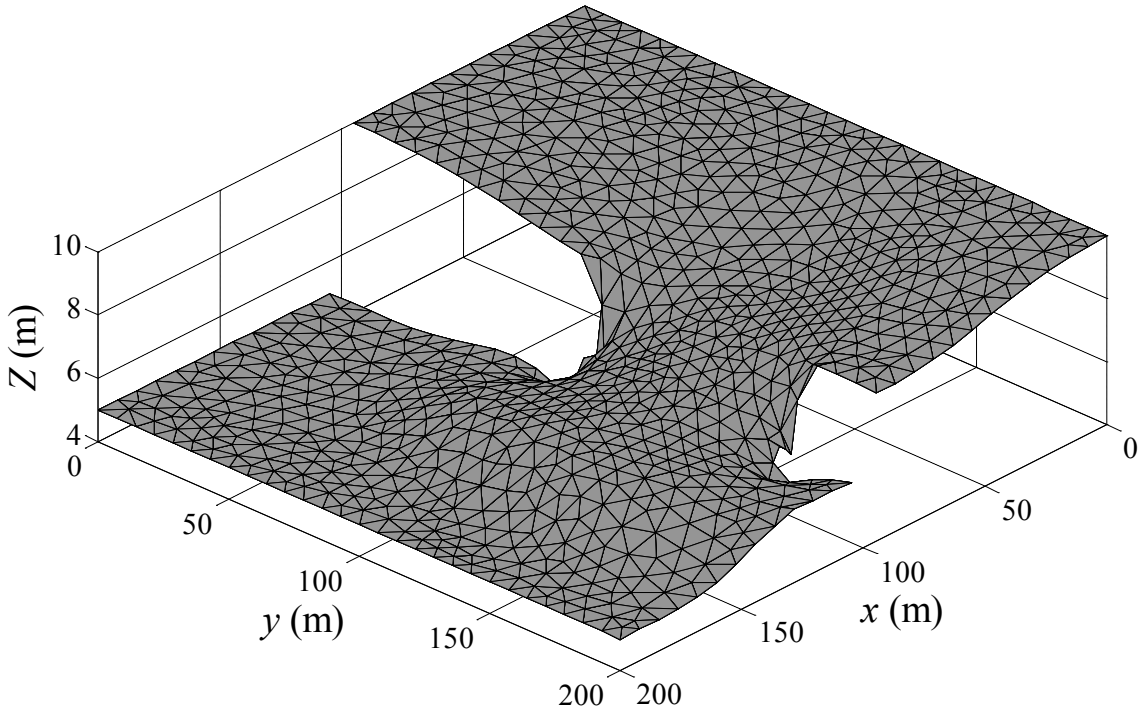

Figure 5.33 Computed water surface for wet bed partial dam-break test

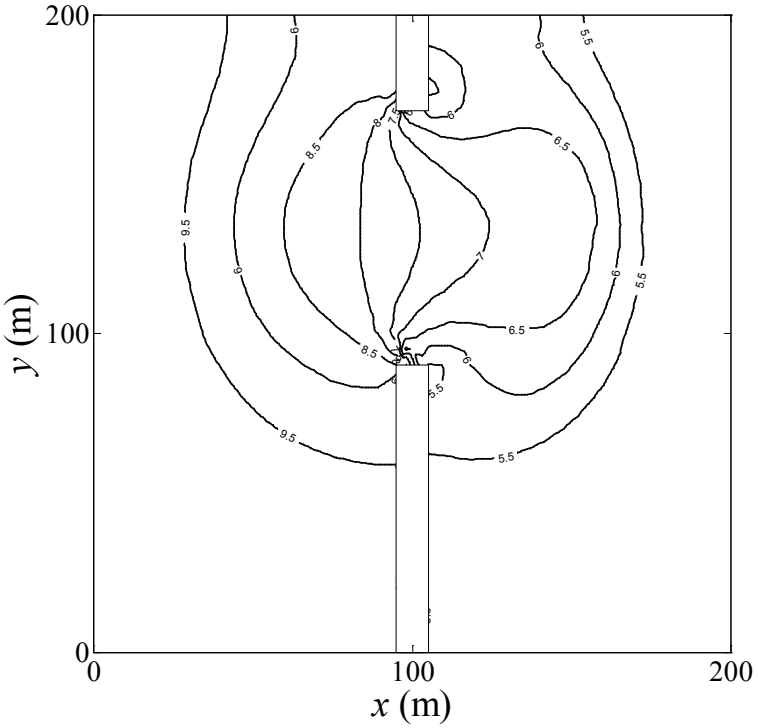

Figure 5.34 Computed water surface contour for wet bed partial dam-break test

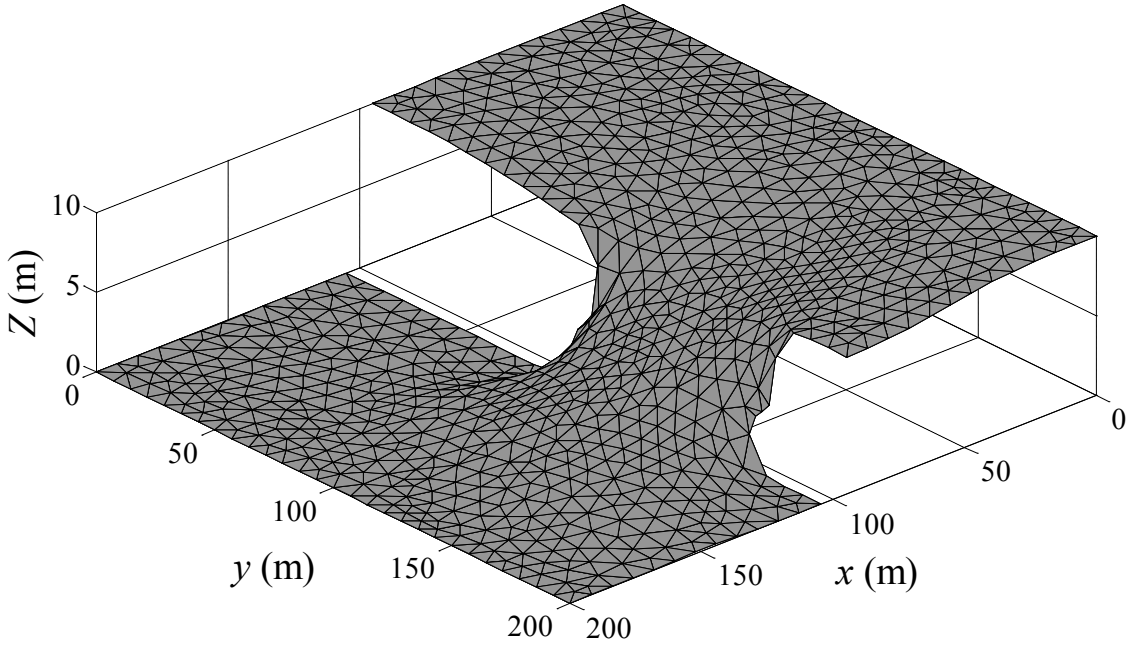

Figure 5.35 Computed water surface for dry bed partial dam-break test

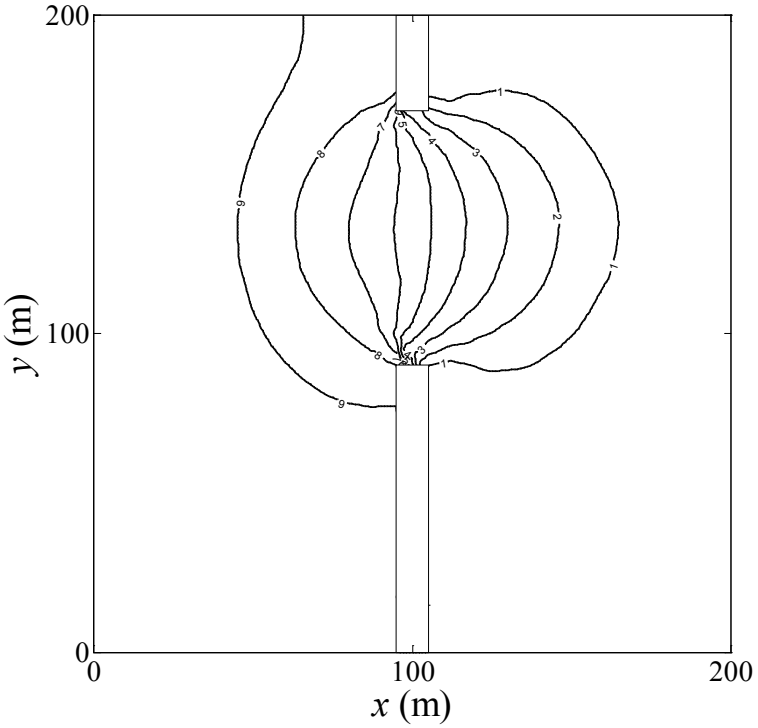

Figure 5.36 Computed water surface contour for dry bed partial dam-break test

5.7 Dam-break in a channel with 45° bend

Physical models were built in the Civil Engineering Department Laboratory, Université Catholique de Louvain (UCL, Belgium) to model dam-break and strong transient flows in sharp bends. Experimental data were collected and used to validate numerical models developed by the CADAM group (Soares Frazão et al., 1999).

The plan view of the channel with horizontal bed and 45° bend is shown in Figure 5.37. The gauge points are also shown in the figure and their positions are listed in Table 5.1. The dam is represented by a gate at the outlet of the reservoir. The gate is pulled up rapidly to simulate the instantaneous failure of the dam. The initial water level in the upstream reservoir is 0.25 m above the horizontal channel bed, and the channel downstream is dry. The Manning's roughness coefficients of 0.0095 $s/m^{1/3}$ for bottom and 0.0195 $s/m^{1/3}$ for wall, as suggested by Soares Frazão et al. (1999), are adopted. These values for Manning's roughness are based on the steady uniform flow.

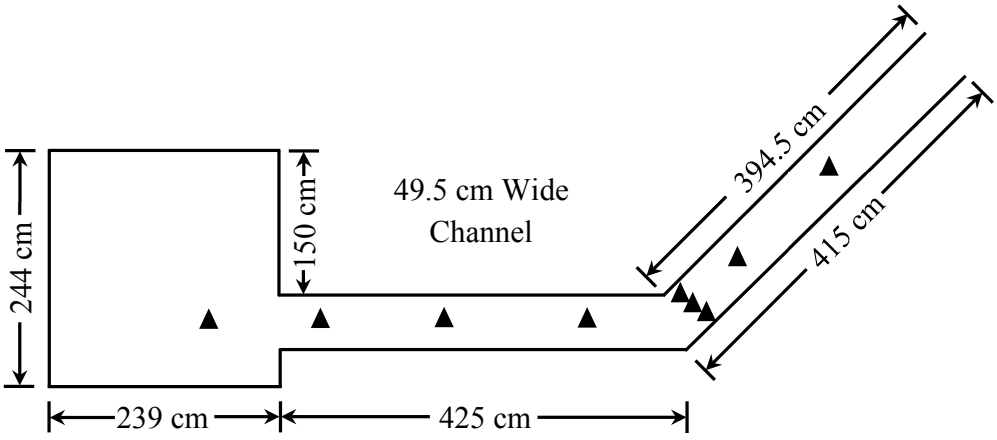

Figure 5.37 Plan view of channel with 45° bend

Table 5.1 Gauge point locations in 45^0 bend

Gauge Point	G1	G2	G3	G4	G5	G6	G7	G8	G9
***x* (m)**	1.59	2.74	4.24	5.74	6.74	6.65	6.56	7.07	8.13
***y* (m)**	0.69	0.69	0.69	0.69	0.72	0.80	0.89	1.22	2.28

After the removal of the gate, water flows rapidly into the channel and reaches the bend. The water reflects against the wall and a shock forms and moves upstream. The velocity field at 3 seconds is shown in Figure 5.38 and the water surface at 10 seconds is shown in Figure 5.39. The velocity field shows that the flow is two-dimensional at the inlet and in the bend region. The reflected shock wave can be clearly seen in the water surface profile. The simulated hydrographs at 9 gauging points are compared with measured data in Figures 5.40 – 5.48. Numerical results are in good agreement with the measured data, except at G2, which is located at the exit of the reservoir. At G2, the magnitude of the reflected wave and its arrival time are predicted accurately. The difference in the water level drop immediately after the gate opening may be related to difference in the manner in which the gate is actually opened and simulated. It should be mentioned that the simulated results are similar to or better than that reported by previous studies.

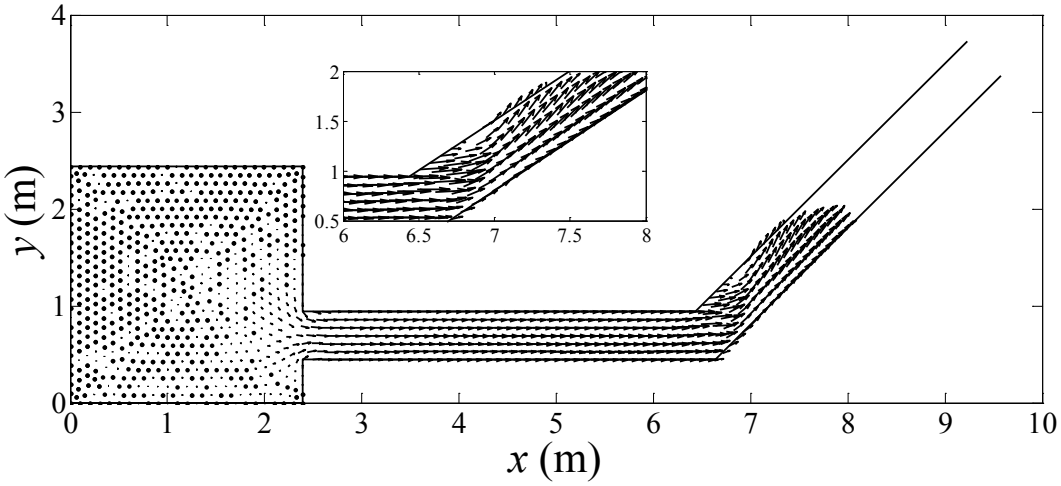

Figure 5.38 Velocity field at 3 s after dam-break

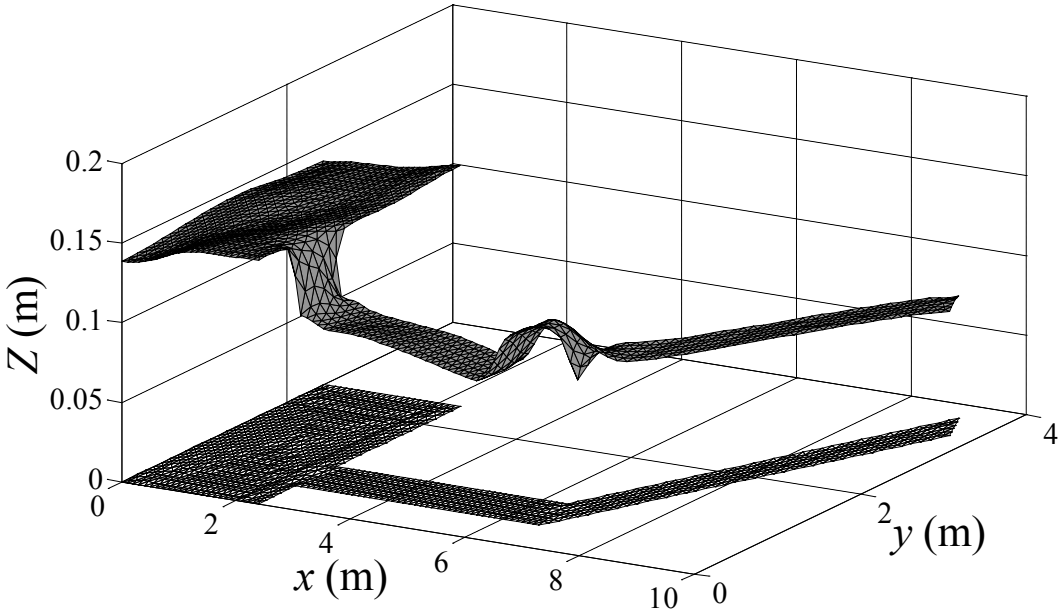

Figure 5.39 Water surface at 10 s after dam-break

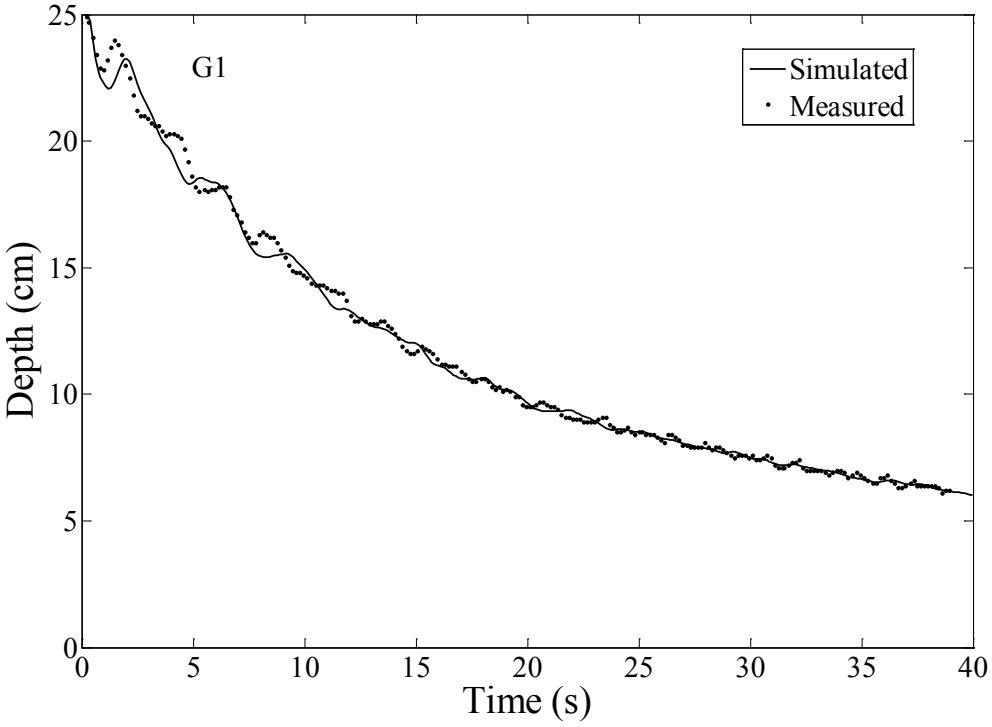

Figure 5.40 Comparison of simulated and measured hydrographs at G1

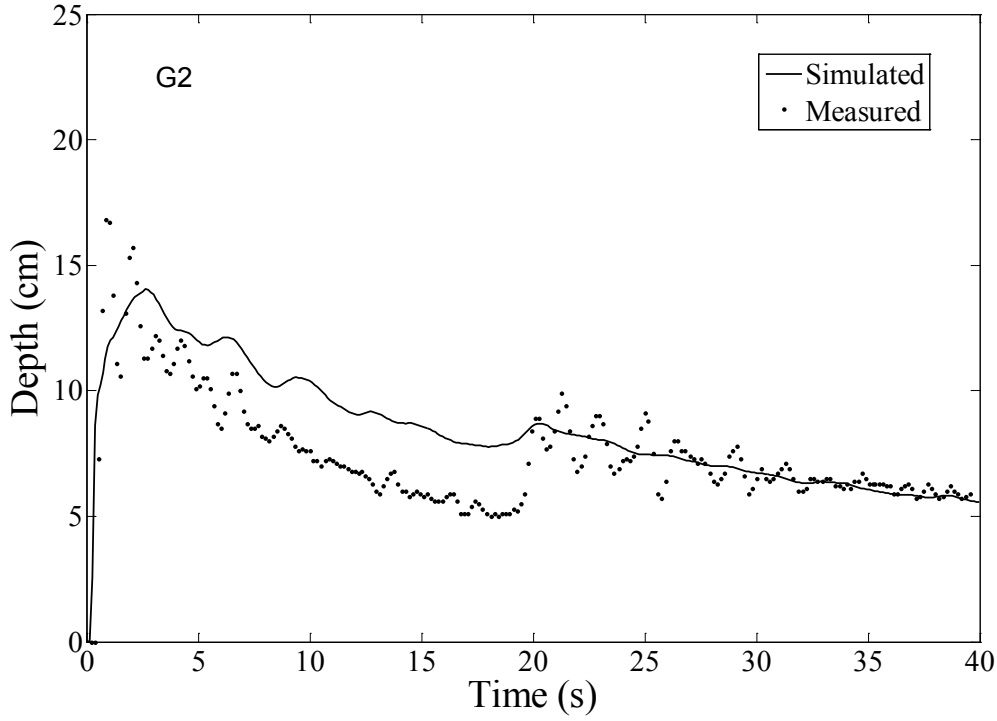

Figure 5.41 Comparison of simulated and measured hydrographs at G2

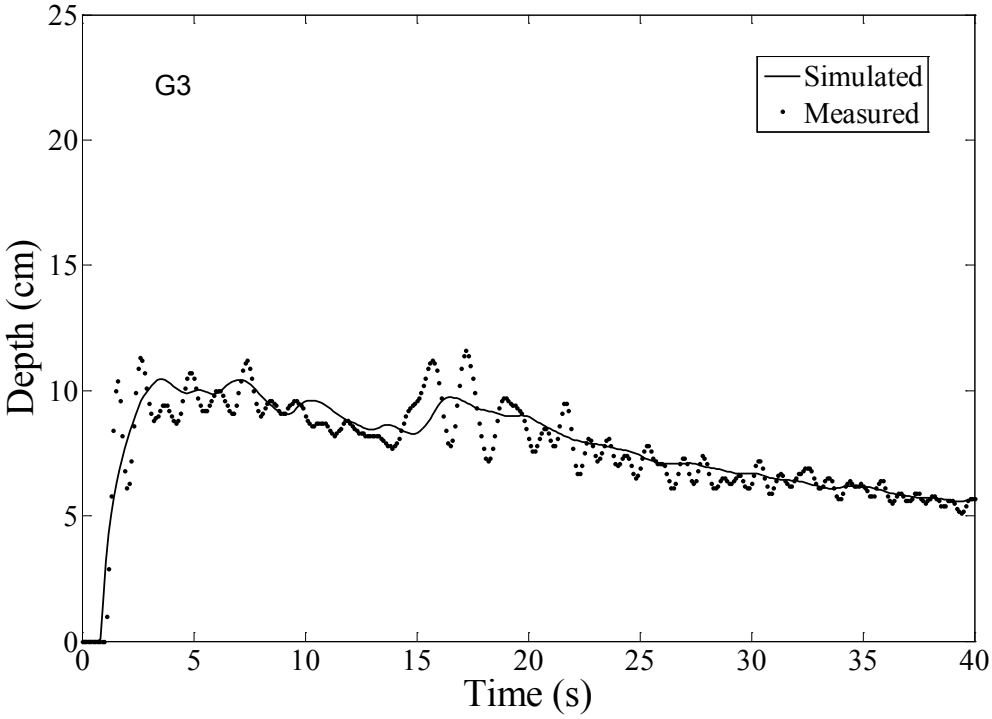

Figure 5.42 Comparison of simulated and measured hydrographs at G3

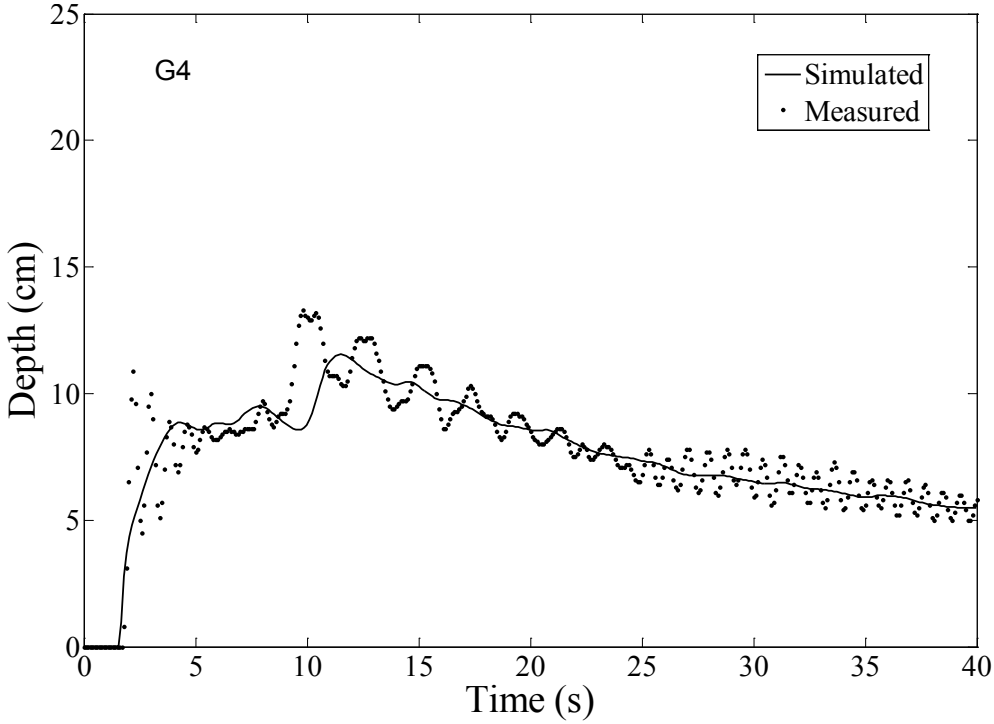

Figure 5.43 Comparison of simulated and measured hydrographs at G4

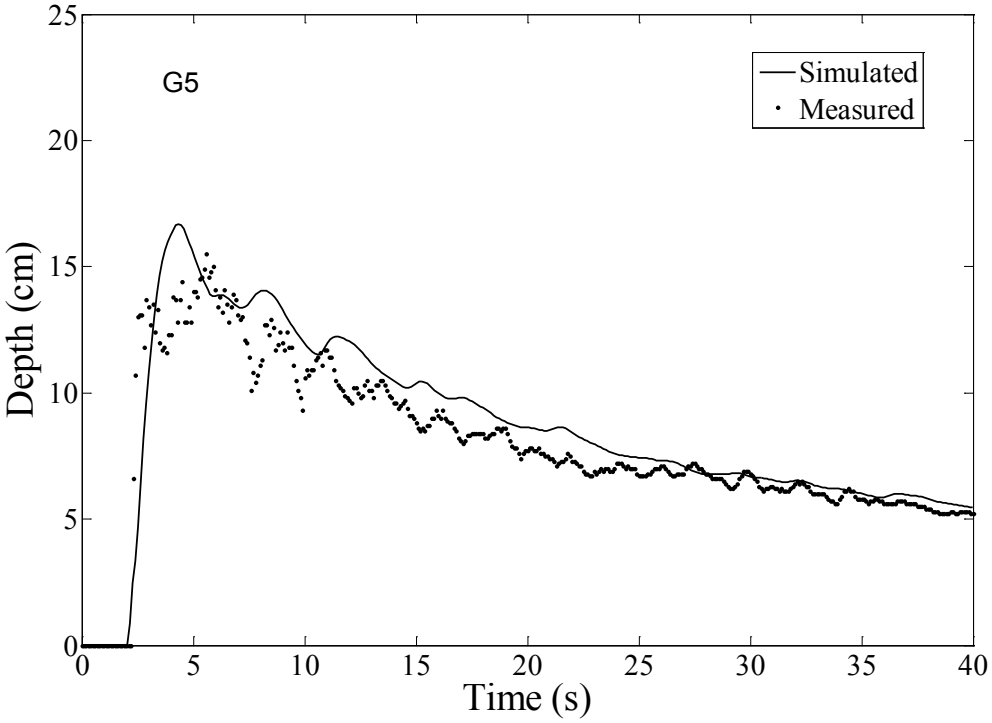

Figure 5.44 Comparison of simulated and measured hydrographs at G5

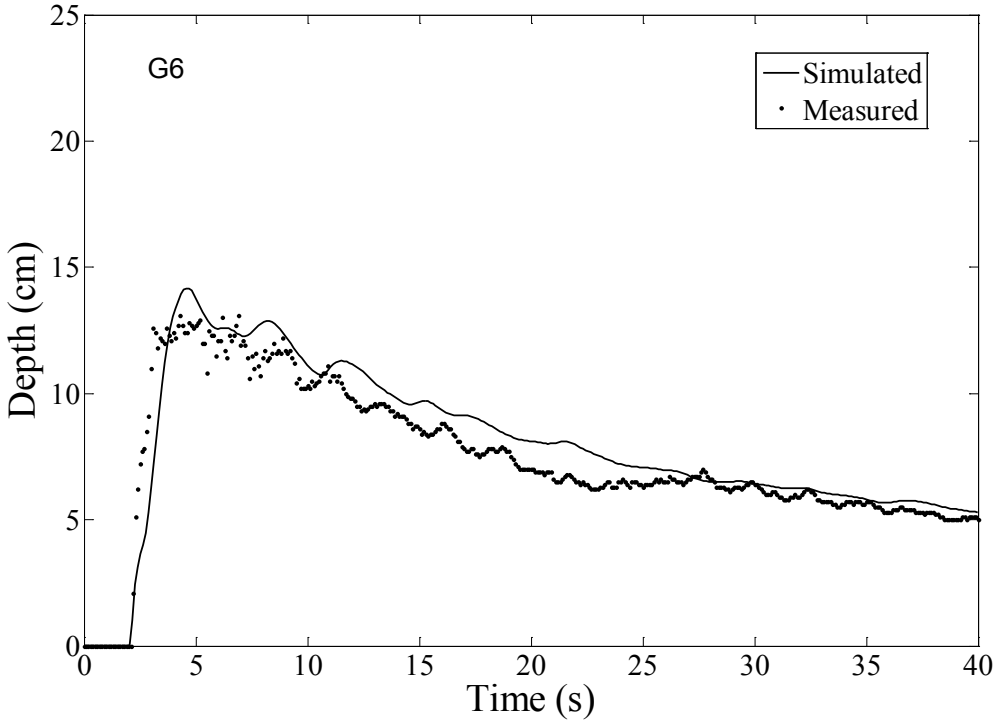

Figure 5.45 Comparison of simulated and measured hydrographs at G6

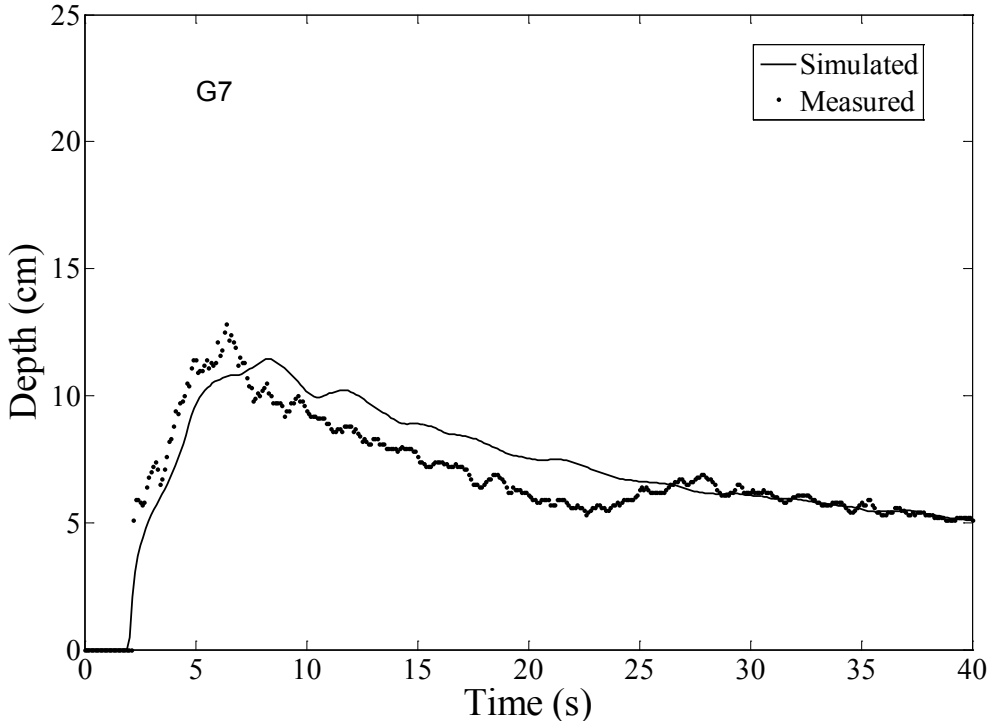

Figure 5.46 Comparison of simulated and measured hydrographs at G7

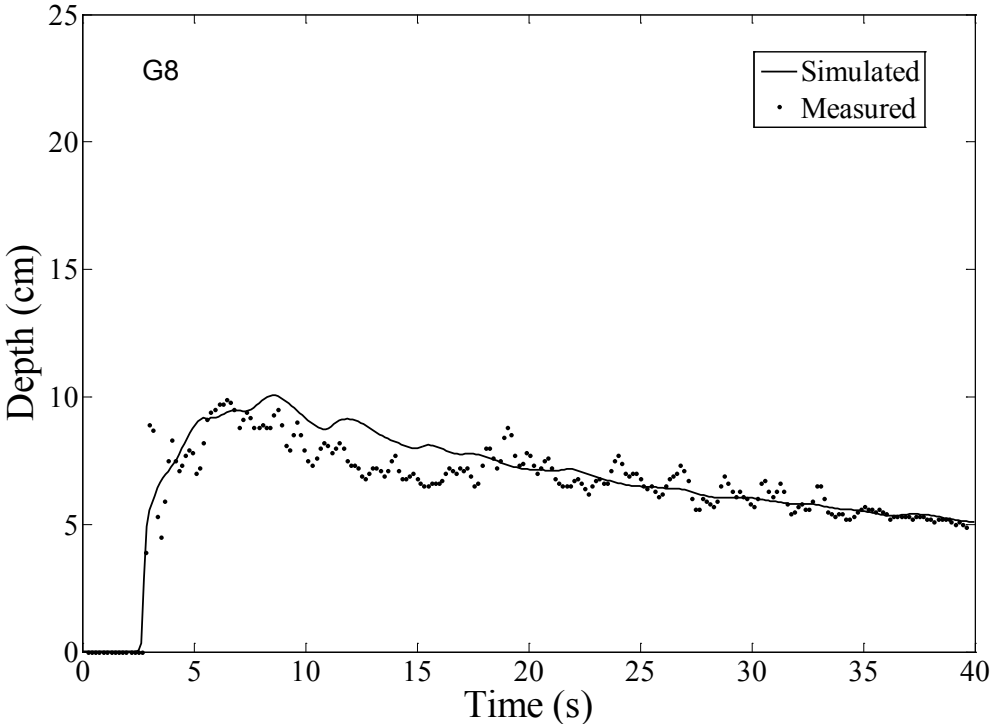

Figure 5.47 Comparison of simulated and measured hydrographs at G8

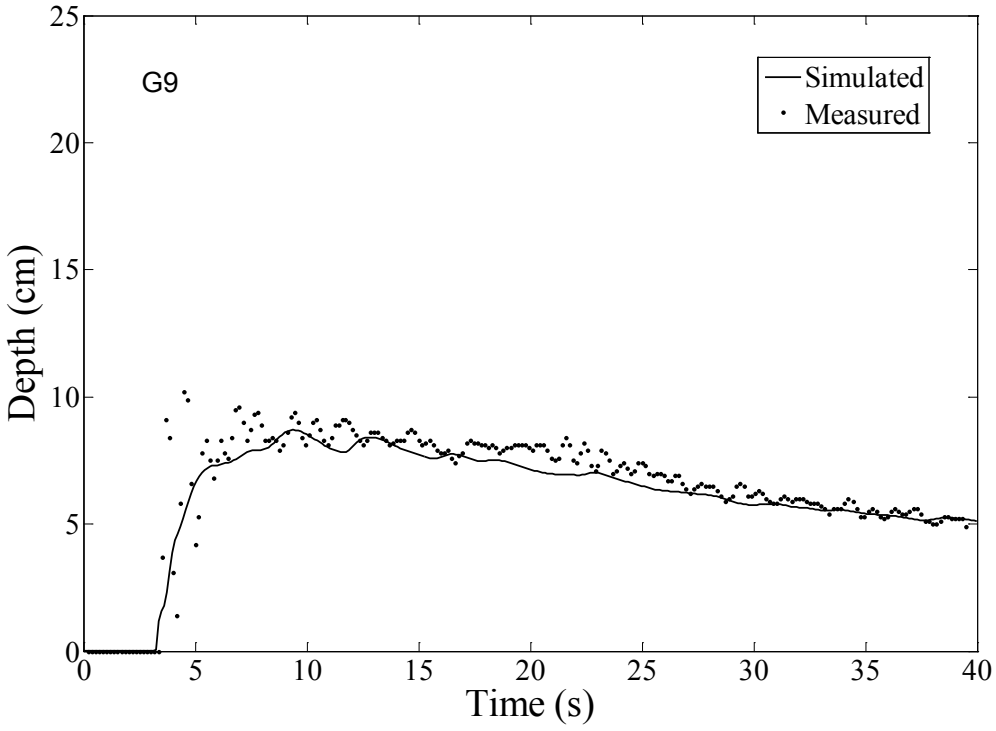

Figure 5.48 Comparison of simulated and measured hydrographs at G9

5.8 Dam-break in a channel with 90° bend

The shape of the horizontal channel with 90° bend is shown in Figure 5.49 and gauge points location at Table 5.2. The dam is represented by a gate at the outlet of the reservoir. The initial water level in the upstream reservoir is 0.2 m above the horizontal channel bed, and the channel downstream is dry. The Manning's roughness coefficients of 0.0095 $s/m^{1/3}$ for bottom friction and 0.0195 $s/m^{1/3}$ for wall friction are adopted as suggested (Soares Frazão and Zech 2002). The computational domain is triangulated with 8546 elements. The dry bed depth of 0.0001 m and time step of 0.002 s are used.

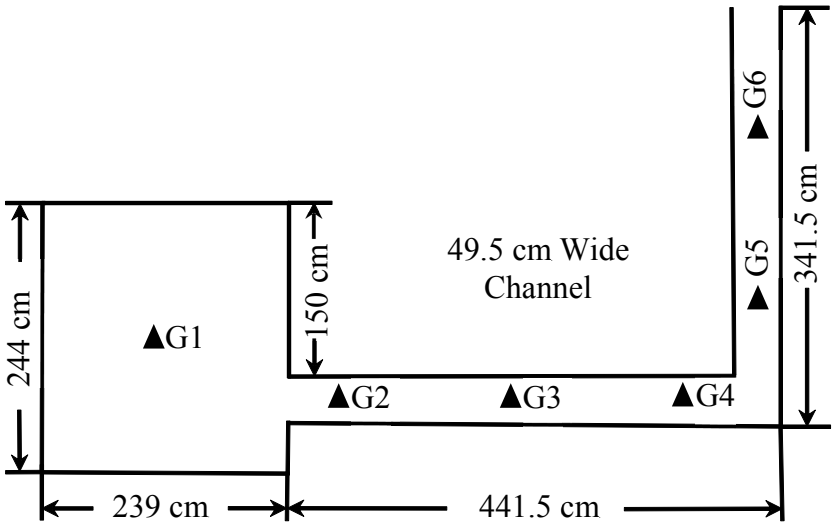

Figure 5.49 Plan view of channel with 90° bend

Table 5.2 Gauge point locations in 90^0 bend

Gauge Point	G1	G2	G3	G4	G5	G6
***x* (m)**	1.19	2.74	4.24	5.74	6.56	6.56
***y* (m)**	1.20	0.69	0.69	0.69	1.51	3.01

After the removal of the gate, water flows rapidly into the channel and reaches the bend. The water reflects against the wall and a shock forms and moves upstream. The simulated hydrographs at six gauging points are compared with measured data in Figures 5.50 – 5.55. Numerical results are in good agreement with the measured data. The arrival time of the flood wave and reflected bore are well predicted except at G2, where the simulated bore arrival time is too early. Overall, the simulated results give satisfactory performance.

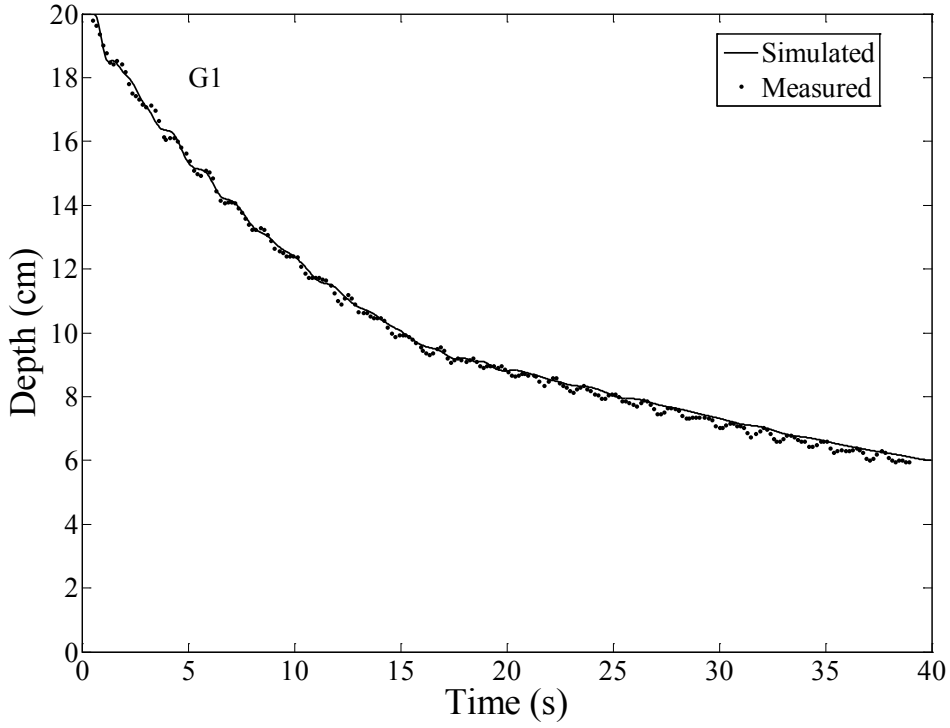

Figure 5.50 Comparison of simulated and measured hydrograph at G1

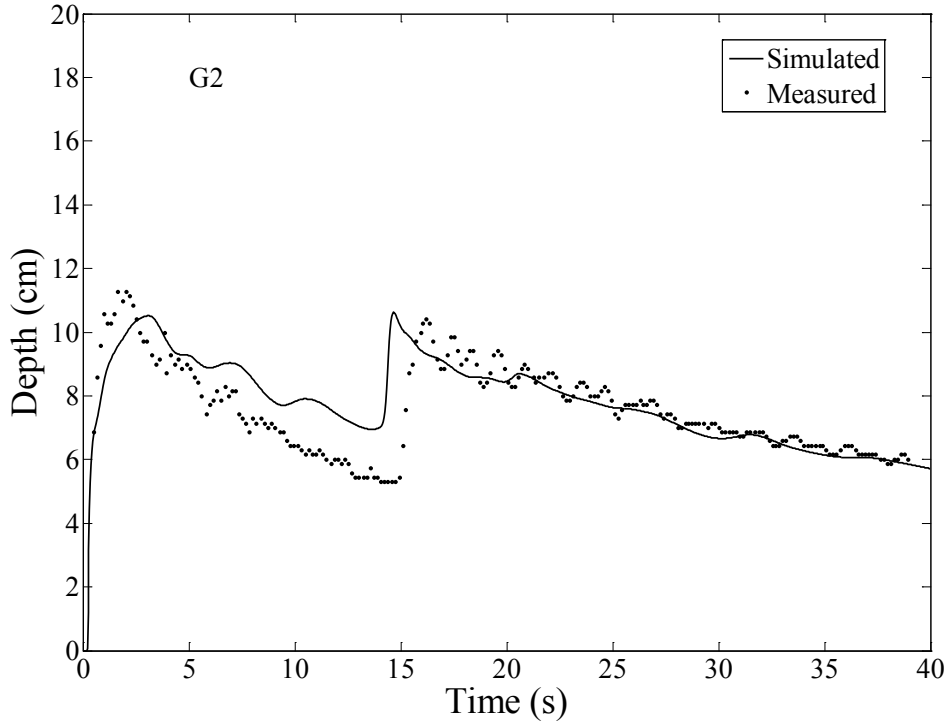

Figure 5.51 Comparison of simulated and measured hydrograph at G2

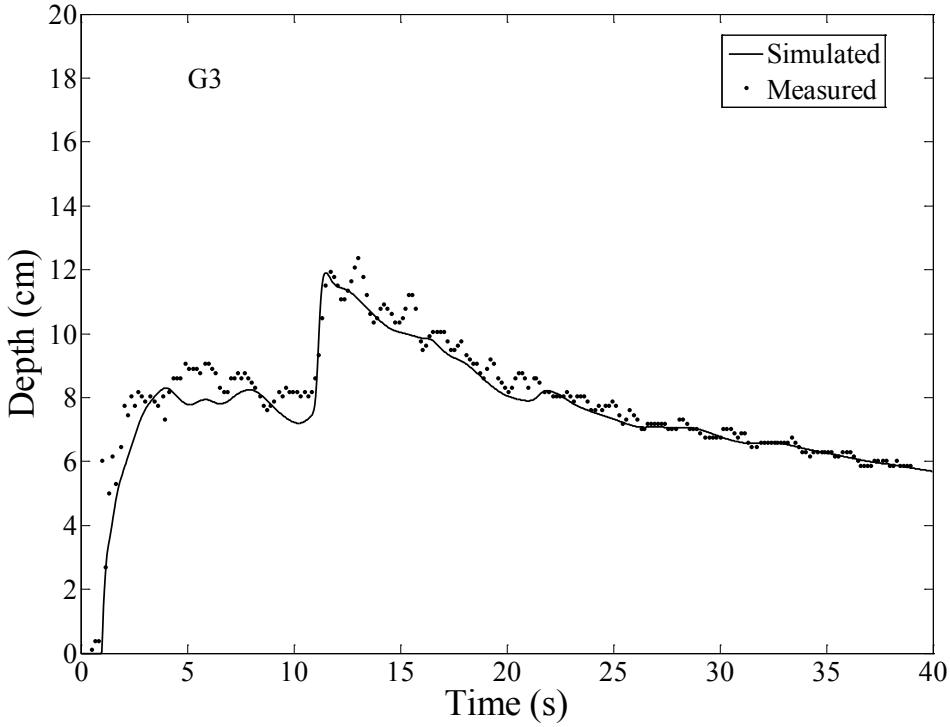

Figure 5.52 Comparison of simulated and measured hydrograph at G3

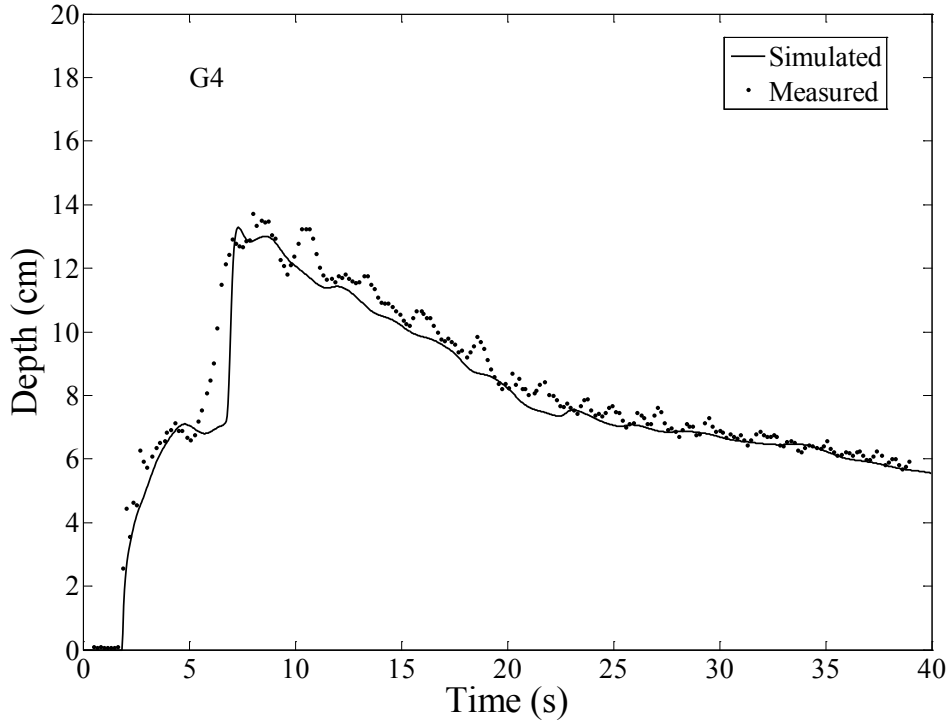

Figure 5.53 Comparison of simulated and measured hydrograph at G4

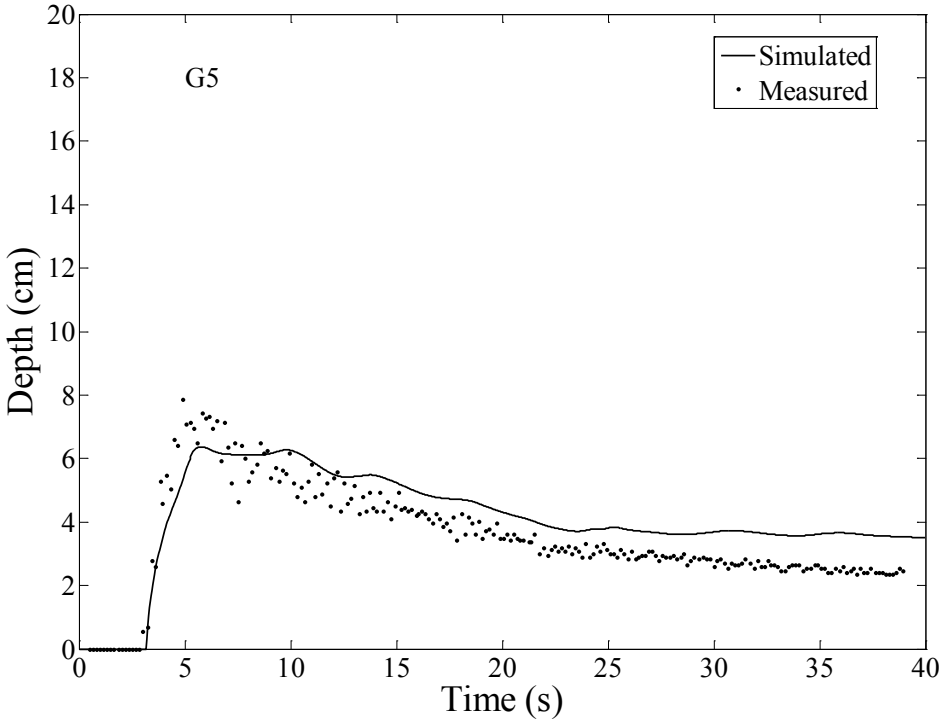

Figure 5.54 Comparison of simulated and measured hydrograph at G5

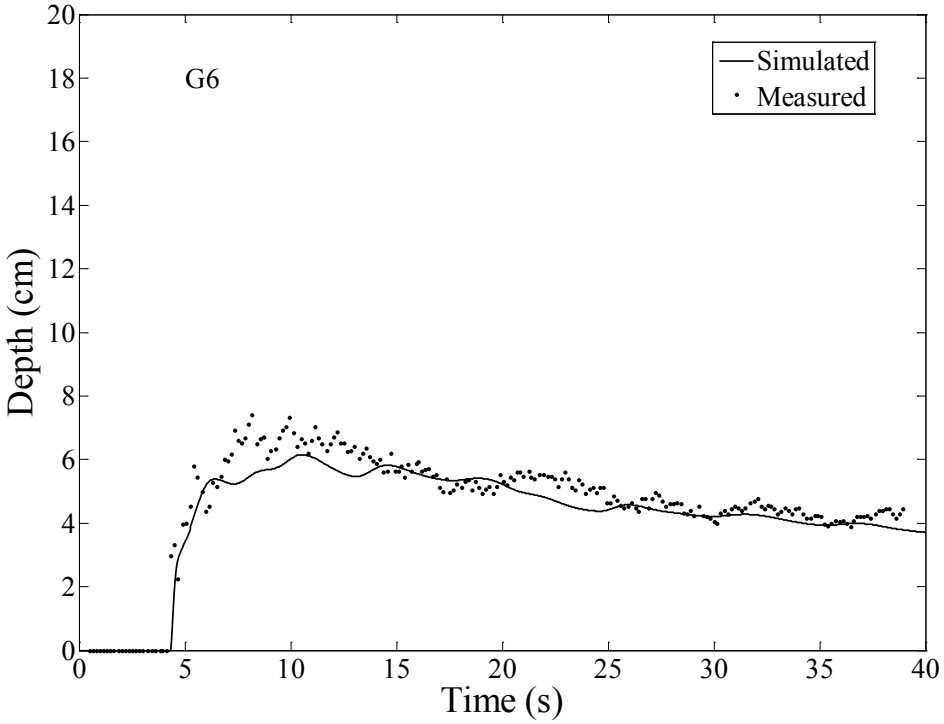

Figure 5.55 Comparison of simulated and measured hydrograph at G6

5.9 Dam-break flow over a triangular bump

In this test, the numerical scheme is used to model dam-break flow over a triangular bump (Hiver, 1997) as proposed by the CADAM project. Numerical results are compared with experimental data obtained from Laboratoire de Recherches Hydrauliques, Châtelet (Belgium). The rectangular channel is 38 m long, 0.75 m wide with a gate located at 15.5 m from upstream end. The symmetric triangular bump (6 m long, 0.4 m high) is situated at 13 m downstream of the gate. The initial condition and bed bottom is shown in Figure 5.56. Water depth upstream of the gate is 0.75 m with dry bed downstream. The Manning's roughness coefficients are 0.0125 and 0.011, respectively, for bed and the walls as suggested (Hiver, 1997). Free outflow boundary condition is applied at the outflow end. The computational domain is triangulated with 4352 elements. The dry bed depth of 0.001 m and time step of 0.006 s are used. Simulated and measured hydrograph at 90 seconds after the dam removal at gauge points G2, G4, G8, G10, G11, G13 and G20 are shown in Figure 5.57-5.63. Gauge points denote distance from the gate, for example, G2 is located 2 m downstream of the gate. The simulated results are in good agreement with the measured data. The flood wave arrival time and water depth are well predicted at all gauge points. The wetting and drying effect at the critical point G13, which is located at the vertex of the bump, is modeled correctly. Difference between simulated and measured results at the last point G20 mostly comes from the uncertainty of the actual outflow boundary condition.

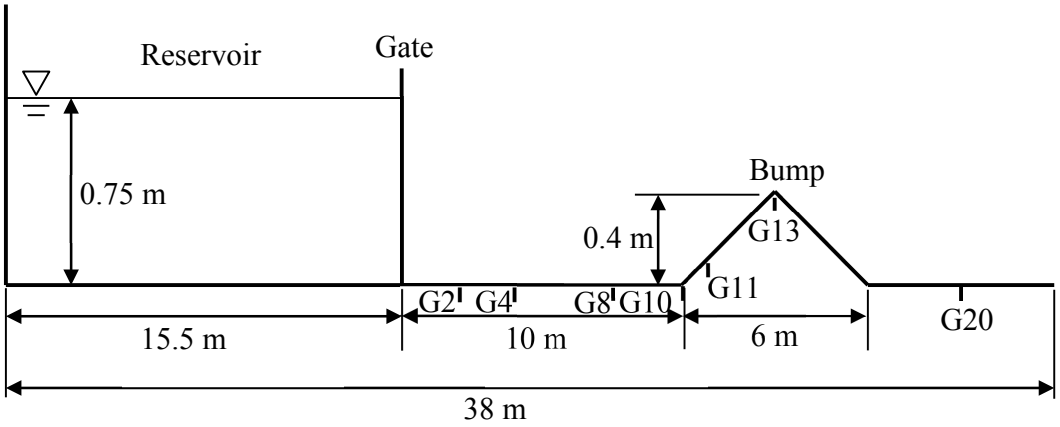

Figure 5.56 Geometry and experimental set up in the channel with triangular bump

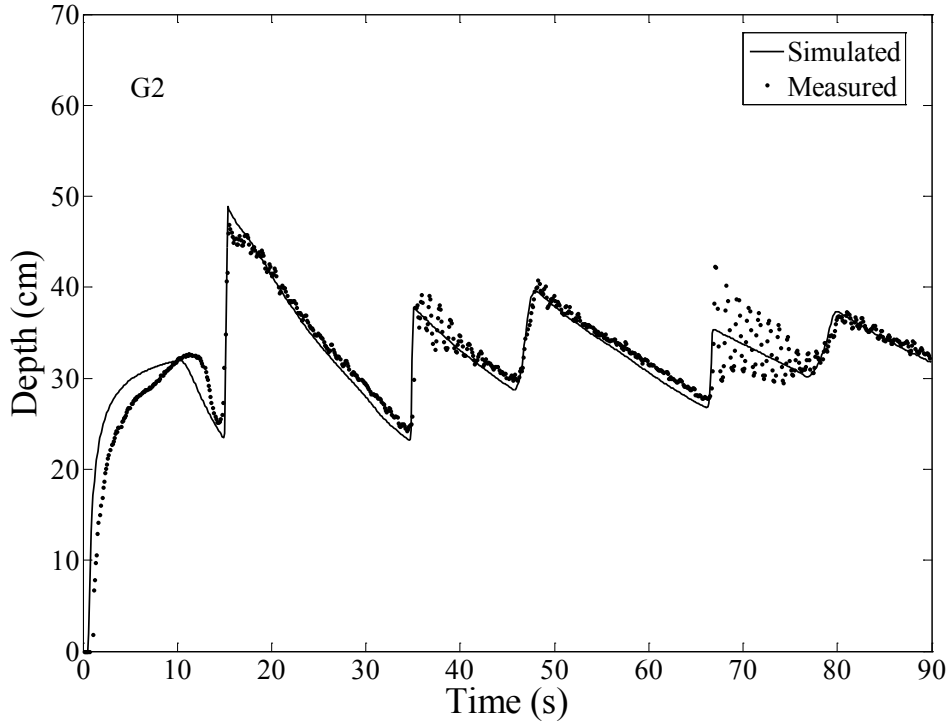

Figure 5.57 Simulated and measured hydrograph at gauge point G2

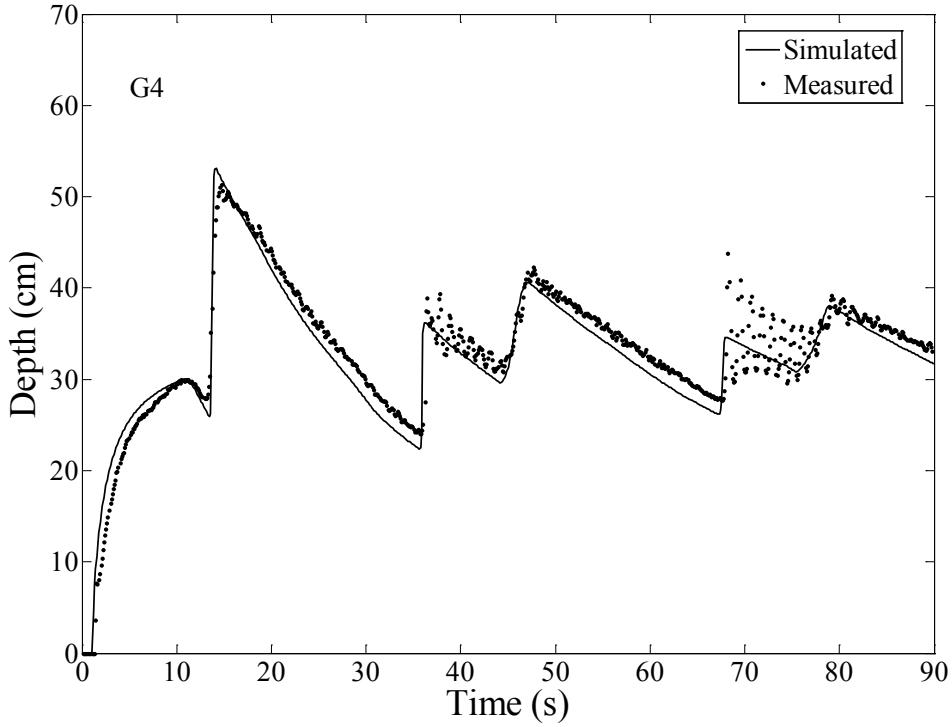

Figure 5.58 Simulated and measured hydrograph at gauge point G4

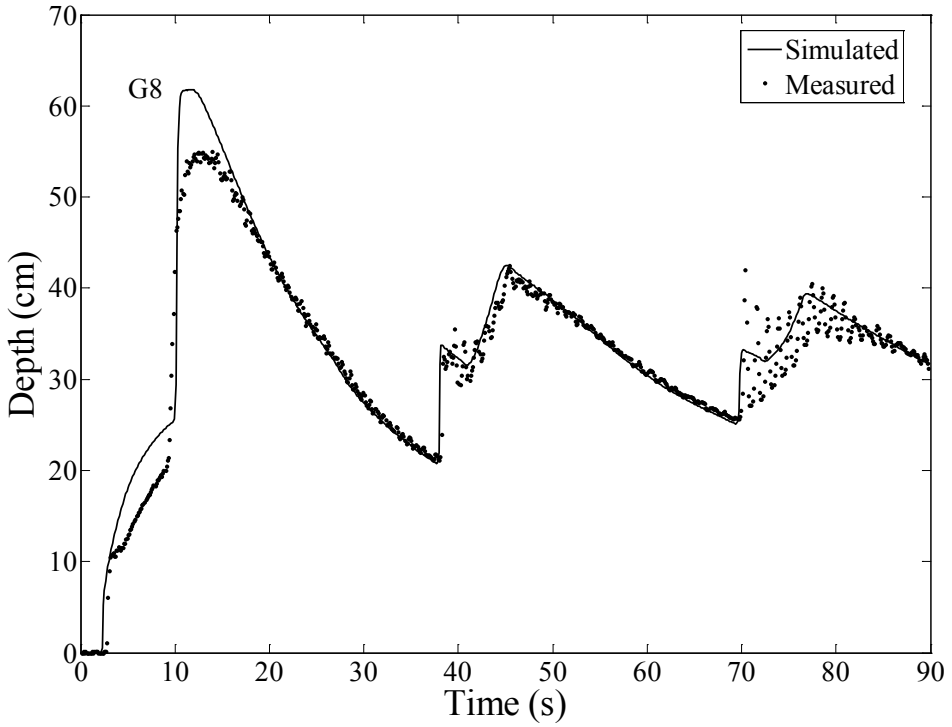

Figure 5.59 Simulated and measured hydrograph at gauge point G8

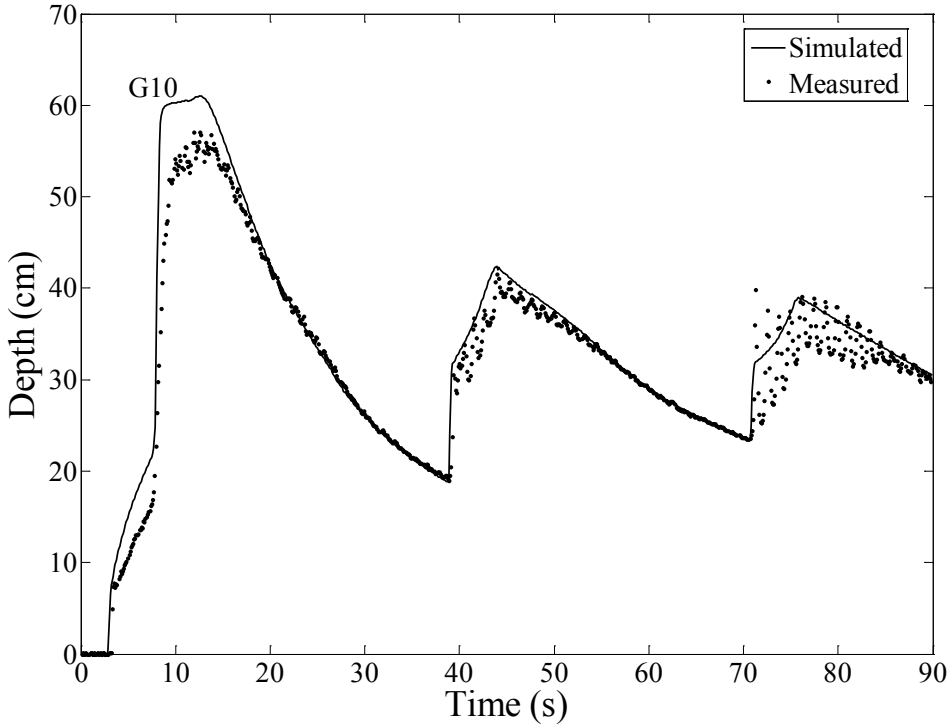

Figure 5.60 Simulated and measured hydrograph at gauge point G10

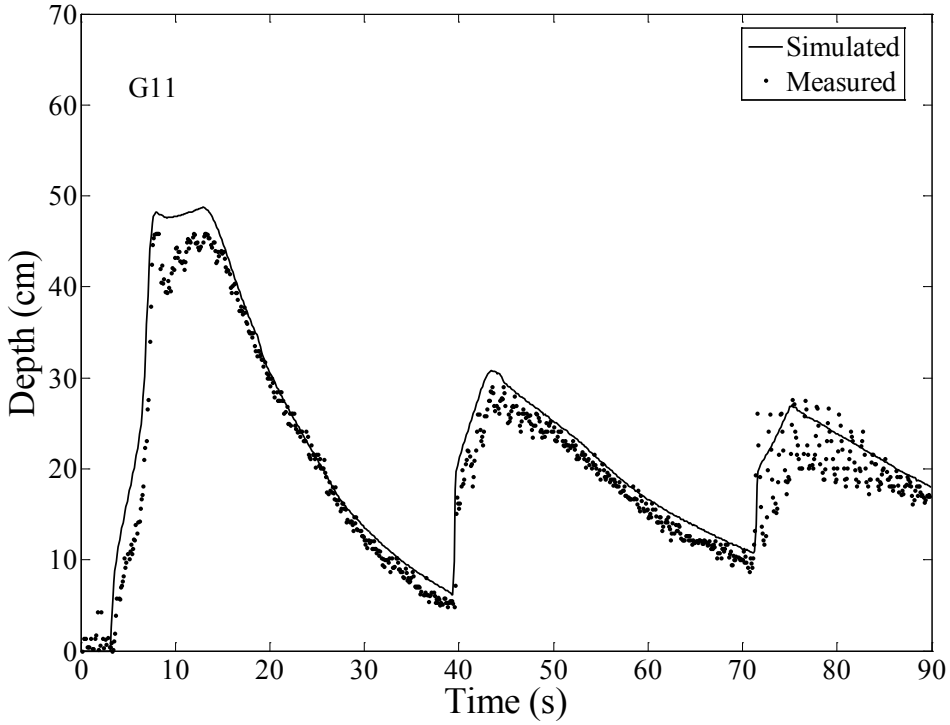

Figure 5.61 Simulated and measured hydrograph at gauge point G11

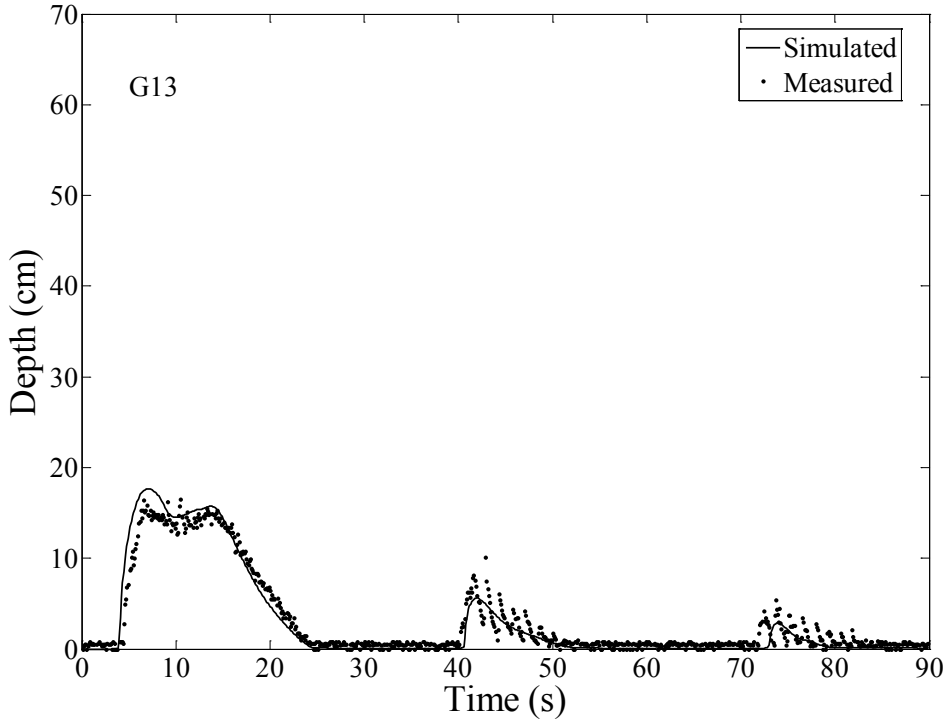

Figure 5.62 Simulated and measured hydrograph at gauge point G13

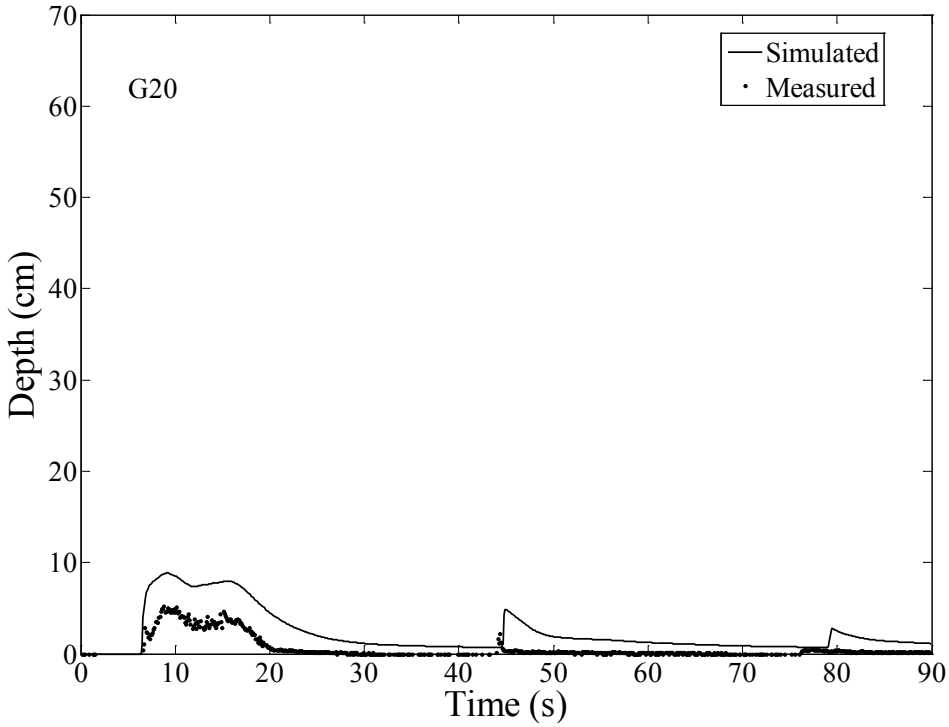

Figure 5.63 Simulated and measured hydrograph at gauge point G20

5.10 Stationarity test over bumps

The well-balanced property of the scheme is tested by simulating initial still water over a channel with three bumps (Kawahara and Umetsu, 1986) and constant water surface level. The channel is 75 m long and 30 m wide with closed wall, and channel bottom is defined as:

$$z_b(x,y) = \max\left[0, 1-\frac{1}{8}\sqrt{(x-30)^2+(y-6)^2}, 1-\frac{1}{8}\sqrt{(x-30)^2+(y-24)^2}, 1-\frac{3}{10}\sqrt{(x-47.5)^2+(y-15)^2}\right] \tag{5.7}$$

The water surface elevation is initially 0.5 m in the whole channel, covering partially the bumps. The domain is triangulated with 5006 elements. Time step of 0.01 s is used. Computed water surface at 100 s is shown in Figure 5.64, showing the stationarity state is well preserved.

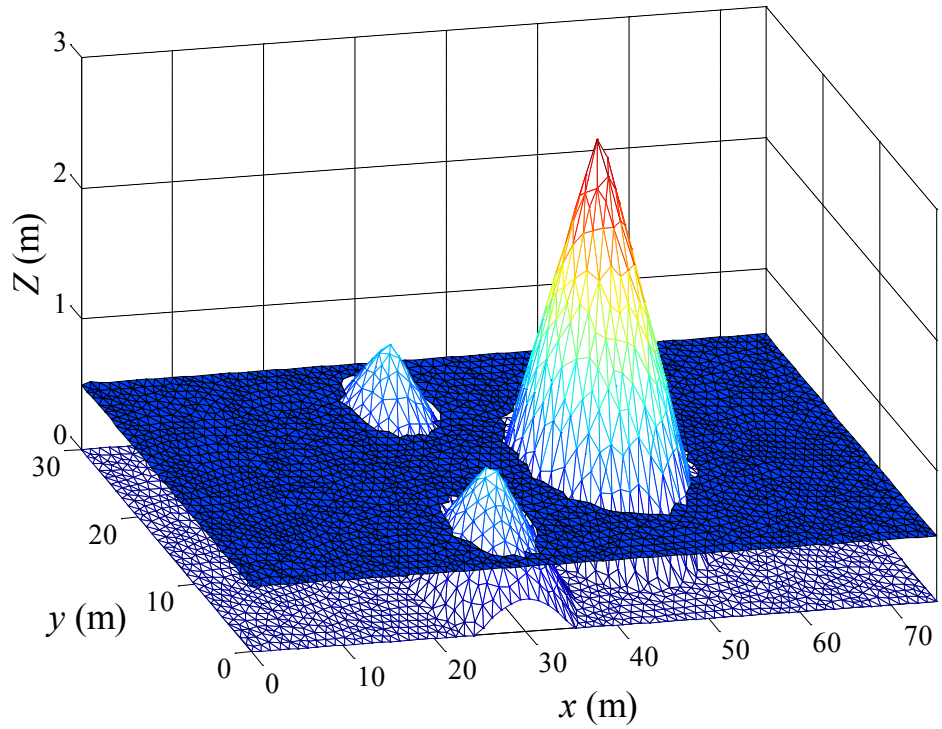

Figure 5.64 Water surface at 100 s for stationarity test with bumps

5.11 Dam-break flow over bumps

The channel with three bumps in the previous test is used in this test with different initial conditions as shown in Figure 5.65. The dam is located at 16 m and retains water to the depth of 1.875 m upstream, while the bed is dry downstream of the dam. The Manning's roughness coefficient is 0.018 $s/m^{1/3}$. The dam is assumed to be removed instantaneously, and the dam-break flow afterward is simulated. This test case has been used by other researchers to validate the flooding and drying treatment in their numerical schemes (Brufau et al., 2002; Liang and Borthwick, 2009). The dry bed depth criterion of 0.001 m and time step of 0.01 s are used. Numerical tests show that decrease in dry bed depth criterion requires decrease in time step to achieve stable results.

Numerical results of water surface at different times after the removal of the dam, are presented through Figures 5.66 – 5.70 to show the flood propagation and wetting and drying capability of the numerical scheme. At time 2 seconds, the flood wave reaches the two smaller bumps and begins to run up. At time 6 seconds, flood wave overtops the two smaller bumps and the water accumulates behind the highest bump. A reflective bore is moving upstream. At time 12 seconds, the floodwater passes the highest bump and begins to flood the lee side. The drying of the highest bump and the reflective bore moving further upstream is clear. At time 30 seconds, wave interaction between the bump and the downstream wall is shown. The steady state water surface at 300 second shows the peaks of the smaller bumps are no longer submerged. The flooding and drying effect on this complicated bed topography is properly simulated.

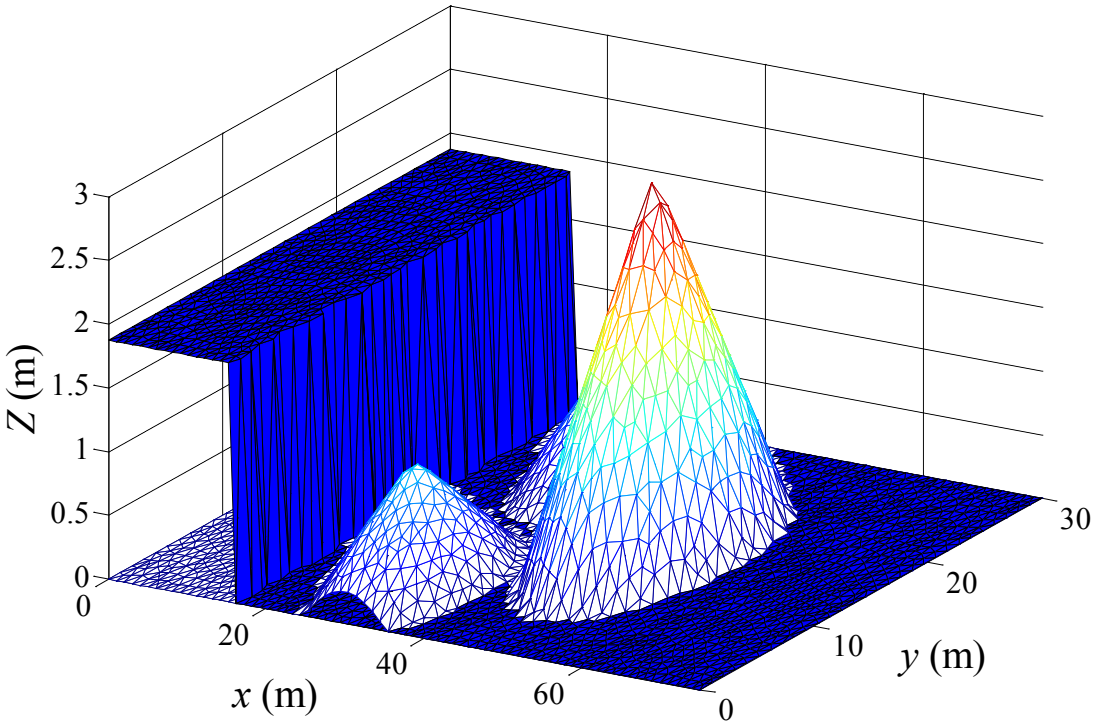

Figure 5.65 Initial condition of dam-break flow over three bumps

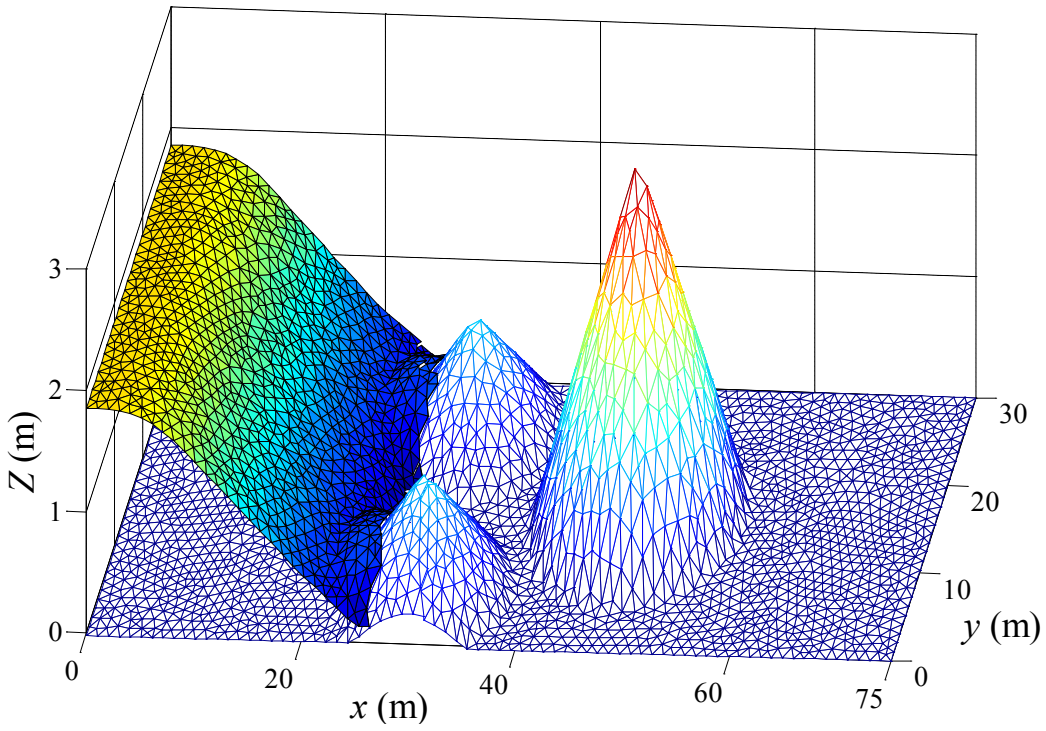

Figure 5.66 Water surface at 2 s for the dam-break flow with three bumps

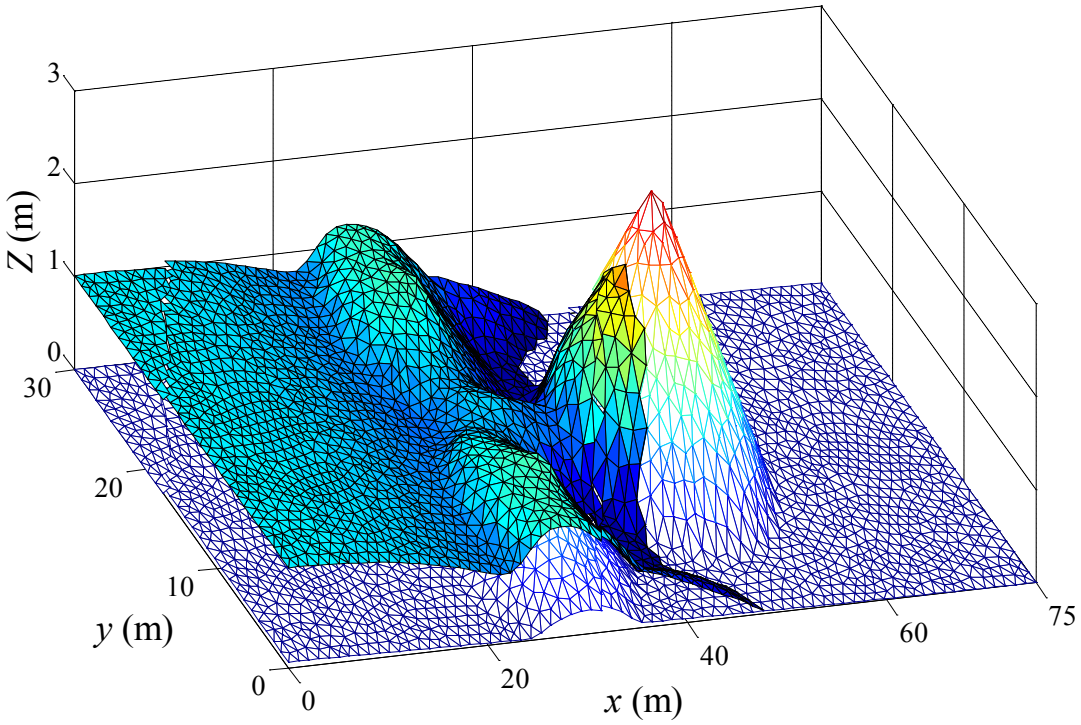

Figure 5.67 Water surface at 6 s for the dam-break flow with three bumps

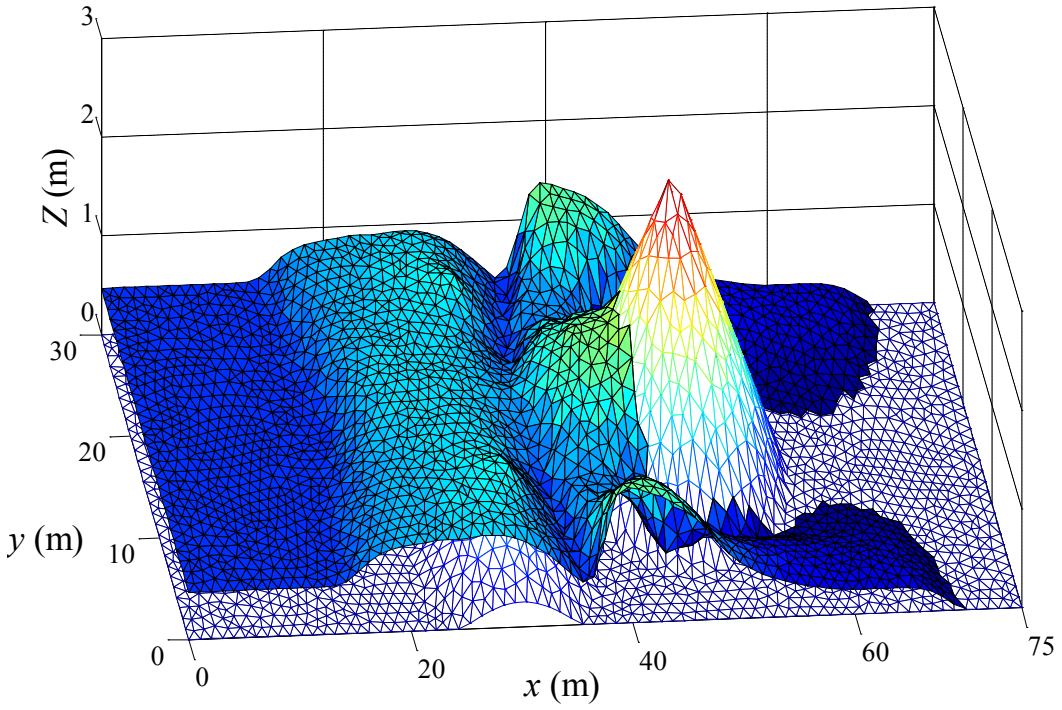

Figure 5.68 Water surface at 12 s for the dam-break flow with three bumps

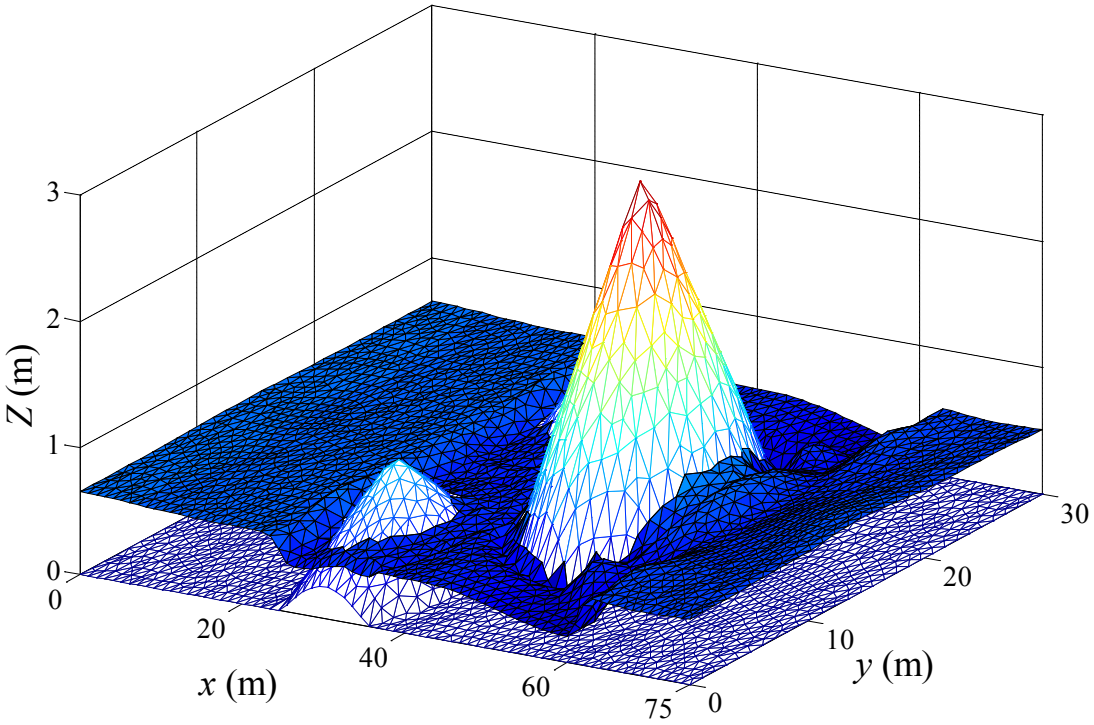

Figure 5.69 Water surface at 30 s for the dam-break flow with three bumps

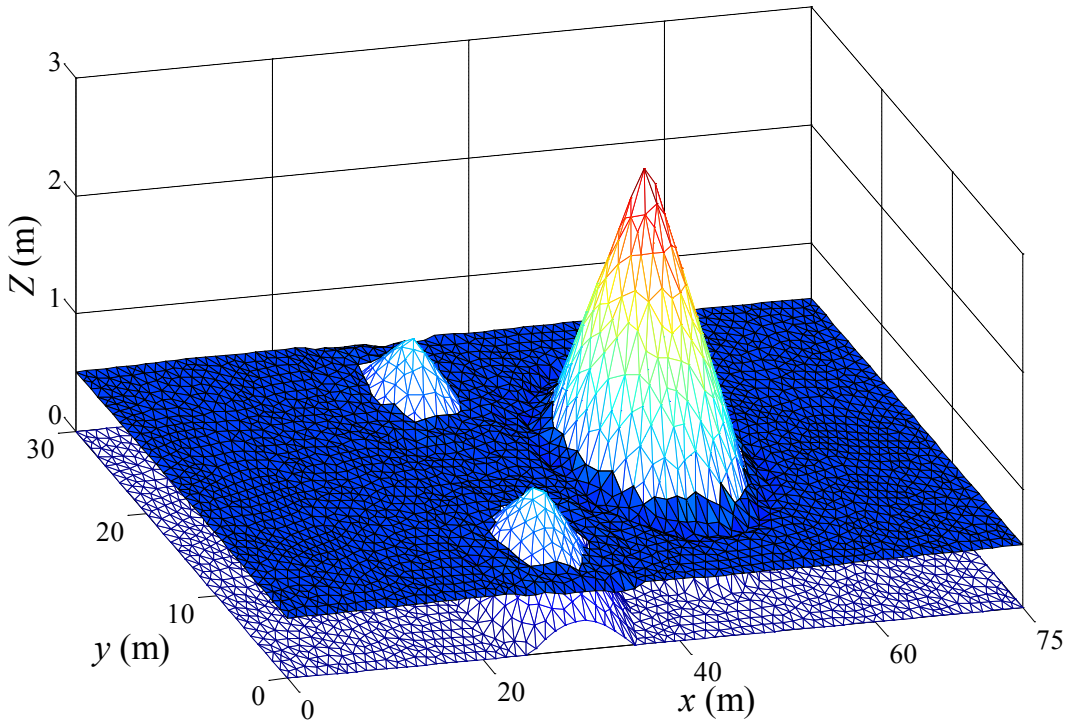

Figure 5.70 Water surface at 300 s for the dam-break flow with three bumps

5.12 The Toce River dam-break

A physical model at a scale of 1:100 of a reach of the Toce River valley (occidental Alps, Italy) was reproduced at the ENEL-HYDRO Laboratory in Milan. Dam-break tests in the physical model were used in the CADAM project (Soares Frazão and Testa, 1999). Modeling parameters such as topographic data, inflow hydrograph, and Manning's coefficient were specified by Electricité de France (EDF). The value of Manning's roughness coefficient was suggested as 0.0162 $s/m^{1/3}$.

The topography of Toce River physical model is shown in Figure 5.71. The physical model approximately covered an area of $50\,\mathrm{m} \times 12\,\mathrm{m}$. The riverbed was initially dry. A rectangular tank was located at the upstream end of the physical model. Two different test cases were conducted in the physical model, one corresponding to the overtopping of the reservoir in the middle of the river and one without overtopping. Inflow hydrographs at the rectangular tank is used as inflow boundary condition for numerical simulations in this study. Critical inflow and outflow boundary conditions are applied in the computation as described in the physical model study. The domain is discretized using 13316 elements. The inflow hydrograph corresponding to overtopping (HY2) and without overtopping (HY1) at the upstream end of the physical model are shown in Figure 5.72.

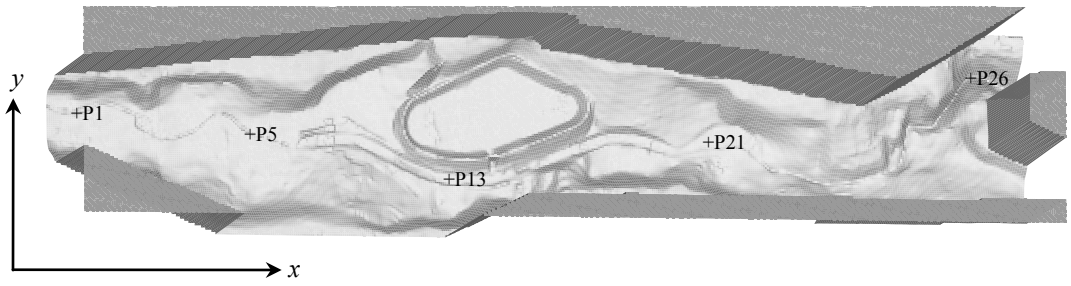

Figure 5.71 3D view of the Toce River topography

Table 5.3 Gauge point locations in Toce River

Gauge Point	P1	P5	P13	P21	P26
***x* (m)**	2.917	11.264	20.879	33.115	45.794
***y* (m)**	6.895	6.083	4.130	6.090	9.437

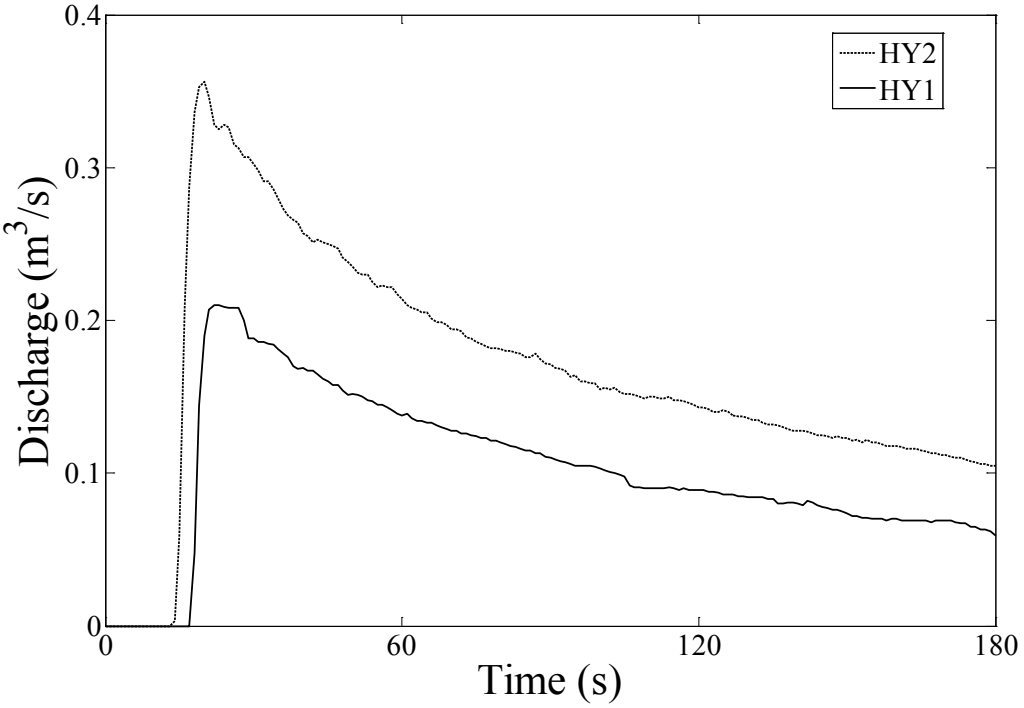

Figure 5.72 Inflow conditions at the river upstream boundary

Water depth and flooded area at time 30, 45, and 60 seconds are shown in Figures 5.73 – 5.78 for both test cases. Results show that the flood flow path is well predicted along the channel. In addition, reflections and deflections due to irregular boundaries and bed geography are handled accurately. Computed stage hydrographs at five gauge points are shown in Figure 5.79 and Figure 5.80 along with the measured data. Coordinates of the gauge points are shown in Table 5.3. Computed results are in good agreement with measured data in terms of magnitude and arrival time of the wave at these gauge points. There is a discrepancy between computed and measured flood arrival time at P26, mainly because the buildings and bridges at the downstream end are not considered in the simulation. This test shows that the numerical scheme is capable of modeling extreme flood events in natural rivers.

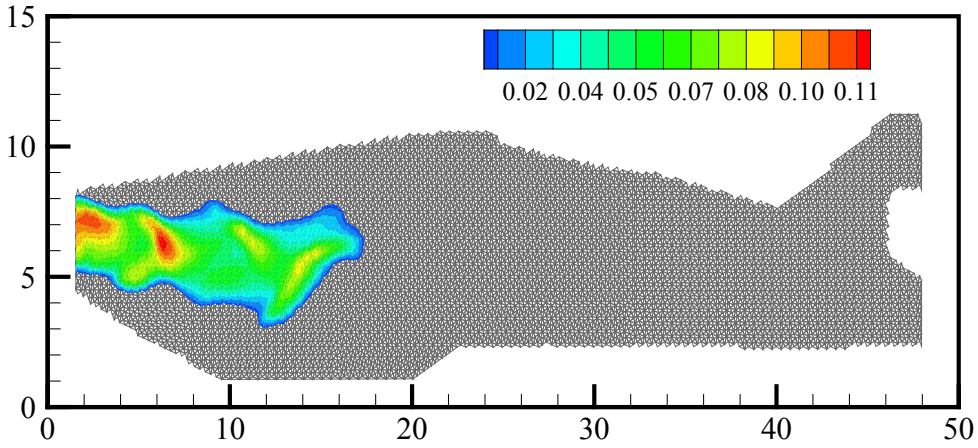

Figure 5.73 Water depth at *t*=30s for Toce dam-break test without overtopping

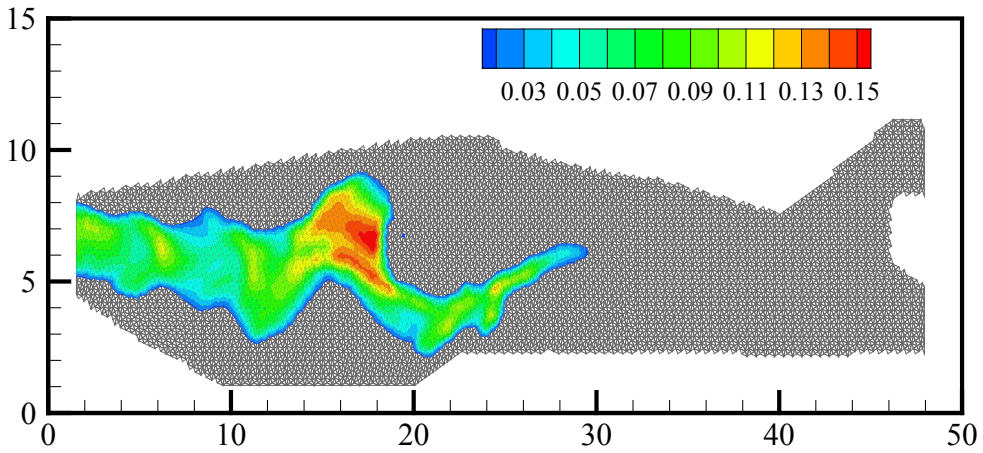

Figure 5.74 Water depth at *t*=45s for Toce dam-break test without overtopping

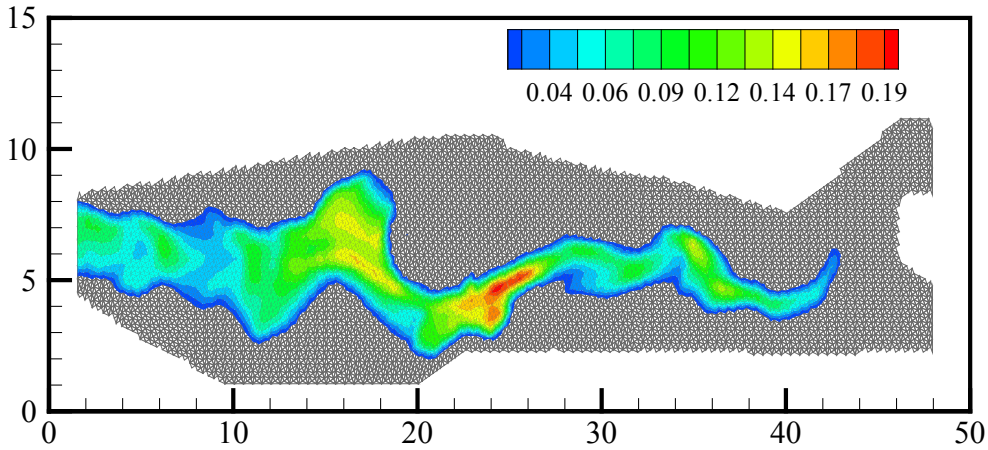

Figure 5.75 Water depth at *t*=60s for Toce dam-break test without overtopping

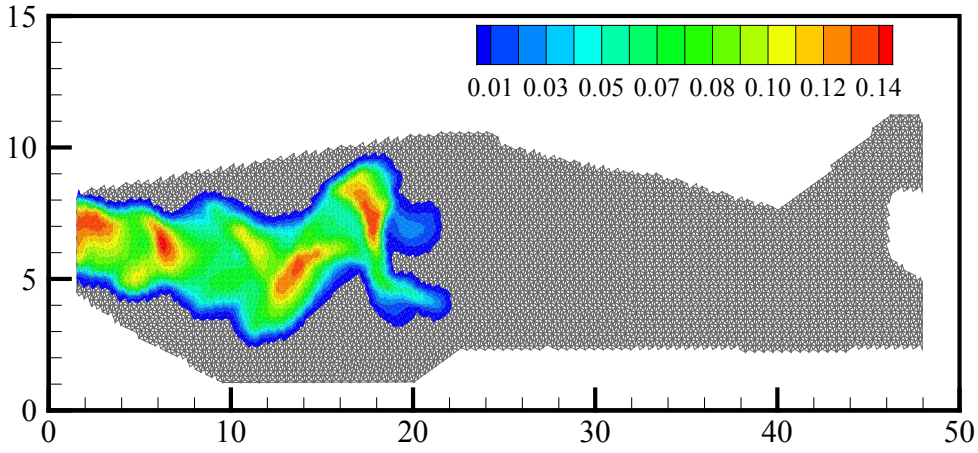

Figure 5.76 Water depth at t=30s for Toce dam-break test with overtopping

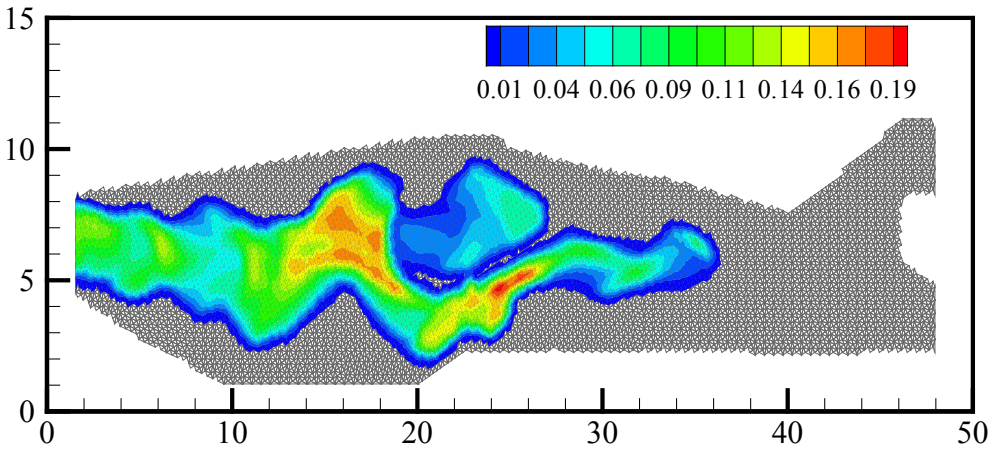

Figure 5.77 Water depth at t=45s for Toce dam-break test with overtopping

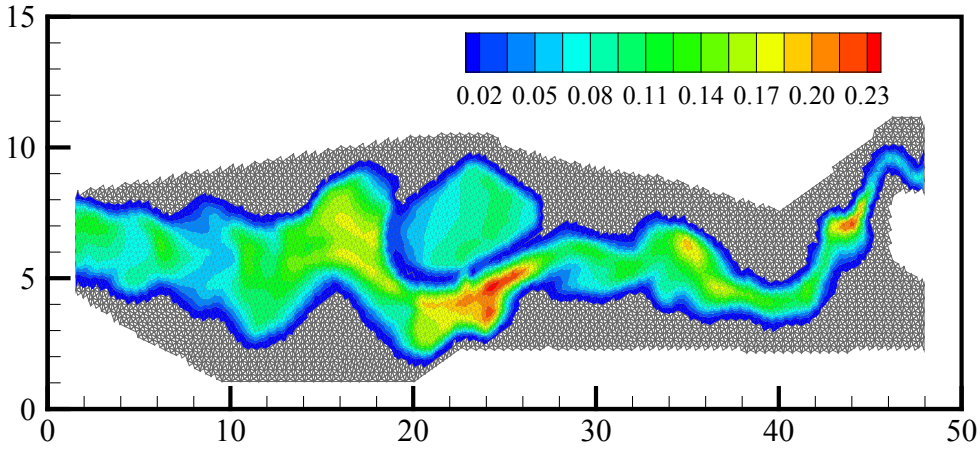

Figure 5.78 Water depth at t=60s for Toce dam-break test with overtopping

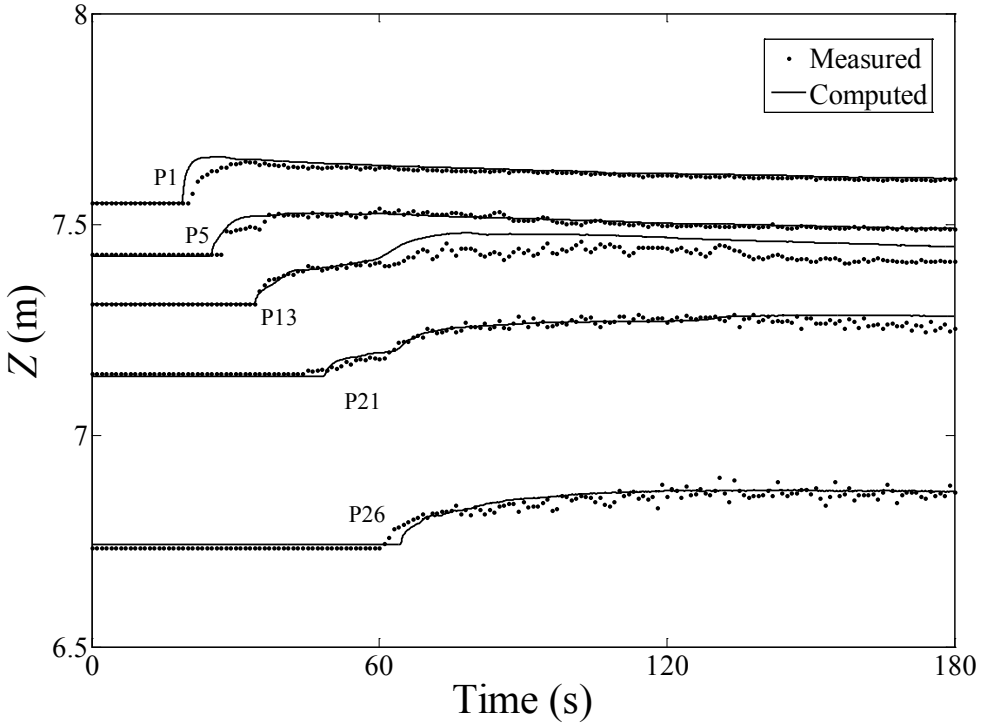

Figure 5.79 Computed stage hydrographs without overtopping

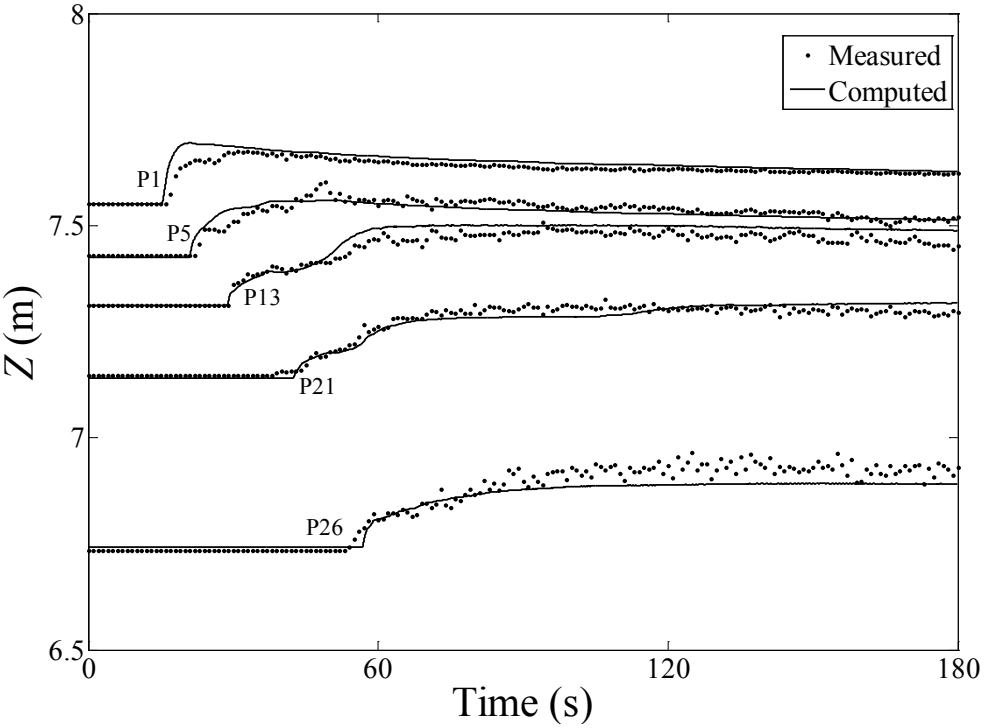

Figure 5.80 Computed stage hydrographs with overtopping

5.13 Paute River dam-break event

In this test, the numerical scheme is used to model a dam-break flood in Paute River, Ecuador. In 1993, a landslide created a natural dam, which blocked the flow and created a reservoir upstream of Paute River. Due to high water level in the reservoir, the dam was subsequently overtopped and caused a dam-break type flood. River topography and triangulation data are available from BreZo (Sanders and Begnudelli, 2010). The dam-break case is used to test the numerical scheme's ability to handle flow in natural rivers with complex geometry and sharp bends, though field data are not available. The computational mesh with 74224 elements and initial water depth are shown in Figure 5.81 (units in meter). The dam is considered as a straight line between (x, y) coordinates of (739602 m, 9684690 m) and (739616 m, 9684530 m), and separates upstream and downstream region. The initial upstream water level is 2362 m above sea level and downstream bed is dry. The bed elevations range from 2155.2 m to 2917.8 m above sea level. The Manning's roughness coefficient is set to be 0.033 in the domain. The dam is assumed to be removed completely and instantaneously. The dam-break flood afterward is simulated. The dry bed depth criterion of 0.04 m and time step size of 0.01 s are used. The computed water depth contour (flood inundation map) at 10 min, 20 min, and 40 min after the dam-break are presented in Figures 5.82-5.84. The numerical results are similar to results reported by Song et al. (2011). The flood wave travels about 6000 m in the first 10 min, then encounters a sharp bend and travels about 6000 m during 20-40 min. Numerical results show the scheme is able to model flow in natural rivers with wet/dry bed conditions and sharp bends.

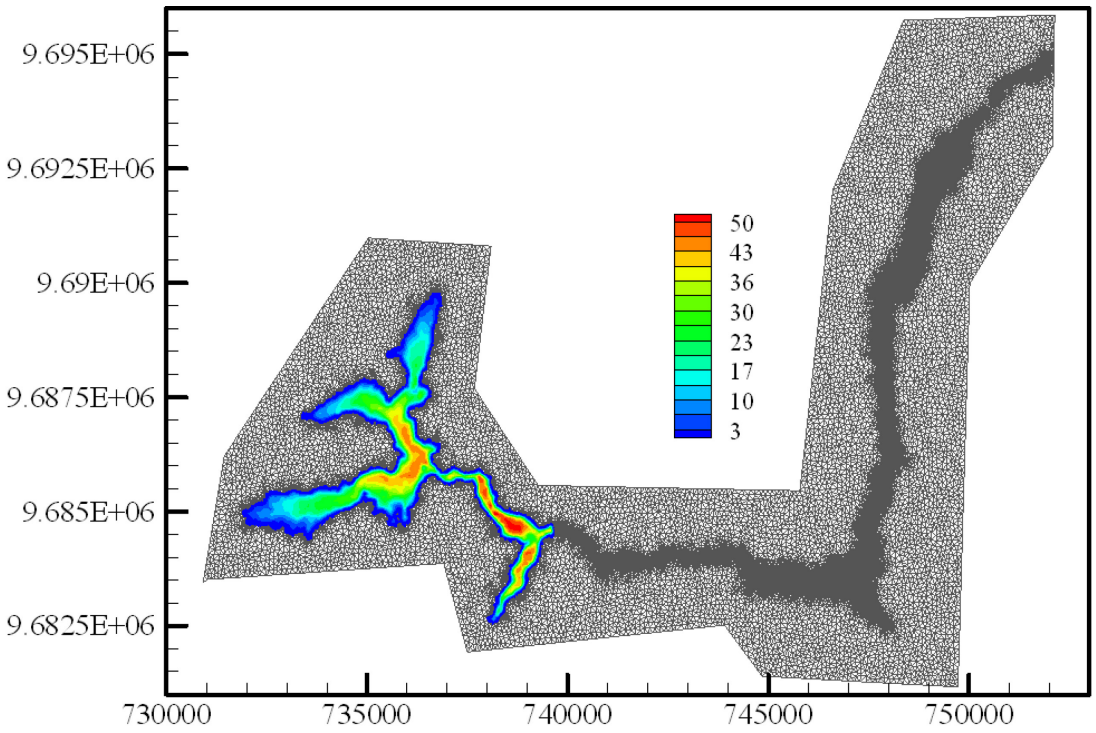

Figure 5.81 Initial water depth contour for Paute River dam-break test

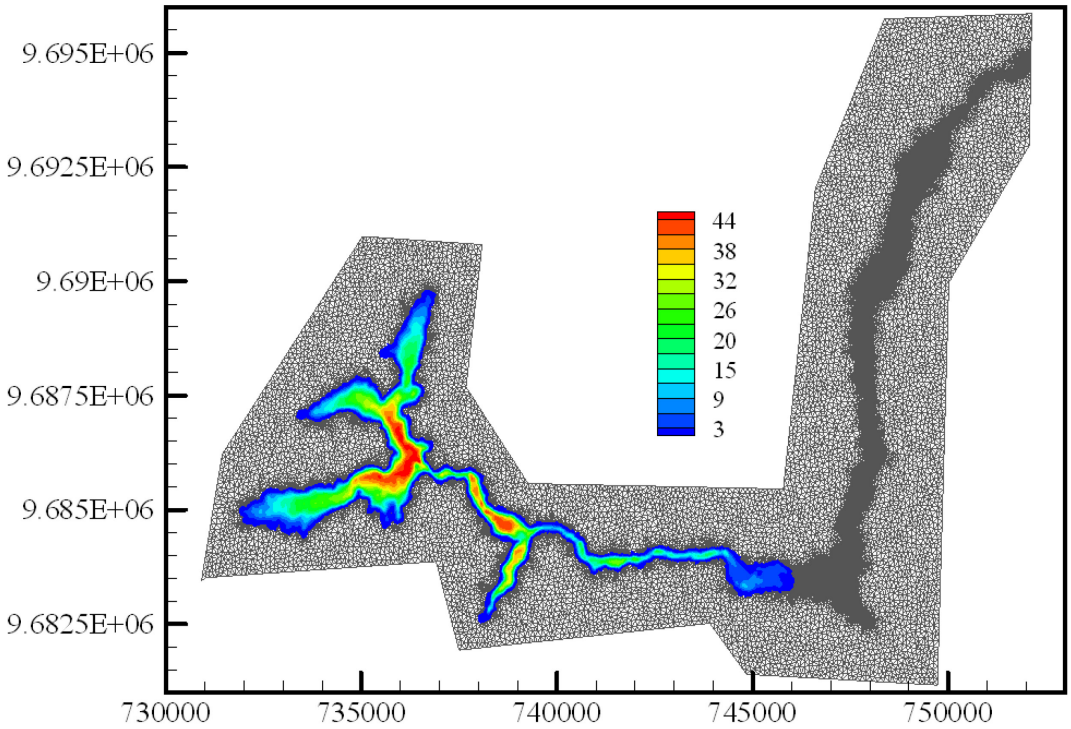

Figure 5.82 Computed water depth contour for Paute River dam-break test at t=10 min

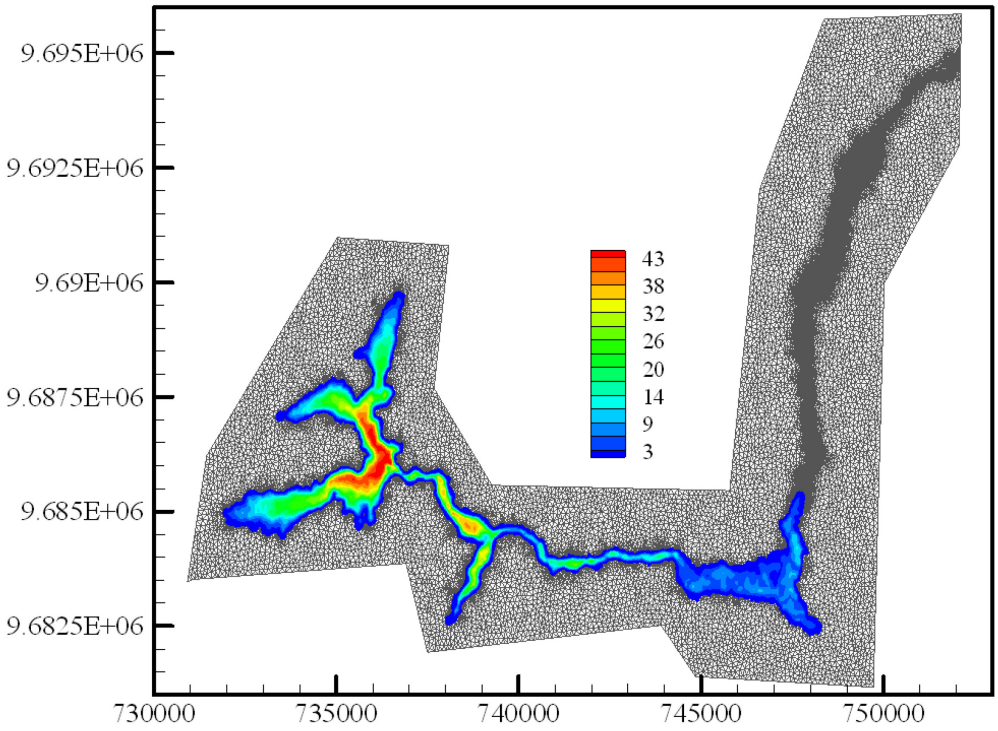

Figure 5.83 Computed water depth contour for Paute River dam-break test at *t*=20 min

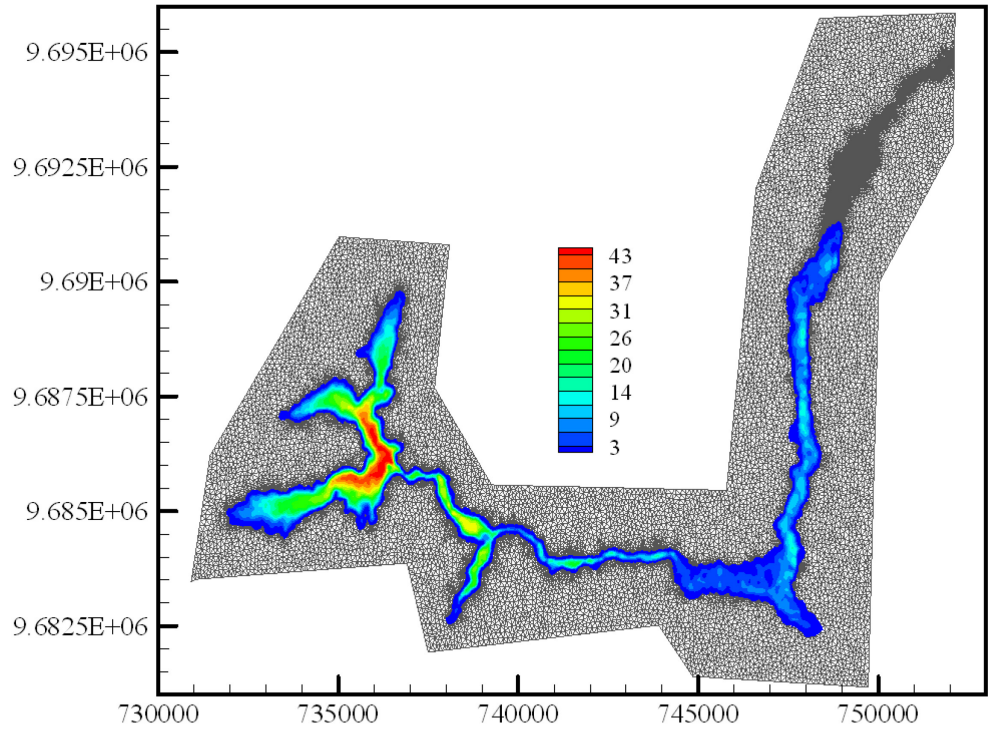

Figure 5.84 Computed water depth contour for Paute River dam-break test at *t*=40 min

5.14 Malpasset dam-break event

The Malpasset dam was located in a narrow gorge of the Reyran River Valley in France. The dam was 66.5 m high with variable thickness and the upper crest had an elevation of 223 m, and formed a reservoir with capacity of 55×10^6 m^3. In 1959, the dam failed due to intense rainfall and rapid increase of water level in the reservoir. The maximum water levels along the Reyran River Valley after the dam failure were obtained from a police survey (these points are denoted P1-P17). In 1964, a physical model with a scale of 1:400 was built by Laboratoire National d'Hydraulique to study the dam-break flow. The maximum water level and flood wave arrival time were recorded at 9 points in the physical model (these points are denoted S6-S14).

Due to the availability of the measured data and complex bottom topography, the Malpasset dam-break event was adopted as a benchmark test for CADAM projects (Goutal, 1999). This event is simulated to validate the numerical model. The computational domain with 26000 elements and measured points are shown in Figure 5.85. The domain covers an area approximate of 17500 m × 9000 m. The bed elevations range from -20 m below sea level to 100 m above sea level. The Reyran River has two sharp narrow bends immediately downstream of the dam and eventually reaches the coastal floodplain.

The dam is considered as a straight line between (x, y) coordinates of (4701.18 m, 4143.41 m) and (4656.5 m, 4392.1 m). The initial water level inside the reservoir is set to 100 m above sea level, and the computational domain downstream of the dam is considered as dry bed. The initial discharge in the Reyran River before dam failure is

neglected because of the relatively huge amount of flow caused by the dam failure. The model is simulated until the water reaches the sea, so no boundary condition is applied at the downstream end. The Manning's roughness coefficient is estimated to be in the range of 0.025-0.033 $s/m^{1/3}$, equivalent to a Strickler coefficient in the range of 30-40 $m^{1/3}/s$ as suggested by EDF (Hervouet and Petitiean, 1999). The dry bed depth of 0.02 m and time step size of 0.01 s are used.

The computed and measured flood arrival time at gauges (S6-S14) are shown in Figure 5.86. The computed and measured maximum water level at gauges and surveyed points (P1-P17) are presented in Figure 5.87 and Figure 5.88, respectively. The effect of Manning's roughness coefficient is investigated; simulated results using uniform value of 0.025 and 0.033 in the entire computational domain are compared with the measured data. Lower roughness (0.025, solid line) corresponds to a faster moving front (Figure 5.86) and lower water levels (Figures 5.87-5.88). A roughness coefficient of 0.029 gives the best estimation. The maximum water level is relatively insensitive to different roughness coefficients. The computed results for both flood arrival time and maximum water levels are generally in good agreement with the field data.

The water depth contour (flood inundation map) at 800 s, 1800 s, and 2400 s with roughness coefficient of 0.029 are presented in Figures 5.89 – 5.91 (units in meter). The flood wave propagation and inundation area are well modeled with high mountains at downstream floodplain. The results show that the present scheme is capable of dealing with dam-break flows over wet/dry bed with complex topography.

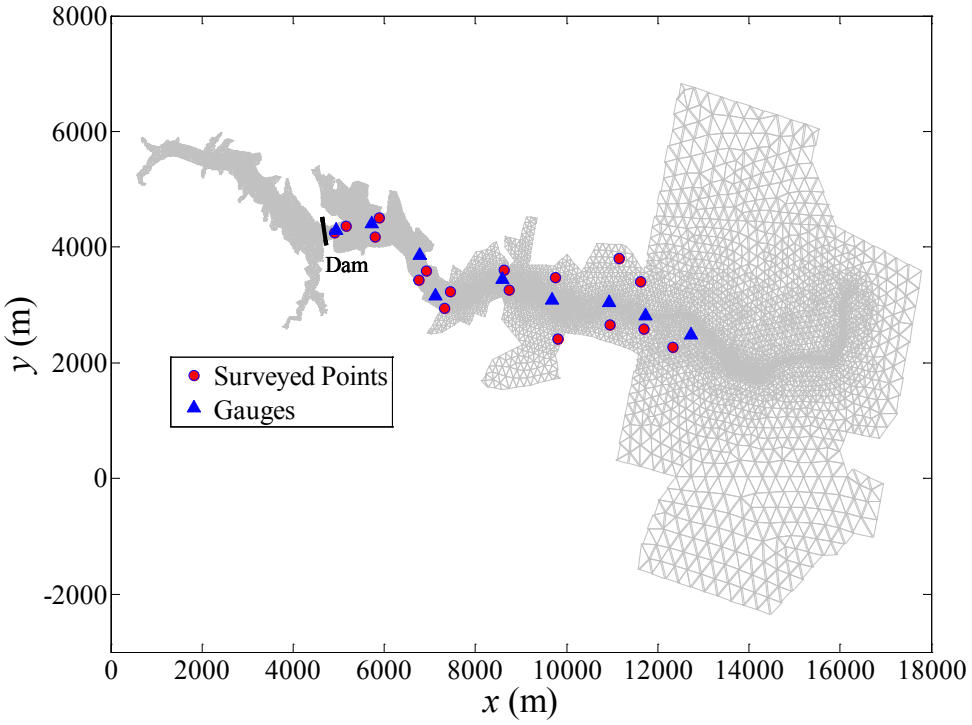

Figure 5.85 Mesh and locations of surveyed points and gauges

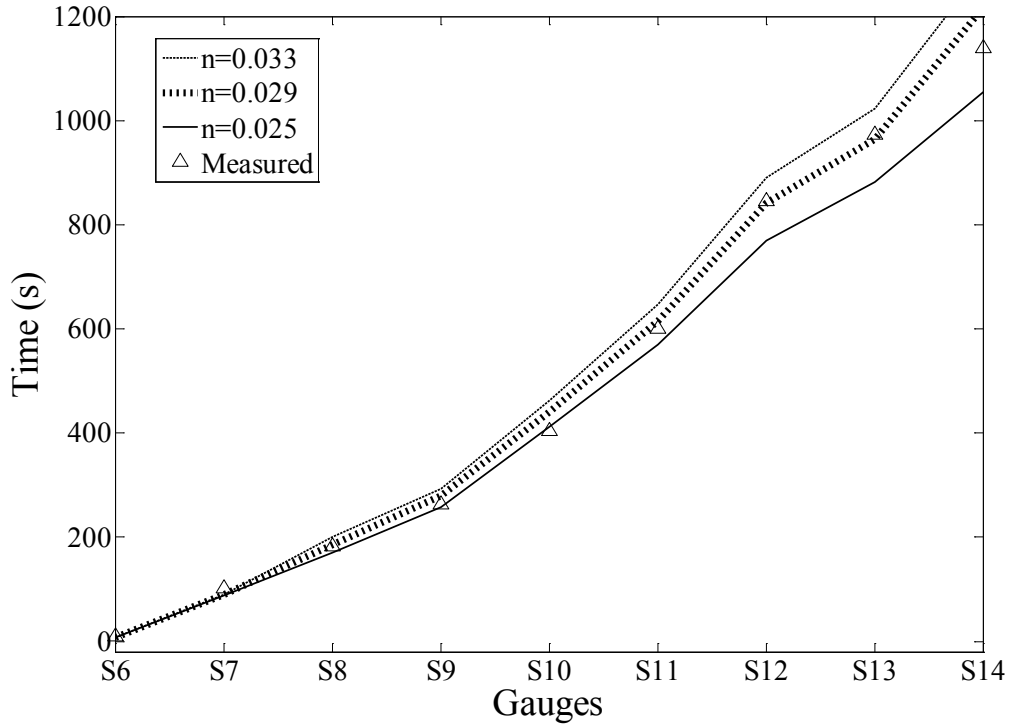

Figure 5.86 Comparison of computed and measured wave front arrival time

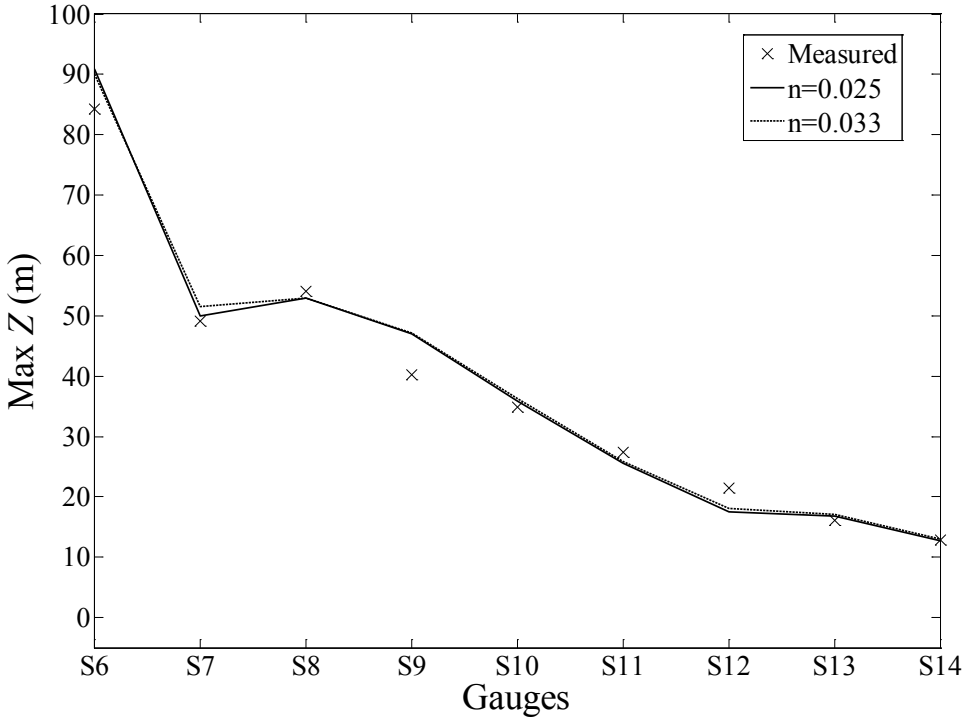

Figure 5.87 Comparison of computed and measured maximum water levels at gauges

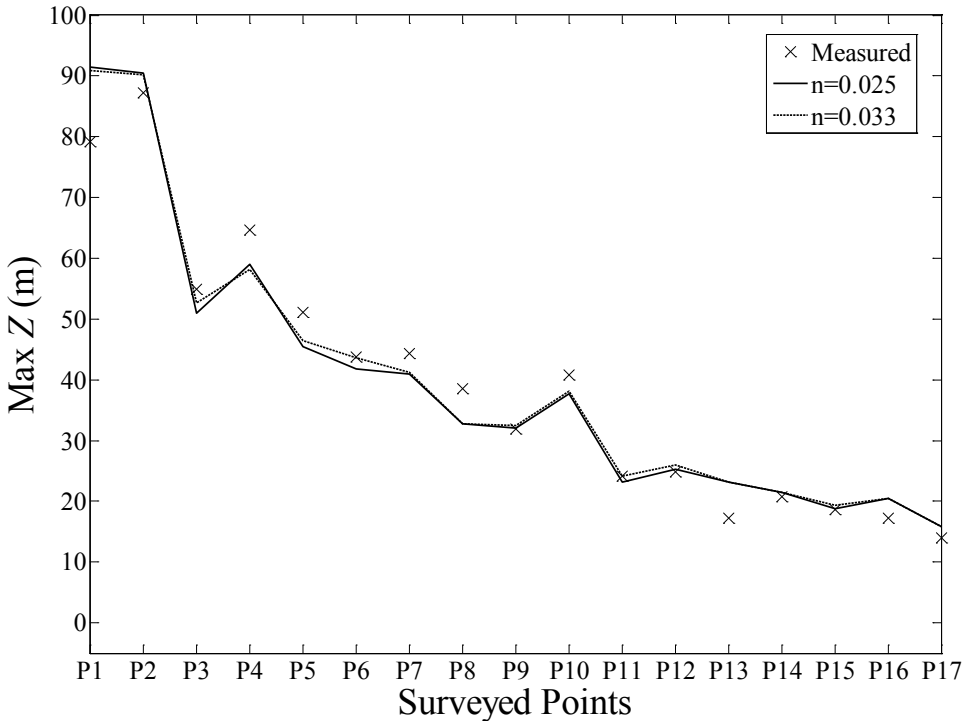

Figure 5.88 Computed and measured maximum water level at surveyed points

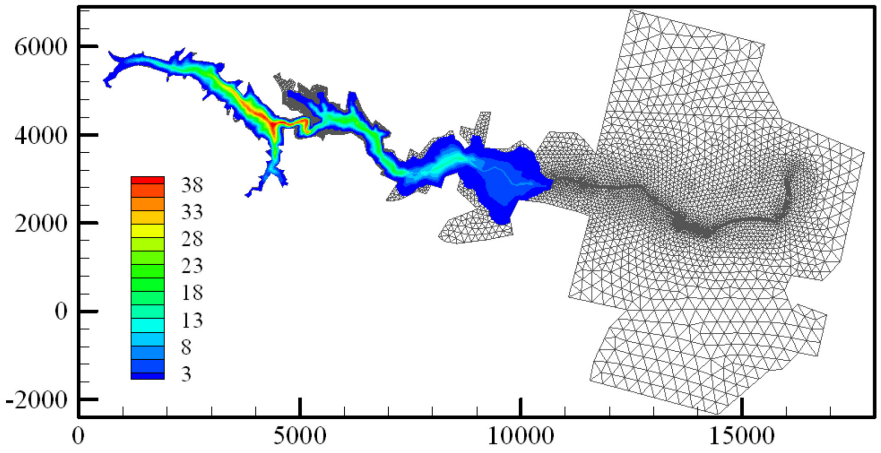

Figure 5.89 Computed water depth contour for Malpasset dam-break test at t=800 s

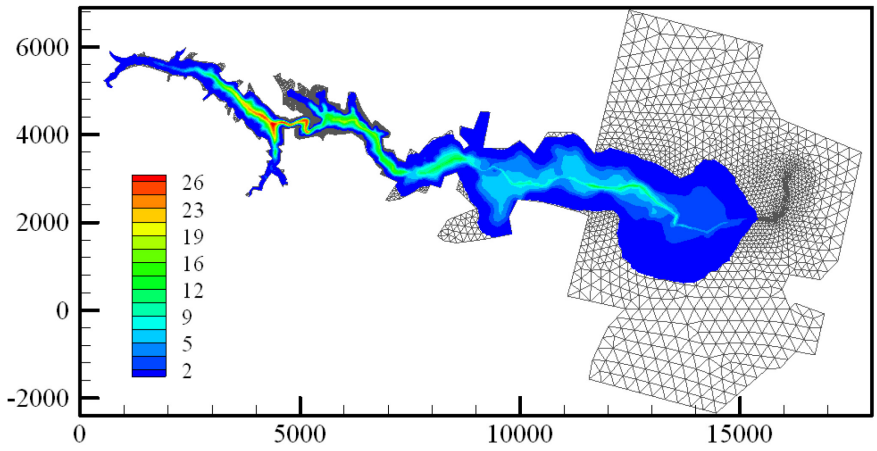

Figure 5.90 Computed water depth contour for Malpasset dam-break test at t=1800 s

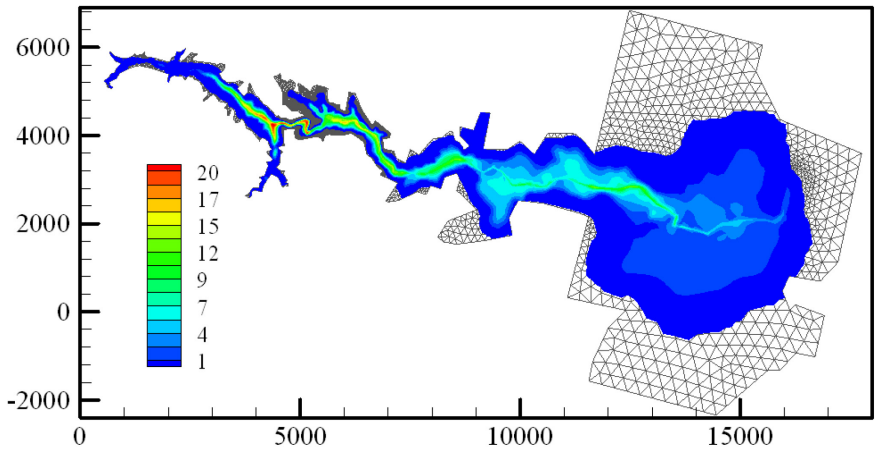

Figure 5.91 Computed water depth contour for Malpasset dam-break test at t=2400 s

CHAPTER SIX

CONCLUSIONS

Numerical models for one- and two-dimensional shallow water flows have been developed using the discontinuous Galerkin finite element method. A number of numerical tests, which including idealized dam-break problems, hydraulic jump, shock wave, wetting/drying problems, and flow in natural rivers, have been performed to validate these numerical models. Numerical results show that these models are simple, robust, accurate, and efficient to simulate shallow water flows under different flow regimes with complex channel geometry.

Governing equations for shallow water flows in one and two dimensions and their properties are discussed. Modified form of the shallow water equations are chosen in the numerical models. In the one-dimensional case, the hydrostatic pressure term and wall pressure term are combined into the water surface gradient term in the momentum equation. The resulting momentum equation circumvents the calculation of integral terms. In addition, it would not generate unphysical oscillations due to improper treatment of bed slope term. Similar to the one-dimensional case, the hydrostatic pressure term and the bed slope term is also combined into the water surface gradient term in the two-dimensional momentum equations. Discretization for the combined terms in both one- and two-dimensional cases are proposed. These formulations preserve the well-balanced property for initially still water problems with wet domain.

To achieve the well-balanced property in partially dry/wet problems, the source term is set to zero in both partially wet elements and dry elements. In addition, the slope limiter is not applied in elements with zero velocities. Although the source term in partially wet elements is forced to be zero, numerical tests show that the flood waves are still accurately modeled.

To provide the shock-capturing property in the numerical models, the approximate Riemann problem solvers, i.e., the Roe flux, HLL flux and HLLC flux, are employed to evaluate the intercell numerical flux. Even though different forms of the governing equations are adopted in the numerical models, it is found that the characteristic eigenvalues and eigenvectors should be used in the calculation of numerical flux. In the one-dimensional case, the effect and accuracy achieved by the Roe flux and HLL flux are compared. In the two-dimensional case, the HLLC is the complete Riemann solver for the three-wave system like the two-dimensional Saint-Venant equations.

Slope limiting procedures using the discontinuous Galerkin method for shallow water equations are presented. These slope limiters are oscillation-free even with shock wave. In the one-dimensional case, comparisons are made between slope limiter on cross-section, water surface elevation, and water depth. Numerical results show that the slope limiter on the conserved variables, cross-section area and flow rate, provides the most accurate scheme. For the two-dimensional shallow water flow equations, the slope limiter is modified and is applied to the conserved variables. The proposed slope limiter

is compared with the Superbee limiter. Numerical results show that the proposed limiter is more accurate and suitable for DG scheme.

Water flow over an initially dry bed is also simulated with the numerical models. Two types of dry bed treatment are compared in both one- and two-dimensional cases, one with sufficiently small depth defined at dry node, and one with zero depth at dry node with sufficiently small depth to track the wet/dry front. In one-dimensional tests, these two types of method give similar performance and accuracy. However, in two-dimensional tests, the second method with zero depth at dry node provides more accurate results in rivers with large bed variations. For horizontal beds, the two methods provide similar results.

The performances of the proposed numerical models are validated through extensive numerical tests. These tests include steady and unsteady flows, transcritical flow, wetting and drying effects, and flows in field-scale natural rivers with complex topography. Numerical results prove the effectiveness, robustness, and accuracy of the numerical models under different flow regimes with complex geometry. In conclusion, the proposed one- and two-dimensional numerical models for shallow water flows are useful tools for flow prediction and simulation.

In future, the models can be extended to incorporate Legendre polynomials as basis and test functions. The models can also be extended to incorporate pollutant and sediment transport. The method can be improved by utilizing higher order Riemann solver and slope limiters. Selective use of slope limiters based on the gradient of the conserved variables can be investigated.

REFERENCES

Aizinger, V., and Dawaon, C. (2002). "A discontinuous Galerkin method for two-dimensional flow and transport in shallow water." Advances in Water Resources, 25(1), 67-84.

Alcrudo, F., and Garcia-Navarro, P. (1993). "A high resolution Godunov-type scheme in finite volumes for the 2D shallow-water equations." International Journal for Numerical Methods in Fluids, 16(6), 489-505.

Anastasiou, K., and Chan, C. T. (1997). "Solution of the 2D shallow water equations using the finite volume method on unstructured triangular meshes." International Journal for Numerical Methods in Fluids, 24(11), 1225-1245.

Bellos, C., Soulis, V., and Sakkas, J. (1992). "Experimental investigation of two-dimensional dam-break induced flows." Journal of Hydraulic Research, 30(1), 47-63.

Bokhove, O. (2005). "Flooding and drying in discontinuous Galerkin finite-element discretizations of shallow-water equations. Part 1: One dimension." Journal of Scientific Computing, 22-23(1-3), 47-82.

Brufau, P., Vázquez-Cendón, M. E., and García-Navarro, P. (2002). "A numerical model for the flooding and drying of irregular domains." International Journal for Numerical Methods in Fluids, 39(3), 247-275.

Bunya, S., Kubatko, E. J., Westerink, J. J., and Dawson, C. (2009). "A wetting and drying treatment for the Runge-Kutta discontinuous Galerkin solution to the shallow water equations." Computer Methods in Applied Mechanics and Engineering, 198(17-20), 1548-1562.

Capart, H., Eldho, T. I., Huang, S. Y., Young, D. L., and Zech, Y. (2003). "Treatment of natural geometry in finite volume river flow computations." Journal of Hydraulic Engineering, 129(5), 385-393.

Catella, M., Paris, E., and Solari, L. (2008). "Conservative scheme for numerical modeling of flow in natural geometry." Journal of Hydraulic Engineering, 134(6), 736-748.

Cockburn, B., and Shu, C.W. (1988). "The Runge-Kutta local projection P^1-discontinuous-Galerkin finite element method for scalar conservation laws." IMA Preprint Series #388, University of Minnesota.

Cockburn, B., and Shu, C. W. (1989). "TVB Runge-Kutta local projection discontinuous Galerkin finite element method for conservation laws II: General framework." Mathematics of Computation, 52(186), 411-435.

Cockburn, B., Lin, S. Y., and Shu, C. W. (1989). "TVB Runge-Kutta local projection discontinuous Galerkin finite element method for conservation laws III: One dimensional systems." Journal of Computational Physics, 84(1), 90-113.

Cockburn, B., Hou, S., and Shu, C. W. (1990). "The Runge-Kutta local projection discontinuous Galerkin finite element method for conservation laws IV: The multidimensional case." Mathematics of Computation, 54(190), 545-581.

Cockburn, B., and Shu, C. W. (1998). "The Runge-Kutta discontinuous Galerkin method for conservation laws V: Multidimensional systems." Journal of Computational Physics, 141(2), 199-224.

Cockburn, B. (1999). "Discontinuous Galerkin methods for convection dominated problems." High-order methods for computational physics, T. Barth and H. Deconinck, eds., LNCSE, Vol. 9, Springer-Verlag, New York, 69-224.

Cunge, J. A., Holly, F. M., and Verwey, A. (1980). Practical aspects of computational river hydraulics, Pitman, London.

Dawson, C., and Aizinger, V. (2005). "A discontinuous Galerkin method for three-dimensional shallow water equations." Journal of Scientific Computing, 22-23(1-3), 245-267.

Dolejší, V. (2010). "On the solution of linear algebraic systems arising from the semi-implicit DGFE discretization of the compressible Navier-Stokes equations." Kybernetika, 46(2), 260-280.

Einfeldt, B. (1988). "On Godunov-type methods for gas dynamics." SIAM Journal on Numerical Analysis, 25(2), 294-318.

Emmett, W. M., Myrick, R. M., and Meade, R. H. (1980). "Field data describing the movement and storage of sediment in the East Fork River, Wyoming, Part I. River hydraulics and sediment transport, 1979." USGS Open-File Report 80-1189, Denver.

Erduran, K. S., Kutija, V., and Hewett C. J. M. (2002). "Performance of finite volume solutions to the shallow water equations with shock-capturing schemes." International Journal for Numerical Methods in Fluids, 40(10), 1237-1273.

Ern, A., Piperno, S., and Djadel, K. (2008). "A well-balanced Runge-Kutta discontinuous Galerkin method for the shallow-water equations with flooding and drying." International Journal for Numerical Methods in Fluids, 58(1), 1-25.

Eskilsson, C., and Sherwin, S. J. (2004). "A triangular spectral/hp discontinuous Galerkin method for modelling 2D shallow water equations." International Journal for Numerical Methods in Fluids, 45(6), 605-623.

Fagherazzi, S., Rasetarinera, P., Hussaini, M. Y., and Furbish, D. J. (2004). "Numerical solution of the dam-break problem with a discontinuous Galerkin method." Journal of Hydraulic Engineering, 130(6), 532-539.

Fennema, R. J., and Chaudhry, M. H. (1990). "Explicit methods for 2-D transient free-surface flows." Journal of Hydraulic Engineering, 116(8), 1013-1034.

Fraccarollo, L., and Toro, E. F. (1995). "Experimental and numerical assessment of the shallow water model for two-dimensional dam-break type problems." Journal of Hydraulic Research, 33(6), 843-846.

Garcia-Navarro, P., and Vázquez-Cendón, M. (2000). "On numerical treatment of the source terms in the shallow water equations." Computers & Fluids, 29(8), 951-979.

Gharangik, A. M., and Chaudhry, M. H. (1991). "Numerical simulation of hydraulic jump." Journal of Hydraulic Engineering, 117(9), 1195-1211.

Godunov, S. K. (1959). "A difference method for the numerical calculation of discontinuous solutions of the equations of hydrodynamics." Matematicheskii Sbornik, 47(3), 271-306.

Goutal, N. (1999). "The Malpasset Dam failure – An overview and test case definition." Proceeding of CADAM Zaragoza meeting, Zaragoza, Spain.

Gottlieb, S., and Shu, C. W. (1998). "Total variation diminishing Runge-Kutta schemes." Mathematics of Computation, 67(221), 73-85.

Harten, A., Lax, P. D., and van Leer, B. (1983). "On upstream differencing and Godunov-type schemes for hyperbolic conservation laws." SIAM Review, 25(1), 35-61.

Harten, A., Engquist, B., Osher, S., and Charkravarthy, S. R. (1987). "Uniformly high order accurate essentially non-oscillatory schemes, III." Journal of Computational Physics, 71(2), 231-303.

Henderson, F. M. (1966). Open Channel Flow, McGraw-Hill, New York.

Hervouet, J. M. and Petitjean, A. (1999). "Malpasset dam-break revisited with two-dimensional computations." Journal of Hydraulic Research, 37(6), 777-788.

Hiver, J. M. (1997). "Etude expérimentale d'écoulement consécutif à une rupture de barrage dans un canal avec contre-pente et pente." Internal report, Châtelet, Belgium.

Ippen, A. T. and Dawson, J. H. (1951). "Design of channel contraction." Transactions of the American Society of Civil Engineers, 116, 326-346.

Jawahar, P., and Kamath, H. (2000). "A high-resolution procedure for Euler and Navier-Stokes computations on unstructured grids." Journal of Computational Physics, 164(1), 165-203.

Kawahara M. and Umetsu T. (1986). "Finite element method for moving boundary problems in river flow." International Journal for Numerical methods in Fluids, 6(6), 365-386.

Kesserwani, G., Ghostine, R., Vazquez, J., Ghenaim, A. and Mosé, R. (2008). "Riemann solvers with Runge-Kutta discontinuous Galerkin schemes for the 1D shallow water equations." Journal of Hydraulic Engineering, 134(2), 243-355.

Kesserwani, G., and Liang, Q. (2010). "A discontinuous Galerkin algorithm for the two-dimensional shallow water equations." Computer Methods in Applied Mechanics and Engineering, 199(49-52), 3356-3368.

Kesserwani, G., Liang Q., Vazquez, J., and Mosé, R. (2010). "Well-balancing issues related to the RKDG2 scheme for the shallow water equations." International Journal for Numerical Methods in Fluids, 62(4), 428-448.

Khalifa, A. M. (1980). "Theoretical and experimental study of the radial hydraulic jump." Ph. D. Thesis, University of Windsor, Windsor, Ontario, Canada.

Khan, A. A. (2000). "Modeling flow over an initially dry bed." Journal of Hydraulic Research, 38(5), 383-388.

Kubatko, E. J., Westerink, J. J., and Dawson, C. (2006). "Hp discontinuous Galerkin methods for advection dominated problems in shallow water flow." Computer Methods in Applied Mechanics and Engineering, 196(1-3), 437-451.

Lai, Y. G. (2010). "Two-dimensional depth-averaged flow modeling with an unstructured hybrid mesh." Journal of Hydraulic Engineering, 136(1), 12-23.

Li, B. Q. (2006). Discontinuous Finite Element in Fluid Dynamics and Heat Transfer, Springer, London.

Li, H., and Liu R. (2001). "The discontinuous Galerkin finite element method for the 2D shallow water equations." Mathematics and Computers in Simulation, 56(3), 223-233.

Liang, Q., and Borthwick, A. (2009). "Adaptive quadtree simulation of shallow flows with wet-dry fronts over complex topography." Computers & Fluids, 38(2), 221-234.

Lin, G., Lai, J., and Guo, W. (2003). "Finite-volume component-wise TVD schemes for 2D shallow water equations." Advances in Water Resources, 26(8), 861-873.

Lin, G., Lai, J., and Guo, W. (2005). "High-resolution TVD schemes in finite volume method for hydraulic shock wave modeling." Journal of Hydraulic Research, 43(4), 376-389.

Liu, X. D., Osher, S., and Chan, T. (1994). "Weighted essentially non-oscillatory schemes." Journal of Computational Physics, 115(1), 200-212.

Meade, R. H., Myrick, R. M., and Emmett, W. W. (1980). "Field data describing the movement and storage of sediment in the East Fork River, Wyoming, Part II. Bed elevations, 1979." US Geological Survey, Open-File Report 80-1190, Denver.

Nujić, M. (1995). "Efficient implementation of non-oscillatory schemes for the computation of free-surface flows." Journal of Hydraulic Research, 33(1), 101-111.

Perthame, B., and Simeoni, C. (2001). "A kinetic scheme for the Saint-Venant system with a source term." Calcolo, 38(4), 201-231.

Qiu, J., and Shu, C. W. (2005). "Runge-Kutta discontinuous Galerkin method using WENO limiters." SIAM Journal on Scientific Computing, 26(3), 907-929.

Ray, H. A., and Kjelstrom, L. C. (1978). "The flood in southeastern Idaho from the Teton Dam failure of June 5, 1976." U.S. Geological Survey, Open-File Report 77-765, Boise, Idaho, USA.

Reed, W. H., and Hill, T. R. (1973). "Triangular mesh method for the neutron transport equation." Los Alamos Scientific Laboratory Report, LA-UR-73-479, 1-23.

Roe, P. L. (1981). "Approximate Riemann solvers, parameter vectors, and difference schemes." Journal of Computational Physics, 43(2), 357-372.

Rosu, C., and Ahmed, M. (1999). "Toce River dam-break test case – A comparison between the ISIS numerical model and the physical model." Proceedings of the 3rd CADAM Workshop, Milan, Italy.

Sanders, B. F. (2001). "High-resolution and non-oscillatory solution of the St. Venant equations in non-rectangular and non-prismatic channels." Journal of Hydraulic Research, 39(3), 321-330.

Sanders, B. F., Jaffe, D. A., and Chu, A. K. (2003). "Discretization of integral equations describing flow in nonprismatic channels with uneven beds." Journal of Hydraulic Engineering, 129(3), 235-244.

Sanders, B. F. and Begnudelli L. (2010). "BreZo: A hydrodynamic flood simulation algorithm." http://sanders.eng.uci.edu/brezo.html (March 1, 2011).

Schoklitsch, A. (1917). "Ueber Dammbruchwellen." Sitzungsberichte der Kaiserlichen Akademie der Wissenschaften, Viennal, 126, 1489-1514.

Schwanenberg, D., and Köngeter, J. (2000). "A discontinuous Galerkin method for the shallow water equations with source terms." In Cockburn, B., Karniadakis, G. E., and Shu, C. W., editors, Discontinuous Galerkin Methods, Vol. 11 of Lecture Notes in Computational Science and Engineering, Springer, Berlin, 419-424.

Schwanenberg, D., and Harms, M. (2004). "Discontinuous Galerkin finite-element method for transcritical two-dimensional shallow water flows." Journal of Hydraulic Engineering, 130(5), 412-421.

Soares Frazão, S., and Testa, G. (1999). "The Toce River test case: Numerical results analysis." Proceedings of the 3rd CADAM workshop, Milan.

Soares Frazão, S., Sillen, X., and Zech, Y. (1999). "Dam-break flow through sharp bends, physical model and 2D Boltzmann model validation." Proc., CADAM Meeting Wallingford, U. K., 2-3 March 1998, European Commission, Brussels, Belgium, 151-169.

Soares Frazão, S., and Zech, Y. (2002). "Dam-break in channels with 90^0 bend." Journal of Hydraulic Engineering, 128(11), 956-968.

Song, L., Zhou, J., Li, Q., Yang, X., and Zhang Y. (2011). "An unstructured finite volume model for dam-break floods with wet/dry fronts over complex topography." International Journal for Numerical Methods in Fluids, 67(8), 960-980.

Thacker, W. C. (1981). "Some exact solutions to the nonlinear shallow-water equations." Journal of Fluid Mechanics, 107, 499-508.

Toro, E. (1989). "A weighted average flux method for hyperbolic conservation laws." Proceedings of the Royal Society of London. Series A, Mathematical and Physical Sciences, 423(1865), 401-418.

Toro, E., Spruce M., and Speares, W. (1994). "Restoration of the contact surface in the HLL-Riemann solver." Shock Waves, 4(1), 25-34.

Tu, S., and Aliabadi, S. (2005). "A slope limiting procedure in discontinuous Galerkin finite element method for gasdynamics applications." International Journal of Numerical Analysis and Modeling, 2(2), 163-178.

U. S. Army Corps of Engineers (1960). "Floods resulting from suddenly breached dams." Misc Paper No. 2-374, Report 1: Conditions of Minimum Resistance. Waterways Experiment Station, Vicksburg, Mississippi.

Xing, Y., Zhang, X., and Shu, C. W. (2010). "Positivity-preserving high order well-balanced discontinuous Galerkin methods for the shallow water equations." Advances in Water Resources, 33(12), 1476-1493.

Ying, X., Khan, A. A., and Wang, S. S. Y. (2004). "Upwind conservative scheme for the Saint Venant equations." Journal of Hydraulic Engineering, 130(10), 977-987.

Ying, X., Jorgeson, J., and Wang, S. S. Y. (2009). "Modeling dam-break flows using finite volume method on unstructured grid." Engineering Applications of Computational Fluid Mechanics, 3(2), 184-194.

Yoon, T. H. and Kang, S. (2004). "Finite volume model for two-dimensional shallow water flows on unstructured grids." Journal of Hydraulic Engineering, 130(7), 678-688.

Zhou, J. G., Causon, D. M., Mingham, C. G., and Ingram, D. M. (2001). "The surface gradient method for the treatment of source terms in the shallow-water equations." Journal of Computational Physics, 168(1), 1-25.